

Development of a Cryogenic DC Photoelectron Gun for GaAs Cathodes with Increased Charge Lifetime

Entwicklung einer kryogenen DC-Photoelektronen-Kanone für GaAs-Kathoden mit verlängerter Ladungslebensdauer

Zur Erlangung des Grades eines Doktors der Naturwissenschaften (Dr. rer. nat.)

Genehmigte Dissertation von Tobias Eggert aus Langen

Tag der Einreichung: 20.12.2022, Tag der Prüfung: 23.01.2023

1. Gutachten: Prof. Dr. Joachim Enders
2. Gutachten: Prof. Dr. Dr. h.c. mult. Norbert Pietralla
Darmstadt – D17



TECHNISCHE
UNIVERSITÄT
DARMSTADT

Fachbereich Physik
Institut für Kernphysik
AG Enders

Development of a Cryogenic DC Photoelectron Gun for GaAs Cathodes with Increased Charge Lifetime

Entwicklung einer kryogenen DC-Photoelektronen-Kanone für GaAs-Kathoden mit verlängerter Ladungslebensdauer

Accepted doctoral thesis by Tobias Eggert

1. Review: Prof. Dr. Joachim Enders
2. Review: Prof. Dr. Dr. h.c. mult. Norbert Pietralla

Date of submission: 20.12.2022

Date of thesis defense: 23.01.2023

Darmstadt – D17

Bitte zitieren Sie dieses Dokument als:

URN: urn:nbn:de:tuda-tuprints-232755

URL: <http://tuprints.ulb.tu-darmstadt.de/23275>

Dieses Dokument wird bereitgestellt von tuprints,
E-Publishing-Service der TU Darmstadt
<http://tuprints.ulb.tu-darmstadt.de>
tuprints@ulb.tu-darmstadt.de

Die Veröffentlichung steht unter folgender Creative Commons Lizenz:
Namensnennung – Weitergabe unter gleichen Bedingungen 4.0 International
<https://creativecommons.org/licenses/by-sa/4.0/>

This work is licensed under a Creative Commons License:
Attribution–ShareAlike 4.0 International
<https://creativecommons.org/licenses/by-sa/4.0/>

For the most part we do not first see, and then define, we define first and then see.

- Walter Lippmann

Erklärungen laut Promotionsordnung

§8 Abs. 1 lit. c PromO

Ich versichere hiermit, dass die elektronische Version meiner Dissertation mit der schriftlichen Version übereinstimmt.

§8 Abs. 1 lit. d PromO

Ich versichere hiermit, dass zu einem vorherigen Zeitpunkt noch keine Promotion versucht wurde. In diesem Fall sind nähere Angaben über Zeitpunkt, Hochschule, Dissertationsthema und Ergebnis dieses Versuchs mitzuteilen.

§9 Abs. 1 PromO

Ich versichere hiermit, dass die vorliegende Dissertation selbstständig und nur unter Verwendung der angegebenen Quellen verfasst wurde.

§9 Abs. 2 PromO

Die Arbeit hat bisher noch nicht zu Prüfungszwecken gedient.

Darmstadt, 20.12.2022

T. Eggert

Abstract

Electron beams can be generated by utilizing the internal photoelectric effect. In this matter, a special photocathode material is necessary for generating polarized electrons. Gallium arsenide (GaAs) proved to be the best choice. However, the production of polarized electrons requires a photo-emission close to the band gap, which in turn requires a negative-electron-affinity (NEA) coating consisting of caesium (Cs) and either oxygen or nitrogen trifluoride (NF₃). This layer limits the possible operation time of the electron source as the layer deteriorates over time due to interactions with residual gas particles, with contamination through desorption and degradation through ionized particles hitting the surface being the two main mechanisms. The latter is called ion back-bombardment (IBB) and is the main lifetime-limiting factor during high-current electron emission. Therefore, a reduction of IBB in order to increase operational lifetime and performance of electron sources is of great interest for many accelerator-based applications with polarized electrons.

In this dissertation the design, assembly and first experimental results of a new kind of electron source is presented, which aims at reducing IBB by placing the cathode inside an almost closed cryogenic sub-volume. The inner walls of this volume are coated with activated charcoal making them act as a cryopump, reducing the local pressure significantly. The closed design limits the flux of particles from the outer, higher vacuum into the volume. Simulations of the hydrogen partial pressure, which contributes the most to IBB, shows a reduction of up to two magnitudes compared to conventional sources. As IBB intensity directly scales with the amount of residual gas molecules, a significant increase in lifetime can be anticipated. In addition, the cooling of the cathode itself compensates the heat load deposited by the laser beam, hence reducing heat-induced desorption of the NEA layer that would otherwise severely limit cathode lifetime for high-current applications.

A pressure below $1 \cdot 10^{-11}$ mbar outside the sub-volume could be achieved after a four-week bake-out at 120 °C inside an aluminum vacuum chamber equipped with a 45 l/s ion-getter pump and four 430 l/s non-evaporable getter panels.

Electrostatic field simulations for electrode voltages ranging from -5 kV to -30 kV have been conducted, showing a maximum field gradient of 11.1(1) MV/m at -30 kV. Experi-

mentally, a stable voltage of -12 kV without and -14 kV with cooling of the electrode has been achieved. Simulations of the electron beam at potentials from -12 kV to -30 kV showed no beam loss for currents from 10 μ A to 1 mA.

The required cooling power was provided by a 1.1 W closed-cycle cryostat. A temperature of 21.3(1) K at the far end of the sub-volume has been reached allowing an effective pumping of hydrogen.

A dedicated test stand was designed and setup at the Institut für Kernphysik of the Technische Universität Darmstadt to conduct measurements evaluating a potential lifetime enhancing effect. It does not feature a chamber to conduct the process of applying the NEA layer to the photocathode surface, also called photocathode activation, hence requiring the use of the existing test stand for Photo-Cathode Activation, Testing, and Cleaning using atomic Hydrogen (Photo-CATCH) for the cleaning and activation procedure. A measurement series demonstrated that a transport chamber, equipped with a NEG pump, is capable of retaining enough of the NEA layer, to allow a transfer of activated cathode from Photo-Catch to the new electron source. After transferring and storing for 20 h a quantum efficiency (QE) of up to 67 % using a red laser with 780 nm and 99 % with a blue 450 nm laser could be maintained. For a foreseen integration of the source into Photo-CATCH, simulations show that with minor modifications of the beamline an operation of both the cryogenic and the conventional source, already in place, is possible.

A measurement demonstrating a life time enhancing effect could not be conducted, as the beam was lost at an unknown location in the system. Multiple approaches were conducted to identify the origin of the beam loss, offering room for further exploration.

Zusammenfassung

Elektronenstrahlen können durch Nutzung des internen photoelektrischen Effekts erzeugt werden. Hinsichtlich polarisierter Elektronen ist dafür ein spezielles Photokathodenmaterial erforderlich. Galliumarsenid (GaAs) hat sich hierfür als die beste Wahl erwiesen. Jedoch erfordert die Erzeugung von polarisierten Elektronen eine Photoemission nahe der Bandlücke, was wiederum eine Beschichtung mit negativer Elektronenaffinität (NEA) erfordert, die aus Cäsium (Cs) und entweder Sauerstoff (O) oder Stickstofftrifluorid (NF₃) besteht. Diese Schicht begrenzt die mögliche Betriebsdauer der Elektronenquelle, da sich die Schicht im Laufe der Zeit aufgrund von Wechselwirkungen mit Restgas-Molekülen verschlechtert, wobei die beiden wichtigsten Mechanismen die Kontamination durch Desorption und der Abbau durch ionisierte Teilchen sind, die auf die Oberfläche aufschlagen. Letzteres wird als Ionen-Rückbombardement (eng. ion back-bombardment, IBB) bezeichnet und ist der wichtigste lebensdauerbegrenzende Faktor bei der Elektronenemission mit hohen Strömen. Daher ist eine Verringerung des IBB zur Erhöhung der Lebensdauer und Leistung von Elektronenquellen für viele beschleunigerbasierte Anwendungen mit polarisierten Elektronen von großem Interesse.

In dieser Dissertation werden der Entwurf, der Aufbau und die ersten experimentellen Ergebnisse einer neuartigen Elektronenquelle vorgestellt, die darauf abzielt, IBB zu verringern, indem die Kathode in einem nahezu geschlossenen kryogenen Teilvolumen untergebracht wird. Die Innenwände dieses Volumens sind mit Aktivkohle beschichtet, so dass sie wie eine Kryopumpe wirken und den lokalen Druck erheblich reduzieren. Durch die geschlossene Bauweise wird der Fluss von Partikeln aus dem äußeren, höheren Vakuum in das Teilvolumen begrenzt. Simulationen des Wasserstoffpartialdrucks, der am stärksten zum IBB beiträgt, zeigen eine Verringerung um bis zu zwei Größenordnungen im Vergleich zu herkömmlichen Quellen. Da die IBB-Intensität direkt mit der Menge der Restgasmoleküle skaliert, ist eine deutliche Verlängerung der Lebensdauer zu erwarten. Darüber hinaus kompensiert die Kühlung der Kathode selbst die durch den Laserstrahl verursachte Wärmebelastung und verringert so die wärmebedingte Desorption der NEA-Schicht, die ansonsten die Lebensdauer der Kathode bei Hochstromanwendungen stark einschränken würde.

Nach einem vierwöchigen Ausheizen bei 120 °C einer Aluminium Kammer, die mit einer 45 l/s Ionengetter-Pumpe und vier 430 l/s nicht evaporierbaren Getterpumpen Panelen (NEG) ausgestattet ist, konnte außerhalb des Teilvolumens ein Druck von unter $1 \cdot 10^{-11}$ mbar erreicht werden.

Es wurden elektrostatische Feldsimulationen für Elektrodenspannungen von -5 kV bis -30 kV durchgeführt, die einen maximalen Feldgradienten von 11,1(1) MV/m bei -30 kV zeigten. Experimentell wurde eine stabile Spannung von -12 kV ohne und -14 kV mit Kühlung der Elektrode erreicht. Simulationen des Elektronenstrahls mit Potentialen von -12 kV bis -30 kV zeigten keinen Strahlverlust für Ströme von 10 μ A bis 1 mA.

Die erforderliche Kühlleistung wurde von einem 1,1 W Kryostaten mit geschlossenem Kreislauf bereitgestellt. Am Ende des Teilvolumens wurde eine Temperatur von 21,3(1) K gemessen, die ein effektives Pumpen von Wasserstoff ermöglicht.

Am Institut für Kernphysik der Technischen Universität Darmstadt wurde ein Teststand entworfen und aufgebaut, um Messungen zur Bewertung eines potenziellen lebensdauer-verlängernden Effekts durchzuführen. Er verfügt über keine Kammer für das Aufbringen der NEA-Schicht auf die Photokathodenoberfläche, auch Photokathodenaktivierung genannt, so dass für das Reinigungs- und Aktivierungsverfahren der bestehende Teststand für Photokathodenaktivierung, -prüfung und -reinigung mit atomarem Wasserstoff (eng. Photo-Cathode Activation, Testing, and Cleaning using atomic Hydrogen, Photo-CATCH) verwendet werden muss. Eine Messreihe zeigte, dass eine mit einer NEG-Pumpe ausgestattete Transportkammer in der Lage ist die NEA-Schicht ausreichend zu erhalten, um einen Transfer der aktivierten Kathode von Photo-Catch zur neuen Elektronenquelle zu ermöglichen. Nach dem Transfer und der Lagerung für 20 h konnte eine Quanteneffizienz (QE) von bis zu 67 % mit einem roten 780 nm Laser und 99 % mit einem blauen 450 nm-Laser aufrechterhalten werden. Für die vorgesehene Integration der Quelle in Photo-CATCH zeigen Simulationen, dass mit geringfügigen Änderungen an der Strahlführung ein Betrieb sowohl der kryogenen als auch der bereits vorhanden konventionellen Quelle möglich ist.

Eine Messung, die eine lebensdauerverlängernde Wirkung nachweisen sollte, konnte nicht durchgeführt werden, da der Strahl an einer unbekannt Stelle im System verloren ging. Es wurden mehrere Versuche durchgeführt, um den Ursprung des Strahlverlustes zu ermitteln, die Raum für weitere Untersuchungen bietet.

Contents

1	Introduction	1
2	Fundamentals of Photocathodes	5
2.1	Polarized Electrons	5
2.2	Photoelectric Effect	6
2.2.1	Three-Step Model	6
2.2.2	Quantum Efficiency	8
2.3	Gallium Arsenide Photocathodes	10
2.3.1	Higher Degree of Polarization	14
2.3.2	Escape into Vacuum	17
2.3.3	Cathode Activation	19
2.3.4	Surface-Layer Decay and Lifetime	20
3	Ultra-High Vacuum	29
3.1	Fundamental Concepts	29
3.2	Achieving Ultra- and Extreme-High Vacuum	31
3.3	Vacuum Pumps	33
3.4	Cryopumps	37
3.4.1	Pumping Mechanisms	38
3.4.2	Sorption Materials	40
3.4.3	Pump Regeneration	42
3.4.4	Heat Influx	42
3.4.5	Commercial Refrigerator-Cooled Cryopumps	45
4	Design of a Cryogenic Electron-Gun	49
4.1	Idea and Motivation	49
4.2	Photo-CATCH and Cathode Preparation System	50
4.2.1	Photo-CATCH Overview	50
4.2.2	Cathode Preparation System	53

4.3	Cryogenic Sub-Volume	57
4.3.1	Exit-Pipe Dimension	62
4.3.2	Electric Field and Field Emission	66
4.3.3	Simulation of the Electron Beam	68
4.4	Cryocooler and Heat Assessment	76
4.4.1	Heat Assessment	80
4.5	Vacuum Chamber	83
4.6	Transport Chamber	86
4.7	Laser Setup	88
4.8	Dedicated Test Stand	92
4.9	The Integration Into Photo-CATCH	96
5	Assembly and Commissioning	103
5.1	Cryo Gun Chamber Assembly	103
5.2	Transport Chamber Evaluation	110
5.3	Commissioning	114
5.3.1	Bake-Out and NEG Activation	114
5.3.2	Laser Commissioning and Properties	114
5.3.3	Cryocooler Commissioning	118
5.3.4	Lifetime Measurement	125
6	Summary and Outlook	129
A	Appendix	133
A.1	Technical Drawings	133
	Curriculum Vitae	156
	List of Publications	157

List of Figures

2.1	Electron Emission from Semiconductors	9
2.2	Crystal structure of GaAs	11
2.3	Band Structure of bulk GaAs	12
2.4	Energy Levels and Possible Transitions in Bulk GaAs	13
2.5	Band structure of strained-superlattice GaAs	15
2.6	Energy Levels and Possible Transitions in Strained-Superlattice GaAs	16
2.7	Energy Levels of NEA Activated GaAs	18
2.8	Co-Deposition Activation Scheme	21
2.9	Decay of Quantum Efficiency when Exposed to Different Gases	23
2.10	Thermal Desorption Rate for Caesium and Gallium	24
3.1	Residual Gases Spectrum Before and After Bake-Out	33
3.2	Working Principle of a Diaphragm Pump	34
3.3	Setup and Working Principle of a Spotter Ion Pump	35
3.4	Saturation Pressure Over the Temperature for Some Common Gases	39
3.5	Desorption of Activated Charcoal	43
3.6	Cryopump Regeneration Process of CO ₂	44
3.7	Refrigerator Cooled Cryopump with Integrated Cryocooler	47
4.1	Puck and Transport Fork	51
4.2	Overview of the Photo-CATCH Test Stand	52
4.3	Activation Setup	55
4.4	Cathode Activation Chamber	56
4.5	Cryogenic Sub-Volume	58
4.6	Thermal Conductivity for the Materials Used	59
4.7	Electrode and Puck Insertion	61
4.8	Molflow Simulations of the Cryo and Photo Catch Gun Chamber	66
4.9	CST Simulation of the Electric Field	69
4.10	Maximum Field Gradient for Different Electrode Potentials	69
4.11	Emission Surface and Angles Distribution in CST	71

4.12 CST Simulated Electron Beam	72
4.13 CST Simulation Results of the Beam Envelope	75
4.14 CST Simulated Off-Axis Electron Beam	77
4.15 CST Simulated Electron Beam With Earth Magnetic Field	78
4.16 Cryocooler with Low Vibration Interface	81
4.17 Outer Vacuum Chamber	85
4.18 Activation Temperature of NEG Modules	86
4.19 Cryo source Assembly	87
4.20 Transport chamber	89
4.21 Quantum Efficiency and Polarization in Relation to Wavelength	90
4.22 Laser Setup	91
4.23 Laser Decoupling Mirror Array	93
4.24 Dedicated cryo source Test Stand	94
4.25 Transfer Chamber	97
4.26 Integration of the Cryo-Source Chamber into Photo-CATCH	98
4.27 Position Spread Along the Photo-CATCH Beamline	100
4.28 Angular Deviation Along the Photo-CATCH Beamline	101
5.1 Charcoal Coated Sub-Volume	105
5.2 Sub-Volume with h.v. Cable	105
5.3 Temperature Sensor at Sub-Volume	105
5.4 Cryocooler with Mounted Sub-Volume	106
5.5 Cryocooler with Sub-Volume and Heat Shield	106
5.6 View into the Cryo Gun Chamber	107
5.7 NEG Panel Connection to Feedthrough	108
5.8 NEG Panels inside Cryo Gun Chamber	108
5.9 h.v. Cable and Feedthrough	108
5.10 Completely Assembled Cryo Gun Chamber	109
5.11 Transport Chamber Pressure Development	113
5.12 View of the Laserspot in the Sub-Volume	115
5.13 Laser Beam Profile	117
5.14 Laser Power Fluctuations	119
5.15 Cryocooler and Sub-volume Cooling Curve 1	120
5.16 Cryocooler and Sub-volume Cooling Curve 2	122
5.17 Temperature Rise due to the Laser	123
5.18 Residual Gas Spectrum After Cooldown	124
A.1 Technical Drawing Vacuum Chamber 1	133

A.2	Technical Drawing Vacuum Chamber 2	134
A.3	Technical Drawing Vacuum Chamber 3	135
A.4	Technical Drawing Vacuum Chamber 4	136
A.5	Technical Drawing Sub-Volume 1	137
A.6	Technical Drawing Sub-Volume 2	138
A.7	Technical Drawing Heat Shield	139

List of Tables

2.1	Values for the Energy Gap Calculation for GaAs	10
2.2	Values for the Calculation of the Width of the Band Bending Region of GaAs	19
2.3	Temperature Rises for Some Existing and Planned Electron Sources	25
3.1	Vacuum Classifications	31
4.1	Maximum Acceptable Initial Pressure in Sub-Volume	63
4.2	Pressure Ratios In and Outside the Sub-volume for Different exit-pipes . .	64
4.3	Hydrogen Outgassing Rates used for Molflow+ Simulations	65
4.4	Molflow+ Simulation Results for Cryogenic Temperatures	65
4.5	CST Particle Source Parameters	73
4.6	Beam Divergence	74
4.7	Cryocooler Properties	80
4.8	Emissivity for Heat Assessment Calculations	82
4.9	Enthalpy Transfer for Some Gases	83
4.10	Heat Load on Cryocooler	84
5.1	Activated Charcoal Properties	104
5.2	QE Decay Measurement of the Transport Chamber	112
5.3	Laser Beam Waist at Different Distances	116
5.4	Stability of the Laser Power	118

Glossary

activation	process of applying a thin film on a photocathode in order to increase its electrical sensitivity to light
bunch charge	total electric charge of a bunch of particles
collider	particle accelerator that collides two particle beams
doping	intentional introduction of impurities into a semiconductor during production in order to modify its properties
electron affinity	amount of energy required to move an electron at the surface of a semiconductor from the bottom of the conduction band to the vacuum
Faraday cup	metal cup used to capture charged particles and measure the resulting current
gun	source of charged particles used in particle accelerators
lifetime	time parameter used to characterize a decay process
manipulator	magnetically-coupled linear transfer devices used for the transfer of pucks inside of vacuum chambers
photocathode	piece of material used to convert light into electrons using the photoelectric effect

puck	round mount for holding a photocathode in place
quantum efficiency	ratio of incident photons to emitted electrons, used for the classification of a photocathode's efficacy
spin polarization	degree to which the spin of a particle ensemble is aligned with a chosen axis

Acronyms

AC	Activation Chamber
AHCC	Atomic Hydrogen Cleaning Chamber
ARS	Advanced Research Systems
CAC	Cathode Activation Chamber
CAN	Controller Area Network
CB	Conduction Band
CB _{min}	Conduction Band minimum
CGC	Cryo Gun Chamber
Cs	Caesium
CSS	Control System Studio
DBR	Distributed Bragg Reflector
DC	Direct-Current
EA	Electron Affinity
EPICS	Experimental Physics and Industrial Control System
ERL	Energy-Recovery Linear accelerator
ESD	Electron Stimulated Desorption
FEL	Free-Electron Laser
FOM	Figure of Merit
FV	Fine Vacuum
GaAs	Gallium Arsenide
GC	Gun Chamber
GUI	Graphical User Interface
H	Hydrogen

He	Helium
hh	heavy-hole
HV	High Vacuum
HVo	High Voltage
IBB	Ion Back-Bombardment
IGP	Ion Getter Pump
IKP	Institut für Kernphysik
lh	light hole
LLC	Load-Lock Chamber
NEA	Negative Electron Affinity
NEG	Non-Evaporable Getter
NF ₃	Nitrogen Trifluoride
O	Oxygen
PEA	Positive Electron Affinity
PEC	Perfect Electric Conductor
Photo-CATCH	Photocathode Activation, Test and Cleaning using atomic Hydrogen
PIC	Particle In Cell
QCF	Quick Flange
QE	Quantum Efficiency
RF	Radio-Frequency
RGA	Residual Gas Analyser
RMS	Root Mean Square
RV	Rough Vacuum
S-DALINAC	Superconducting Darmstadt Linear electron Accelerator
SPIn	Spin-Polarized Injector
SRF	Superconducting Radio-Frequency
TC	Transfer Chamber

TSM	Three-Step Model
TUD	Technische Universität Darmstadt
UHV	Ultra-High Vacuum
VB	Valenc Band
VB _{max}	Valence Band maximum
XHV	Extreme-High Vacuum

Symbols

A	area
A_c	area, cryo surface
A_{EB}	area, electron beam
A_s	area, solid
α	material dependent quantity for energy gap calculation
$\alpha(\nu)$	absorption coefficient
α_{PE}	reduced photo-emissive absorption coefficient
α_s	cryo pump sticking probability
β	material dependent quantity for energy gap calculation
c	speed of light
C	gas flow conductance
C_{12}	thermal radiation exchange number
c_s	cryo pump capture coefficient
C_{tot}	gas flow conductance, total
χ_{eff}	effective electron affinity
d_{BBR}	width of the band bending region
d_{pipe}	diameter, exit pipe
$d_{rms,(x/y)}$	root mean square electron beam envelope, diameter
ΔH	cryosorption enthalpy transfer per molecule
Θ_{div}	electron beam divergence
dn/dt	NEA layer desorption rate
e	elemental charge
E	electric field
E_A	electron affinity
E_B	surface binding energy of NEA atoms

E_{BB}	band bending energy
E_G	semiconductor energy gap
E_{kin}	kinetic energy of emitted photons
E_P	photon energy
E_{VF}	energy difference between valence band maximum and Fermi energy
ϵ	emissivity
ϵ_0	vacuum permittivity
ϵ_s	dielectrical constant
η	quantum efficiency
h	Plancks constant
\vec{I}	nuclear spin
$I_0, I(x)$	light intensity at incident/at distance x
$i(\nu)$	total electron yield
I_p	photocurrent
k	crystal momentum
k_B	Boltzmann constant
$k(T)$	thermal conduction
l	traveled distance
L	length
$l_a(\nu)$	absorption length
L_e	escape length
l_{pipe}	length, exit pipe
λ	light/photon wavelength
M	molar mass
n	number of NEA layer atoms bound to surface per unit area
$N \uparrow, N \downarrow$	number of electrons with spin parallel/antiparallel to a chosen axis
N_{e^-}	count of electrons
N_i	number of ionize molecules

N_P	count of photons
ν	light/photon frequency
ν_t	thermal desorption rate constant
ω	laser spot diameter ($1/e^2$, gaussian beam)
p	pressure
P	polarization degree
P_E	escape propability of an electron
P_{ex}	probability to exited an electron above vacuum level
p_{in}	pressure, inside of sub-volume
P_L	laser power
p_{out}	pressure, outside of sub-volume
P_T	probability of en electron to reach the surface with sufficient energy for emission
ϕ	electrostatical potential
φ_{12}	viewing factor
ϕ_i	zimuth angle, i-th emitted electron
Q	gas throughput
q_b	charge, total electron bunch/beam
Q_{dif}	gas throughput, diffusion
\dot{q}_G	heat load, gas conduction
q_i	charge, i-th macro particle
Q_{in}	gas flux, into sub-volume
Q_{lea}	gas throughput, leak
Q_{out}	gas flux, out of sub-volume
\dot{q}_P	heat load, cryosorption/cryocondensation
Q_{pro}	gas throughput, process
\dot{q}_R	heat load, radiation
\dot{q}_S	heat load, solid conduction
Q_τ	lifetime, charge (in unit of charge)
\dot{q}_{tot}	heat load, total
Q_{tot}	gas throughput, total
Q_{vol}	gas load in volume
R	universal gas constant
$R(\nu)$	light reflectivity

$r_{rms,(x/y)}$	root mean square electron beam envelope, radius
ρ_i	gas density
\vec{s}	spin vector of electrons
S	pumping speed
S_{id}	pumping speed, black hole
n_p	doping density
σ	Stefan-Boltzmann constant
σ_i	ionization cross section
r	beam splitter splitting ratio
t	time
T	temperature
τ	lifetime, total
τ_D	lifetime, dark
τ_{IBB}	lifetime, ion back-bombardment
τ_{td}	lifetime, thermal
τ_C	lifetime, charge (in unit of time)
θ_i	polar angle, i-th emitted electron
θ_{max}	polar angle, maximal
θ_{rms}	polar angle, root mean square
C_t	window transmission coefficient
\bar{v}	thermal velocity
V	Volume
w	cryo pump transmission probability
W	gas flow resistance
w_i	weight factor
W	work function
$\langle x \rangle$	arithmetical mean/rms electron position
$\langle x^2 \rangle$	variance electron position

1 Introduction

Electron accelerators have been around since the end of the 19th century, exhibiting versatile applications in industry, in fundamental research and medicine. The most prevalent industrial application is the modification of plastic and rubber products while in medicine they are used, among others, for the sterilization of medical devices and radiotherapy. Recently emerging applications include the treatment of toxic industrial wastes as well as the preservation of foods [1]. Intense X-ray radiation originating from electron synchrotrons [2] or free-electron lasers (FEL) [3] is employed in material science, condensed-matter physics, and even biomedical imaging applications. For basic research in subatomic physics, electrons have been used for more than 50 years in scattering experiments studying nuclear shapes and excitations [4].

Before the electrons can be accelerated, they need to be generated by electron sources also referred to as electron guns. The three most commonly used principles for electron generation are field emission, thermionic emission and photoemission. In guns of the latter type the electron beam is extracted from a so-called photocathode by irradiation with laser light making use of the photoelectric effect as first discovered by Hertz [5] and later described by Einstein [6].

The photo-electron guns used today can be grouped into categories depending on their gun design and the cathode material used. There are two popular designs, where the first uses a static electric field to accelerate the emitted photons away from the cathode surface. The field is generated by applying a negative potential to an electrode housing the cathode and either a positive or ground potential to an anode. These types are referred to as direct-current (DC) photo-guns. Guns of the second type are called radio-frequency (RF) guns and work with an alternating electromagnetic field gradient by placing the cathode directly in an RF cavity. The first gun of this types was commissioned by Fraser et al. in 1986 at the Los Alamos National Laboratory [7]. With a superconducting cavity, this design is named superconducting RF (SRF) gun.

In theory, (S)RF guns provide higher field gradients but are technological challenging in practice. In comparison, photoinjectors consisting of a DC gun followed by an (S)RF

injector to further accelerate the electrons have been established with good performance for many years [8, 9]. They are considered to be more mature and reliable. However, SRF guns made substantial progress in recent years and may play a more important role for future accelerators [10, 11].

When it comes to choosing the cathode material, there are also two types used in today's guns: metals and semiconductors. The emission efficiency of both is characterized by the ratio of incident photons to emitted electrons, commonly referred to as quantum efficiency. Metal cathodes exhibit a high work function resulting in low quantum efficiency but they provide a high robustness which makes them a suitable candidate for RF and SRF guns. Semiconductor cathodes can again be split into two sub-groups depending on the sign of the electron affinity (EA) they exhibit. The EA describes the amount of energy which is released when an electron attaches to a neutral atom. Positive electron affinity (PEA) cathodes show a comparable robustness as metal cathodes but provide a higher quantum efficiency. In contrast, negative electron affinity (NEA) cathodes demand a thin surface coating to create the NEA condition, making them less robust and limits their operational lifetime significantly compared to metal and PEA cathodes.

Despite this disadvantage, NEA cathodes are still relevant for electron guns as they show some unique properties, like gallium arsenide (GaAs), which can emit spin-polarized electrons with polarization degrees of up to 90% [12]. Therefore, photo-guns using GaAs are a popular source for spin-polarized electrons as they can provide a higher current than other sources such as β -decay, ionization of polarized Helium (He), optical pumping of unpolarized alkali atoms (Fano-Effect) or Mott scattering [13, 14]. GaAs exhibits a high quantum efficiency and requires a NEA coating with caesium (Cs) [15] and either oxygen (O₂), nitrogen trifluoride (NF₃) [16] or fluorine (F) [17]. As (S)RF guns cannot provide the vacuum conditions needed to sustain the NEA coating, DC guns are the only viable option for the operation of GaAs cathodes [9]. They are used among others in energy-recovery linear accelerators (ERLs) [18–22] and FELs [23, 24].

Polarized electron beams allow to access polarization-sensitive observables, e.g. in studies on nuclear and nucleon structure such as the proton magnetic form factor [25], the determination of the neutron skin thickness of medium to heavy nuclei [26] or the high precision determination of the electroweak mixing angle with the P2 experiment [27]. Proposed future projects for polarized guns include the production of spin-polarized positrons by transferring the polarization of an electron beam to positrons via Bremsstrahlung [28], the cooling of electrons at high-energy storage rings [29] and the use in colliders [30–32].

One accelerator featuring a GaAs-based electron-gun for spin-polarized electrons is the Superconducting Darmstadt Linear electron Accelerator (S-DALINAC) at the Institut für Kernphysik of the Technische Universität Darmstadt [33]. First operation as an ERL has

been achieved in 2017 [34] while the first multi-turn ERL operation could be realized in 2021 [35]. The Spin-Polarized Injector (SPIn) of the S-DALINAC can provide 100 keV electrons with a polarization of up to 86 % [36]. In addition, a DC thermionic gun can provide unpolarized electrons with an energy up to 250 keV. There are a number of foreseen experiments at the S-DALINAC using spin-polarized electrons, including the determination of polarization correlations in Bremsstrahlung production and the study of parity violation in photo fission using intense polarized photon beams [37–39].

As already mentioned, the operation time of GaAs cathodes is limited by the NEA surface coating which degrades over time [40]. The procedure of applying this NEA layer is called cathode activation. The parameters of this procedure have a significant impact on the achievable quantum efficiency as well as the robustness of the coating and is still subject to recent research. To reproducibly provide reliable high-performance photocathodes for accelerator operation, the optimization and standardization of the activation process is of great demand. A second lifetime relevant factor is the vacuum condition around the cathode, where a total pressure in the 10^{-11} mbar regime or lower is required [41].

As SPIn is not accessible during beamtime operation of the S-DALINAC, a dedicated test stand for Photo-Cathode Activation, Testing, and Cleaning using atomic Hydrogen (Photo-CATCH) has been constructed in a separate laboratory [42, 43], allowing further studies of the activation process [44] and the design of the electron gun [45].

Recently multiple promising approaches to increase the robustness of the NEA layer have emerged, including the introduction of additional elements such as lithium (Li) [46], antimony (Sb) [47] or tellurium (Te) [48] to the activation process. An increase in lifetime with Li-enhanced activation has also been demonstrated at Photo-CATCH [43, 49]. However, for high current applications e.g. positron production the heating of the cathode due to the high laser power also plays an important role for the operational lifetime.

In the scope of this work, a new gun is developed and commissioned featuring an active cooling of the cathode to compensate for the introduced heat. In addition, the provided cooling power is used to increase the vacuum condition by placing the cathode in an almost closed cryogenic sub-volume which acts as a pump and significantly reduces the pressure inside. An integration of this source into Photo-CATCH is foreseen but was not possible during this work. The integration would require some reconstruction work including a rearrangement of the chambers and a modification of the beamline, which was not feasible as Photo-CATCH was in active use for other experiments. Therefore, a separated test stand featuring all required components to produce an electron beam and measure its current was designed and set up during this work. All components were designed in a way that they are fully compatible with Photo-CATCH for a future integration.

The goal of this work is to deliver a proof of principle and to demonstrate that a lifetime increase using cryogenic cooling is possible. The dissertation is structured in 6 chapters, starting with an overview of the relevant fundamentals on photocathodes in Chapter 2, followed by Chapter 3 covering the basics of ultra-high vacuum generation including vacuum pumps and in particular cryo pumps. In Chapter 4, the design of the gun and the test stand are presented, including an overview of the Photo-CATCH test stand. The assembly, the commissioning and first measurements of the cryo source are presented and discussed in Chapter 5. Chapter 6 concludes this dissertation with a summary and a brief outlook.

2 Fundamentals of Photocathodes

2.1 Polarized Electrons

A ensemble of electrons is considered polarized, if the electrons feature a preferred direction of the spin vector \vec{s} . This is in contrast to an unpolarized ensemble, where the directions of the individual electrons are distributed uniformly so that the spin vectors cancel each other as a result. The degree of polarization can be calculated as [50]

$$P = \frac{N \uparrow - N \downarrow}{N \uparrow + N \downarrow}, \quad (2.1)$$

where $N \uparrow$ represents the number of electrons with a spin oriented parallel to a chosen axis while $N \downarrow$ stands for electrons with an anti-parallel orientation.

Besides the degree of polarization, the current I_p of electrons (also called photocurrent) is another important aspect for experiments with electron beams. Both factors get combined to a figure of merit (FOM) of an electron source in the form [14]

$$FOM = P^2 \cdot I_p. \quad (2.2)$$

As the contribution of the polarization is quadratic, a high degree of polarization is desirable for experiments. However, as the degree of polarization cannot be increased beyond 100 %, providing intense beams is of equal importance for high-sensitivity experiments including polarization.

There are different approaches to produce spin-polarized electrons, such as β -decay, Mott scattering, optical pumping of unpolarized alkali atoms (Fano Effect) or ionization of polarized helium [13, 14]. However, all these methods are not a viable source for the high-intensity requirements of modern accelerators as they cannot deliver the required current and/or degree of polarization.

2.2 Photoelectric Effect

The most popular sources for polarized electrons used today utilize the photoelectrical effect, which was first observed by Hertz in 1887 [5]. The phenomenon has been studied deeper later on by Hallwachs, Lenard and others [51, 52]. They discovered that electrons get emitted from a solid (often called photocathode) when irradiated by light. Thereby a minimum frequency of the light, depending on the material used, is required to allow the emission of electrons. Increasing the light intensity is not sufficient if the minimum frequency is not given. Furthermore, the kinetic energy of the electrons only depends on the light frequency and not its intensity; solely the number of emitted electrons can be increased with raising light intensity.

These findings were not in accordance with theory at that time, which considered light to be a wave. This would anticipate the kinetic energy of the electrons to be proportional to light intensity. In 1905, Albert Einstein solved this contradiction by introducing a quantized light package called photon [6]. Only if the energy of the individual photons are high enough electrons can be emitted. As the energy transferred to the electrons is quantized, increasing the number of incident photons does not lead to emission if the photon energy is too low to excite an electron. The energy of a photon E_P depends on its frequency ν , or its wavelength λ , and can be calculated with Planck's constant h and the speed of light c

$$E_P = h \cdot \nu = \frac{hc}{\lambda}. \quad (2.3)$$

From this, the maximum kinetic energy of emitted electrons is given by

$$E_{kin} = E_P - W, \quad (2.4)$$

where W represents the *work function*, which describes the minimum energy needed to remove one electron from the cathode. It can be expressed as

$$W = e\phi, \quad (2.5)$$

with the elementary charge e and the electrostatic potential ϕ in the vacuum near the surface.

2.2.1 Three-Step Model

More than 70 years after the first observation of the photoelectrical effect, Spicer and Berglund developed a phenomenological model describing the process from excitation to emission of electrons from semiconductors, called the three-step model (TSM) [53–56].

Opposed to earlier theories which considered the photoelectrical effect to be a surface phenomena, it describes the emission as a bulk effect in three independent steps [57, 58]:

1. Electrons get excited from the valence band (VB) into the conduction band (CB) by the absorption of incident photons. The energy E_P of the photon must fulfill the requirement $E_P = h \cdot \nu > E_G$, where E_G represents the energy gap between the two bands. The intensity I_0 of the incident light gets reduced by reflection at the cathode surface and by absorption within the medium. The intensity $I(x)$ at the distance x in the material is given by

$$I(x, \nu) = I_0(\nu) \cdot [1 - R(\nu)] \cdot e^{-\alpha(\nu)x}, \quad (2.6)$$

with the light reflectivity $R(\nu)$, which takes the intensity loss due to reflection at the surface into account, and the absorption coefficient $\alpha(\nu)$ describing the intensity reduction by absorption inside the medium. Both are dependent on frequency. However, not every excited electron contributes to photoemission, only electrons with energies above the vacuum energy level are capable of escaping the cathode. To take this into account, a so-called reduced photo-emissive absorption coefficient α_{PE} is introduced. The probability P_{ex} to excite an electron above vacuum level, providing it with enough energy for emission, can than be expressed for a cathode layer dx by

$$P_{EX}(\nu, x, dx) = I_0(\nu) \cdot [1 - R(\nu)] \cdot \alpha_{PE} e^{-\alpha(\nu)x} dx. \quad (2.7)$$

2. The photo-electrons are now transported from the inside of the bulk to the cathode surface. On their way they are subject to elastic and inelastic scattering processes reducing their energy. As the chance to scatter is proportional to the distance traveled, the probability P_T of an electron to reach the surface with sufficient energy for emission can be expressed as

$$P_T(x, \nu) = e^{(-x/L_e(\nu))}. \quad (2.8)$$

The escape length L_e describes the distance after which a fraction of $1/e$ electrons retain enough energy to escape the cathode surface.

3. The last step covers the emission of the electrons into the vacuum, which is determined by the energy dependent escape probability P_E at the material surface. Electrons with sufficient kinetic energy to overcome the surfaces potential barrier can escape into the vacuum, the others are reflected back into the bulk material.

The differential intensity $di(x, dx, \nu)$ of the photo-emission from a layer dx in the cathode can be calculated by multiplying the probabilities of each step

$$di(x, dx, \nu) = P_{EX}(\nu, x, dx) \cdot P_T(x, \nu) \cdot P_E(\nu). \quad (2.9)$$

The total electron yield $i(\nu)$ can be determined for a cathode with infinite thickness by integrating over the differential intensity

$$i(\nu) = \int_0^\infty di(x) = I_0(1 - R) \frac{\alpha_{PE}}{\alpha + \frac{1}{L_e}} P_E(\nu). \quad (2.10)$$

Figure 2.1 shows a schematic representation of the three steps illustrating that a minimum photon energy of E_G is required to excite an electron from the valance band maximum (VB_{\max}) into the conduction band minimum (CB_{\min}). The energy difference E_A between CB_{\min} and the vacuum level is called the electron affinity (EA). An electron in the conduction band needs enough energy to overcome this barrier to leave the cathode surface. From this follows the criteria of photoemission, describing the minimal required energy for a photon to emit an electron [59]:

$$E_P = h \cdot \nu \geq E_G + E_A = e\phi + E_{VF}. \quad (2.11)$$

Here, E_{VF} refers to the energy difference between VB_{\max} and the Fermi energy E_F . Electrons, that do not fulfill this criteria fail to escape the surface and are recombined through radiative and non-radiative processes eventually.

The TSM is commonly used, as it has proven to be quite successful in predicting the behavior of photo cathodes in experiments. However, it is only a phenomenological approach. Since it assumes that the excitation takes place at a given spacial position before transportation and emission, and that the inelastically scattered electrons lose their energy after they have been excited, the TSM violates the uncertainty principle [60].

The one-step model solves this problem by describing photoemission as a scattering process in one step. Aspects like surface effects and the wave-particle duality of electrons are taken into account. However, this dissertation will not discuss this topic any further. For more information one may consult [60] and [61].

2.2.2 Quantum Efficiency

An important value to quantify the quality of a photo cathode is the quantum efficiency (QE) or quantum yield η . It is defined as the ratio of emitted electrons N_{e^-} to incident

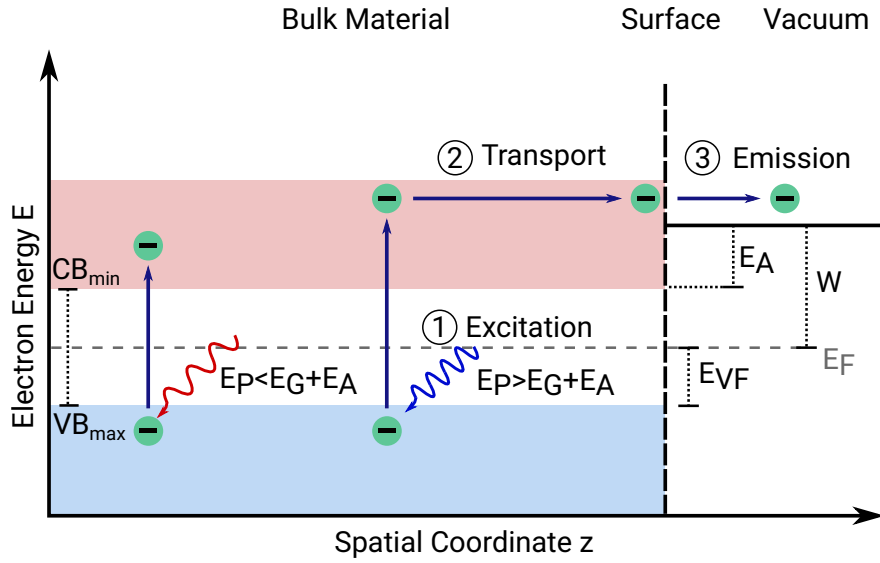


Figure 2.1: Coordinate Visualization of the emission of electrons from a semiconductor according to the three-step model by Spicer and Berglund. In step 1, an electron from the valence band maximum (VB_{\max}) is excited to the conduction band minimum (CB_{\min}). In step 2, the electron gets transported to the surface to be emitted into the vacuum in step 3, under the presumption that it has enough energy to overcome the electron affinity barrier. E_G , E_A , E_F , W and E_{VF} describe the band gap energy, the electron affinity, the Fermi energy, the work function of the material and the energy difference between VB_{\max} and the Fermi energy, respectively.

photons N_P . Using Equation (2.10), the quantum efficiency can be expressed as [57]

$$\eta = \frac{N_{e^-}}{N_P} = \frac{i(\nu)}{I_0(1-R)} = \frac{(\alpha_{PE}/\alpha) \cdot P_E}{1 + (l_a/L_E)}, \quad (2.12)$$

introducing the absorption length $l_a(\nu) = 1/\alpha$ as the inverse of the absorption coefficient. The term l_a/L_E in Equation (2.12) indicates a reduction of the probability for electrons to reach the surface with enough energy for emission if the absorption of the photons happens at a depth larger than L_E . The fraction of electrons excited above the vacuum level are represented by the ratio α_{PE}/α . The higher the ratio, the higher the QE a cathode can exhibit, while the ratio l_a/L is required to be small for the same result.

Table 2.1: Energy gap $E_G(0)$ at 0 K and material-dependent quantities α and β for GaAs [62].

$E_G(0)$	1.519(1) eV
α	$5.405(250) \cdot 10^{-4}$ eV/K
β	204(45) K

In practice, the quantum efficiency is often calculated from the measured photocurrent I_p , the power P_L and wavelength λ of the laser [63]

$$\eta(P_L, I_e, \lambda) = \frac{hc}{e\lambda} \cdot \frac{I_p}{P_L}, \quad (2.13)$$

with the electron charge e , the speed of light c and Planck constant h .

2.3 Gallium Arsenide Photocathodes

Due to the high beam quality and high degree of polarization gallium arsenide (GaAs) photocathodes can provide, they are predominantly used for electron sources for spin-polarized applications in the accelerator physics community today. They were first introduced as unpolarized photo emitters by Scheer and van Laar in 1965 [64], later proposed as polarized emitters by Lampel and Weisbuch [65] and established by Pierce, Meier and Zürcher in 1975 [66].

GaAs belongs to the semiconductor III/V group and shows a direct band-gap, meaning that the CB_{\min} and VB_{\max} are located at the same value of wave vector k . This restricts transitions between valance and conduction bands to vertical in momentum space and gives rise to a high absorption constant α near the band-edge. GaAs exhibits a so-called Zinc-Blende crystal structure, which consists of two face-centered cubic lattice displaced along a diagonal direction. A schematic representation of the crystal structure is shown in Figure 2.2. At room temperature, the energy gap E_G is about 1.42 eV corresponding to a wavelength of roughly 870 nm. For other temperatures, E_G can be calculated empirically using the Varshni equation [68]

$$E_G(T) = E_G(0) - \frac{\alpha \cdot T^2}{T + \beta}, \quad (2.14)$$

with the crystal temperature T in Kelvin, the energy gap $E_G(0)$ at 0 K and the material dependent quantities α and β for GaAs given in Table 2.1.

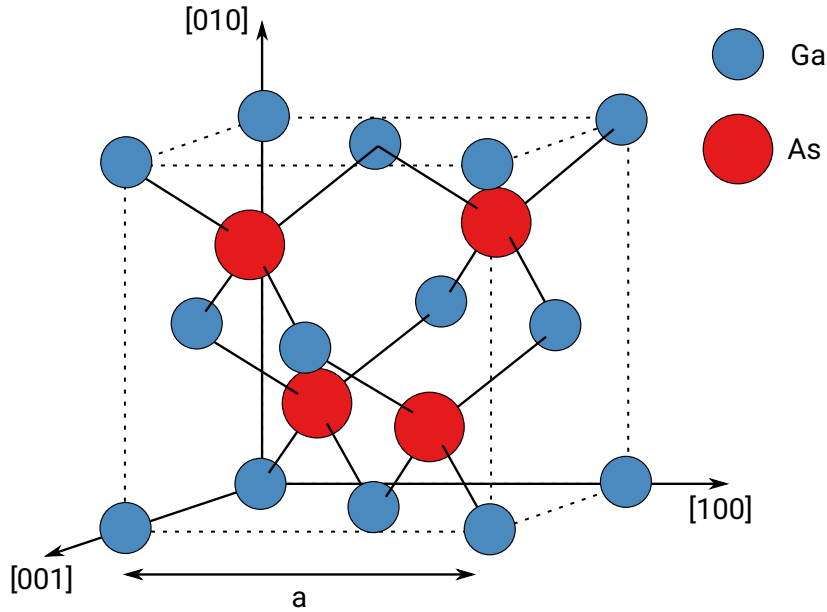


Figure 2.2: Crystal structure of GaAs with a volume of a^3 . Figure based on [67, Fig. 1].

The band structure of GaAs is well known and shown in Figure 2.3 . The CB_{\min} and VB_{\max} are located at the symmetry point where $k_x = k_y = k_z = 0$, denoted by Γ . Here the upper valence band is split by spin-orbit coupling, resulting in a $p_{1/2}$ (Γ_7) and $p_{3/2}$ (Γ_8) sub-band, separated by an energy gap of $\Delta_{SO} = 0.34 \text{ eV}$. The $p_{3/2}$ band is split additionally into the light-hole (lh) and heavy-hole band (hh), leading to a total of three twice-degenerated sub-bands for the upper valence bands. The CB_{\min} exhibits s-symmetry and is twice-degenerated. The resulting energy levels of the bands are shown in Figure 2.4. For more information on the properties of GaAs and its band structure, see [67],[69], [70] and [71].

Transition from Γ_{8hh} , Γ_{8lh} and Γ_7 to Γ_6 are possible when absorbing photons of energy $h\nu > E_G + \Delta_{SO}$. To create spin polarized electrons, photons with an energy of $E_G < h\nu < E_G + \Delta_{SO}$ are required to restrict transition to be only possible from the Γ_{8hh} , Γ_{8lh} valence band/the $p_{3/2}$ states to the conduction band/the $s_{1/2}$ states. Due to conservation of angular momentum, the magnetic quantum number m_j needs to change by +1 for circular polarized photons with helicity σ^+ and -1 for polarized photons with helicity σ^- . Using either one or the other, the possible transitions can be limited further to two allowed transitions. The relative transition probabilities can be calculated by the corresponding

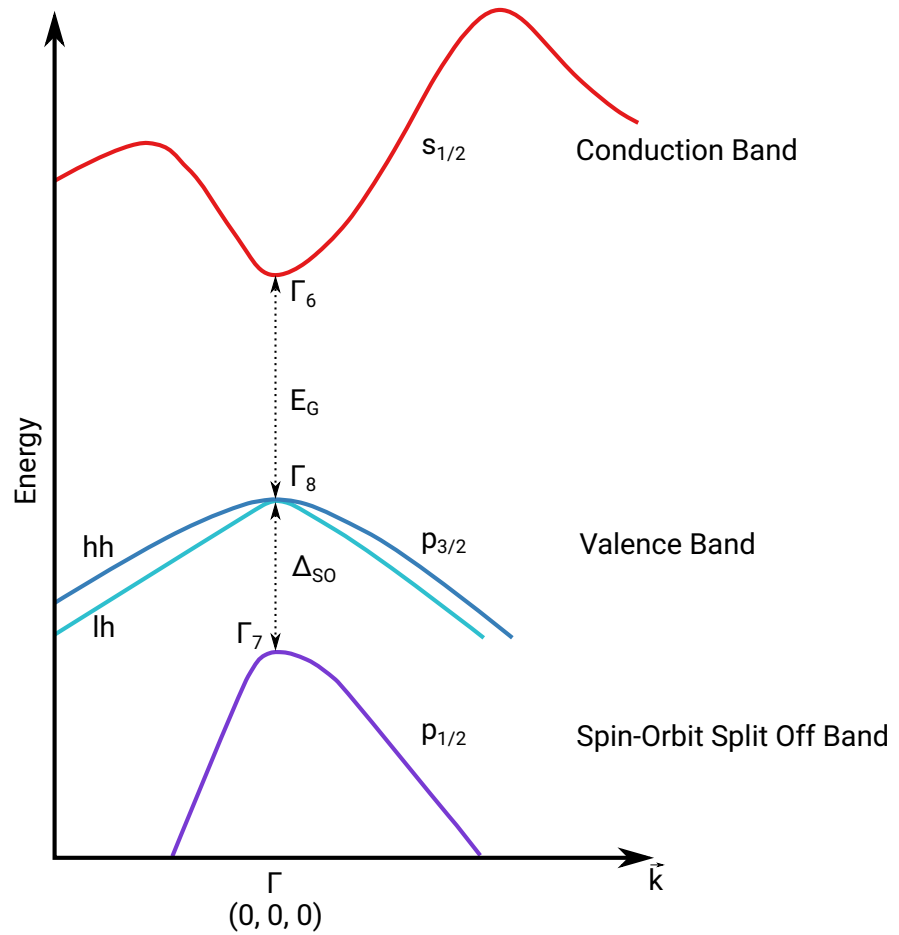


Figure 2.3: Schematic illustration of the band structure of GaAs near the Γ point. Γ_6 , Γ_7 , Γ_8 lie in the conduction band, the valence band (with the heavy-hole and light-hole sub-band) and the spin-orbit split off band, respectively. The latter is separated from the heavy-hole and light-hole band by an energy gap of Δ_{SO} , while the CB_{\min} and VB_{\max} are separated by an energy of E_G .

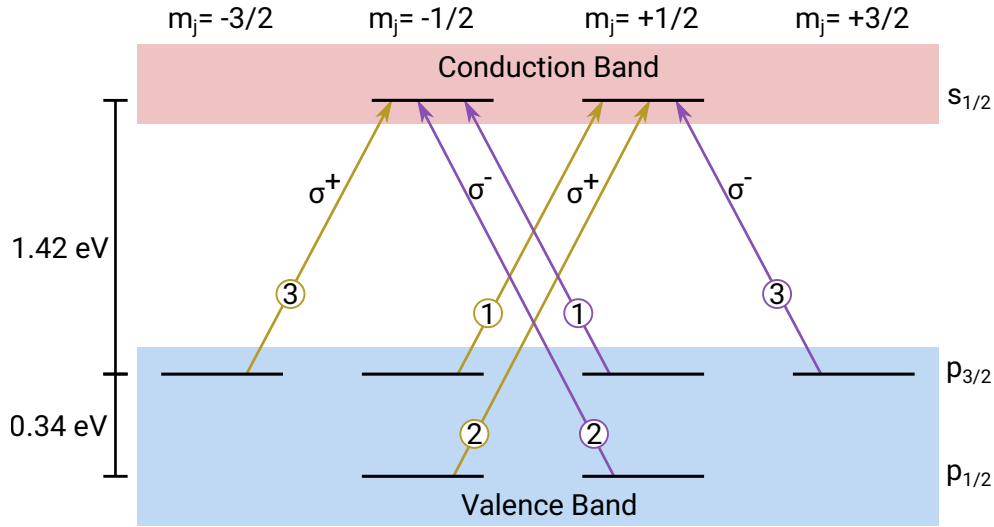


Figure 2.4: Schematic illustration of the energy levels and possible transitions for photo-excitation in bulk GaAs. Transitions between energy levels are represented by arrows labeled with σ^{\pm} for right or left circular polarized photons. The Clebsch-Gordan coefficients represents the relative transition probabilities and are given by circled numbers. Figure based on [72, Fig. 2].

Clebsch-Gordan coefficients, which are show in Figure 2.4. The probabilities directly correspond with the ratio of parallel to antiparallel spin oriented electrons. Plugging this ration into Equation (2.1), the maximal polarization theoretically possible calculates by

$$P_{+} = \frac{1 - 3}{1 + 3} = -0.5, \quad (2.15)$$

for σ^{+} -light and

$$P_{-} = \frac{3 - 1}{1 + 3} = 0.5, \quad (2.16)$$

for σ^{-} -light. The polarization vector \vec{P} of the electrons is oriented anti-parallel towards the angular momentum vector of the incident photons. When using light with an energy above $E_G + \Delta_{SO}$, transitions from $p_{1/2}$ become possible, resulting in a total transition probability ratio of $(2+1):3 = 1:1$, leading to a termination of the polarization. To increase the degree of polarization above 50%, special grown and doped GaAs are necessary.

2.3.1 Higher Degree of Polarization

Equation (2.15) and (2.16) show that the maximal theoretical polarization of normal GaAs cathodes (also referred to as bulk GaAs cathodes) is limited to 50%. As the FOM depends on the degree of polarization quadratically, a higher polarization is of great interest. The limiting factor for higher polarization is the degeneracy of the $p_{3/2}$ level. If it was possible to split this level in two two-fold degenerate sub-levels with an energy difference of ΔE_S (see Figure 2.5 and 2.6), the allowed transitions for circular polarized photons with an energy of $E_G < h\nu < E_G + \Delta_{SO}$ would be restricted to just one, effectively increasing $|P|$ to 1. This was first achieved in 1982 at SLAC by applying uni-axial mechanical stress to the crystal, using an apparatus, resulting in a polarization degree above 0.7 [73]. A different method to generate stress was proposed by Ciccacci et al. by growing a thin active epitaxial GaAs layer on a substrate with slightly different lattice constant [74]. Electron polarization of up to 90% were reported for different substrate layers such as GaAsP and InGaAs [75–78]. These types of cathodes are usually referred to as strained-layer cathodes.

Another approach to increase polarization is to create multiple, alternating layers of two different compounds with the same lattice constant but different energy gaps E_G . At the beginning of the 1990s, electrons with polarization of around 71% were achieved using these so-called superlattice cathodes [79]. Nowadays values up to 80% are possible [80].

When combining both approaches, cathodes with a polarization of up to 92% can be manufactured [81]. The quantum efficiency of these strained-superlattice cathodes is typically below 1%, which is higher than those of strained or superlattice cathodes alone, but still significantly lower compared to bulk cathodes, which can reach up to 10% quantum efficiency at 25% polarization [82]. This is due to the fact that the maximum layer thickness of strained cathodes of 100 nm is low compared to an absorption length l_a of 1 μm , leading to only 1/10 of the photons being used for photo absorption [83]. However, recent development demonstrated a greatly improved quantum efficiency of 6,4% at a polarization of 84% by integrating a distributed Bragg reflector (DBR) into strained GaAs/GaAsP superlattice photocathode [12]. Together with the cathode surfaces, the DBR creates a Fabry-Perot cavity, which reflects the laser light. Instead of only once, the light passes the cathodes many times leading to an increase in quantum efficiency.

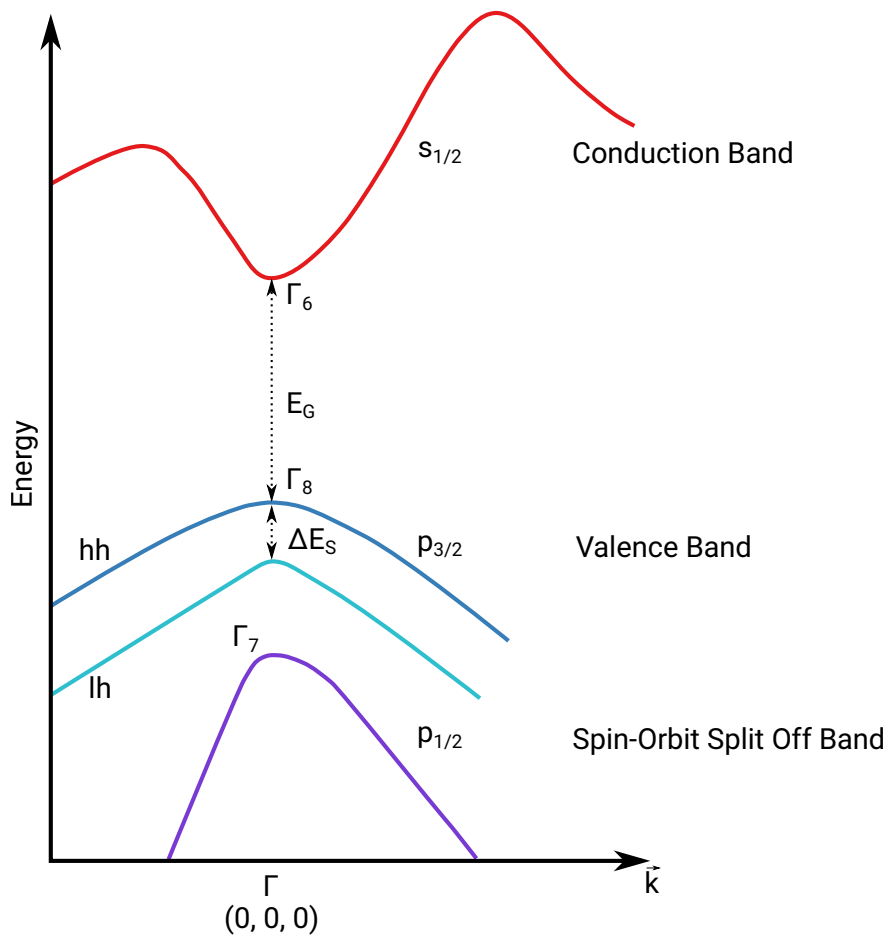


Figure 2.5: Band structure of strained-superlattice GaAs. The $p_{3/2}$ level gets split into two two-fold degenerate sub-levels due to the stress created by the strained-superlattice crystal structure. This separates the heavy-hole and light-hole sub-band by an energy of ΔE_S .

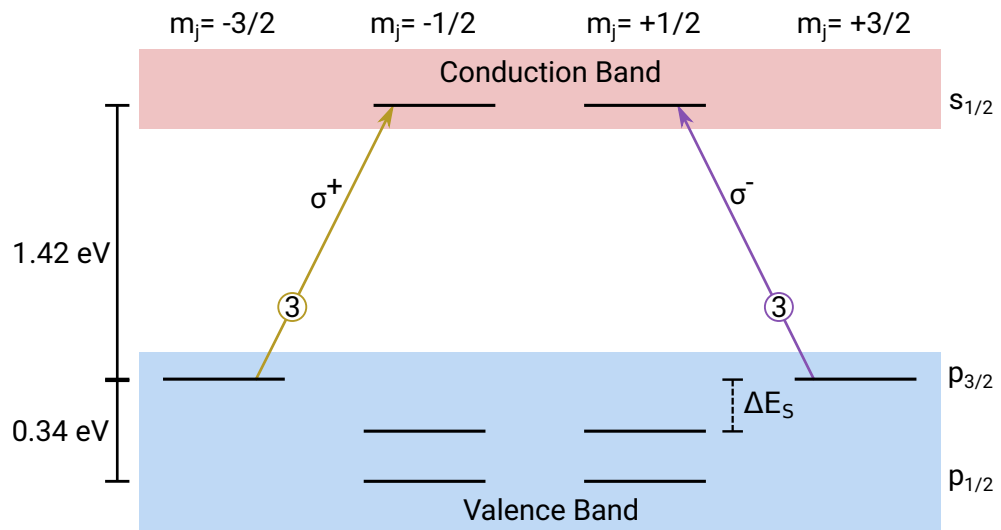


Figure 2.6: Schematic illustration of the energy levels and possible transitions for photo-excitation in strained-superlattice GaAs. Transitions between energy levels are represented by arrows labeled with σ^{\pm} for right or left circular polarized photons. The Clebsch-Gordan coefficients represents the relative transition probabilities and are given by circled numbers. Figure based on [72, Fig. 3].

Depolarizing Effects

Due to depolarization effects, the theoretical polarization degree of 100 % for strained and superlattice cathodes cannot be achieved experimentally. There are five effects that contribute to a reduction of polarization:

1. D'yakonov-Perel' process: a spin-dependent splitting of the conduction band due to the lack of inversion symmetry in III-V compounds,
2. Elliott-Yafet process: elastic scattering of the electrons by a perturbing potential,
3. hyperfine coupling: interaction between the electron \vec{s} and nuclear spin \vec{I} ,
4. Bir-Aronov-Pikus process: a relaxing effect of the exchange interaction between the electrons in the conduction band and the holes in the valence band, and
5. radiation trapping: creation of a new electron-hole pair due to capture of recombination radiation.

For more information see [84] for the first four and [85] for the last effect.

2.3.2 Escape into Vacuum

Equation (2.11) shows the threshold Energy E_P for a photon to cause photo-emission

$$E_P = h \cdot \nu \geq E_G + E_A = e\phi + E_{VF}.$$

Rearranging the rear part of this equation, an expression for the electron-affinity E_A can be given by

$$E_A = e\phi + E_{VF} - E_G, \quad (2.17)$$

with the band gap E_G , the work function $e\phi$, the energy difference E_{VF} between VB_{\max} and the Fermi energy E_F . It describes an additional barrier an electron has to overcome to escape from the cathode surface into vacuum. This is illustrated in Figure 2.7a. Bulk GaAs has an electron affinity of $E_A = 4.1$ eV, which is almost three times the band gap Energy of $E_G = 1.42$ eV at room temperature [86]. Therefore, no emission of spin-polarized electrons using bulk GaAs is possible with excitation near the energy band gap, which is necessary to achieve a high degree of polarization.

Hence, a reduction of the threshold energy E_P is necessary to enhance the photo-emission yield. As Equation (2.11) shows, this can be realized by either reducing the band gap energy E_G or the electron affinity E_A . The former can only be lowered by increasing the cathode temperature considerably. However, this is not practical for technical applications. So a reduction of E_A remains to increase the photo-emission yield. Equation (2.17) shows that this must be done by a reduction of the work function $e\phi$ and/or the Fermi energy E_F , which results in a reduced E_{VF} . Both can be achieved by a combination of p-doping and coating the surface with a thin layer of caesium (Cs) and an oxidant. This has been demonstrated first by Sheer and van Laar in 1965 by using a zinc doped GaAs photocathode coated with Cs [64].

The effects of p-doping of different semiconductors aiming at a reduction of electron affinity has first been shown by Spicer in 1958 [53]. It introduces impurities with less electrons to the cathode acting as acceptors. This alters the cathodes electronic structure by introducing an additional acceptor level, leading to a re-positioning of the Fermi level inside the material almost down to the level of the valence band maximum at Γ . At the surface the doping creates a space-charge region, which bends down both bands. This leads to a reduction of the effective electron affinity χ_{eff} , which is defined as the difference between the vacuum energy E_0 and the non-lowered edge of the conduction band (see Figure 2.7b). The magnitude of this effect depends on the doping concentration and can be found for GaAs cathodes in [89]. The area in which the bands are bent is called the band bending region. Its width can be calculated from the dielectrical constant ϵ_s , the doping density n_p , and the band-bending energy E_{BB} , which is typically half the

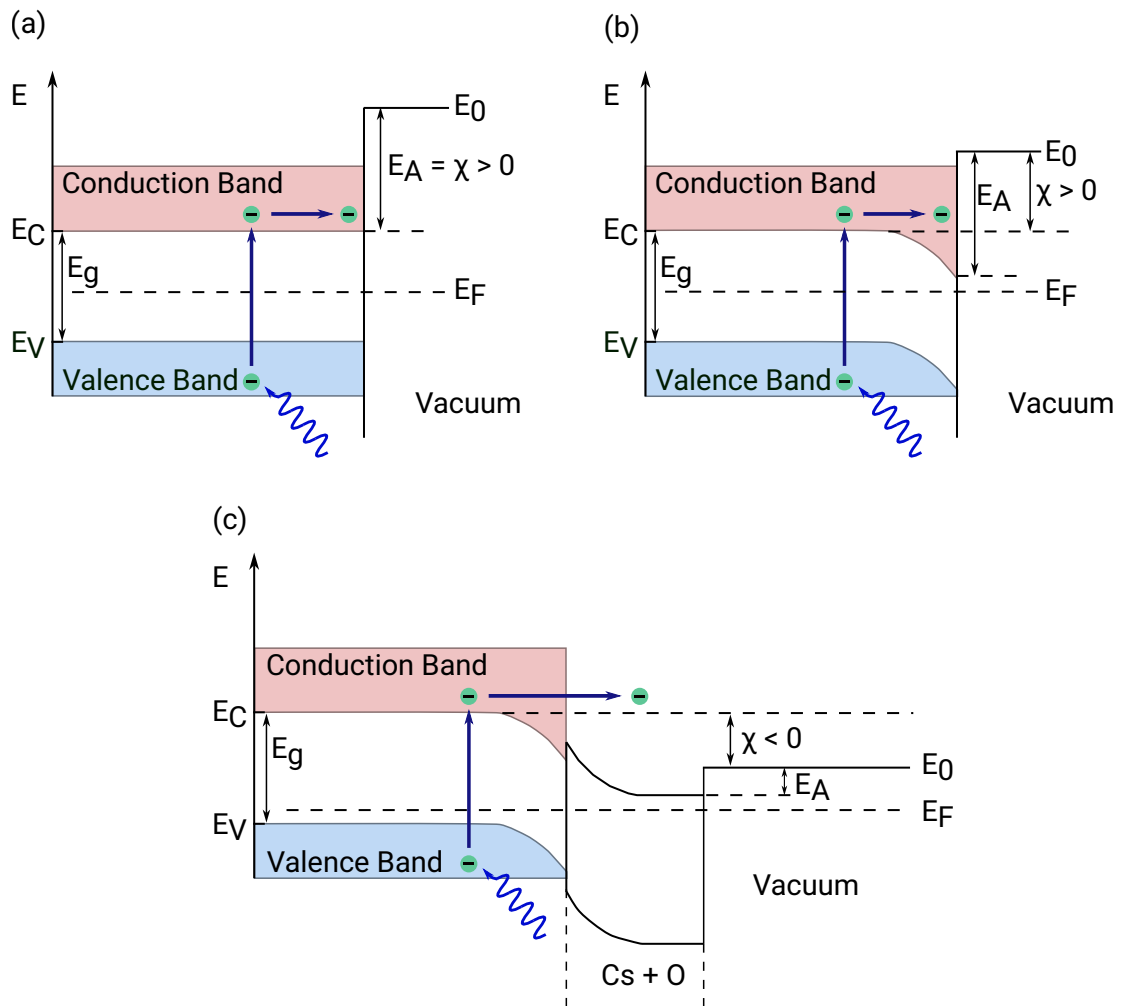


Figure 2.7: Schematic representation of the energy levels on the surface of a GaAs cathode. (a) In undoped bulk GaAs, the electrons require energies far greater to overcome the electron affinity E_A barrier. (b) P-doping of the cathode reduces the Fermi energy E_F and results in a bending of the bands at the surface. For emission, the excited electrons now only need enough energy to overcome the effective electron affinity χ_{eff} . (c) A layer of caesium and oxidant reduces the effective electron affinity further to a value below zero. Now electron emission for excitation near the energy gap of GaAs is possible. Figure based on respective figures in [64, 86–88].

Table 2.2: Values used to calculate the width of the band bending region for a typical p-doped GaAs cathode.

ϵ_s	12.85	[71]
n_p	10^{19} cm^{-3}	[90]
E_{BB}	0.7 eV	[90]

band gap energy. Using the values from Table 2.2 for a typical p-doped GaAs cathode and the vacuum permittivity ϵ_0 , it can be approximated to [90]

$$d_{BBR} = \sqrt{\frac{2\epsilon_0\epsilon_s \cdot E_{BB}}{2\pi \cdot e^2 \cdot n_p}} \approx 2.8 \text{ nm}. \quad (2.18)$$

More details on the effects of p- and n-doping of GaAs and other semiconductors can be found in [54], [91] and [92].

As the band bending only reduces the effective electron affinity by 0.9 eV [93], p-doping is not sufficient to provide effective electron emission. Therefore, it is combined with the coating of the cathode surface with a thin layer of Cs and an oxidant such as O₂, F or NF₃. The effect of a Cs-only coating of GaAs was first reported by Sheer and van Laar in 1965 [64]. Two years later, Turnbull and Evans increased the stability and effectiveness of the coating by introducing O₂ to the process [15]. Cs, as an electro-positive metal, reduces the electron affinity as it forms a dipole layer at the surface. This cuts down the effective electron affinity χ_{eff} below zero and is usually referred to as a negative-electron-affinity. The effect of the coating on the bands and energy levels is shown in Figure 2.7c. The technical process of applying this coating is called activation and will be discussed more detailed in the next section.

2.3.3 Cathode Activation

The process of applying a negative electron affinity layer on top of a photocathode is called activation. For GaAs, this is typically achieved with a layer of Cs and O₂ or NF₃. Studies showed no significant differences in lifetime for both oxidants, only different time evolution were observed [16]. As in this work O₂ is used for all conducted activations and the procedure with NF₃ is equivalent, from here on, only the term oxygen or O₂ will be used representing both oxidants.

The achieved lifetime and quantum efficiency is highly depended on the exact activation procedure, including the used amount of the elements and the order in which they are applied. There are a few commonly used activation schemes, which are still subject to recent research. Each start with the application of a caesium layer but differ in the sequence for adding oxygen. Because of its simplicity, only the so-called co-deposition is used in this work and will be described in more detail here. An overview of alternative activation schemes can be found in [49].

Before any activation can be carried out the cathode needs to be placed in an ultra-high vacuum (UHV) environment with a pressure below 10^{-10} mbar (see Section 3.1 for more information on vacuum classifications). The next step is the cleaning of the cathode to remove any unwanted contamination on the surface. This is done by heating the cathode to a temperature of around 650°C for some time [94]. In addition, a cleaning procedure with atomic hydrogen can be conducted, which removes oxygen and carbon more effectively than conventional thermal cleaning [95–97]. During the activation procedure the photocurrent needs to be measured to determine the right times to switch on and off the exposure of caesium and oxygen. This is usually performed with an anode ring and a low powered laser spot on the cathode surface (see Chapter 4.2.2 for a detailed description of the activation setup used in this dissertation). For the co-deposition activation scheme, a caesium layer is applied using an evaporator or dispenser until the photocurrent reaches its maximum. Now oxygen is introduced, while maintaining caesium exposure at the set rate. The oxygen can either be introduced in gaseous form through a leak valve or also via a dispenser. Once the photocurrent reaches a plateau, both supplies are turned off. The exact time for oxygen exposure can be delayed to improve the process. It is commonly started when the photocurrent peak caused by caesium exposure has fallen to about 75 % of its maximum. Figure 2.8 shows the photocurrent development over time for a typical co-deposition activation. Recent research studies the addition of other elements to the activation process to enhance quantum efficiency and lifetime of the NEA layer (see next section for more information on lifetime). The metalloid antimony [98], the alkali metal lithium [43, 46, 49] and tellurium [48] have been reported to have a positive effect.

2.3.4 Surface-Layer Decay and Lifetime

After activation, the quantum efficiency decays over time due to a deterioration of the NEA coating. This limits the operational lifetime of GaAs photocathodes. The observed trend of the photocurrent $I_p(t)$ can be described by an exponential decay in the form of

$$I_p(t) = I_p(0) \cdot e^{-t/\tau}, \quad (2.19)$$

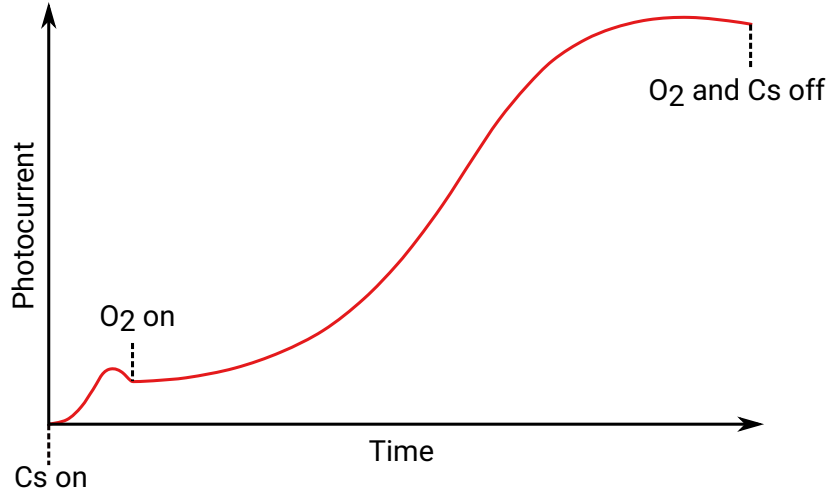


Figure 2.8: Development of the photocurrent over time for a typical co-deposition activation with caesium and oxygen. The times when Cs and O₂ exposures are turned on and off are marked.

where the decay constant τ , which is defined as the time until an extracted photocurrent $I_p(t)$ drops to a fraction of $1/e$ of its initial value, is interpreted as the lifetime of the cathode¹.

When using a laser with constant wavelength and power, the development of the quantum efficiency $\eta(t)$ follows the same exponential decay [99]

$$\eta(t) = \eta(0) \cdot e^{-t/\tau}. \quad (2.20)$$

The total lifetime τ can be split into two parts: the dark lifetime τ_d , which is defined as the decay of quantum efficiency regardless of the extracted charge amount and the charge lifetime Q_τ (also called operational or beam lifetime), which describes the decay depending on the amount of extracted charge. The latter is expressed in the unit of charge rather than time. With these definitions, Equation (2.20) can be rewritten as

$$\eta(t) = \eta(0) \cdot e^{-t/\tau_d} \cdot e^{-\int I(t)dt/Q_\tau}. \quad (2.21)$$

If the photocurrent is kept constant, during lifetime measurement by increasing the laser power accordingly, this yields

$$\eta(t) = \eta(0) \cdot e^{-t(1/\tau_d + I_p/Q_\tau)}. \quad (2.22)$$

¹If the lifetime of the cathode is mentioned, the author actually refers to the lifetime of the NEA layer.

The total lifetime τ can now be expressed as a reciprocal sum of the dark and charge lifetime

$$\frac{1}{\tau} = \frac{1}{\tau_d} + \frac{I_p}{Q_\tau}. \quad (2.23)$$

For a constant extracted current I_p , the charge lifetime Q_τ can be transformed into a charge lifetime τ_C in units of time by

$$\tau_C = \frac{Q_\tau}{I_p}. \quad (2.24)$$

Both dark and charge lifetimes can be further separated, depending on the involved lifetime-limiting effects. They are described hereinafter, following along the lines of [49]:

- **Residual-Gas Adsorption**

Even under best vacuum conditions, residual gas particles are present in the system. These particles get adsorbed on the CsO coating and change its properties, decreasing the quantum efficiency. The elements carbon, oxygen, chlorine and sulfur have been observed on the cathode [100]. Chanlek et al. investigated the degeneration effect of different residual gases and found that H₂, CH₄ and N₂ do not contribute significantly to a reduction of the quantum efficiency, while CO has a minimal and CO₂ and O₂ the strongest effect [101]. Figure 2.9 shows the quantum efficiency decay of the cathode when exposed to these gases. This behavior can be explained by a bond of oxygen with the surface, as oxygen accepts electrons from caesium and weakens the dipole activation, increasing the potential barrier of the layer and the vacuum, similar to an over-oxidation during the activation process. They also found that through a re-caesiation process, the quantum efficiency can be recovered almost completely (95 %) after exposure to O₂ and partly (60–70 %) after exposed to CO₂ or CO.

In addition to CO₂ and O₂, water vapor has a strong poisoning effect on the cathode. Even small amounts reduce the lifetime significantly. Durek et al. explained this by an over-oxidation of the cathode with water, as the quantum efficiency can also be restored by a re-caesiation [102], while Wada et al. suspects the H₂O molecules to be dissociated into H and OH by ion pumps [103].

As residual gas adsorption entirely depends on the vacuum condition, the lifetime characterizing the associated decay is often referred to as vacuum lifetime τ_{vac} . The process occurs independent from photoemission and therefore, contributes to dark as well as charge lifetime. When the cathode is not on a potential (grounded), is not illuminated and at room temperature, vacuum lifetime is the only term contributing to the dark lifetime ($\tau_d = \tau_{vac}$).

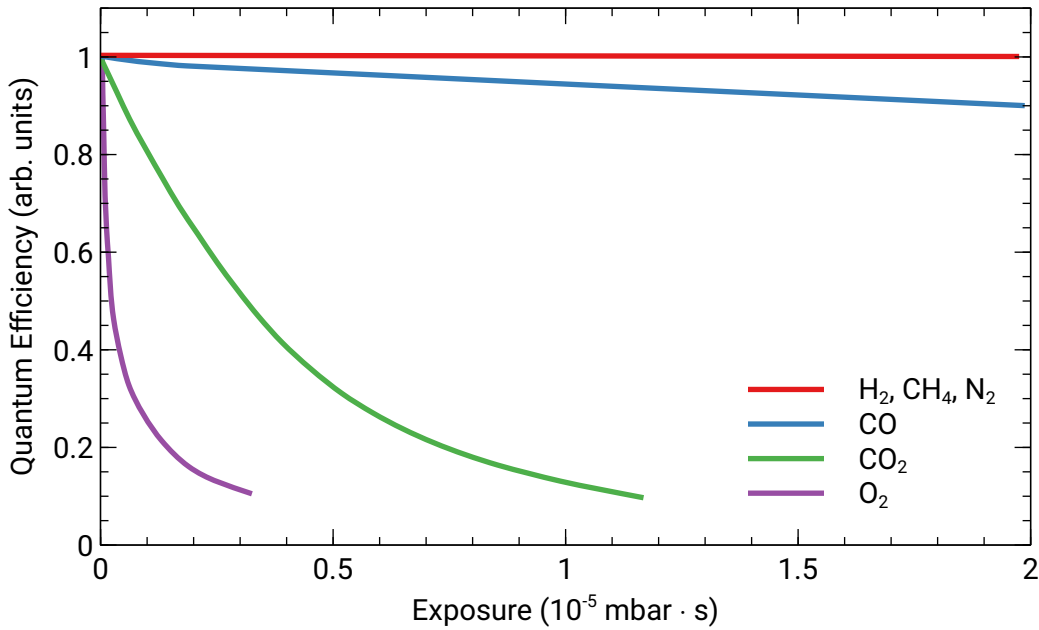


Figure 2.9: Decay of the quantum efficiency of an activated GaAs cathode, when exposed to different gases. Source of data: [101].

- **Thermal Desorption**

The rate of NEA layer decay increases with rising temperature due to thermal desorption of the layer materials [104, 105]. The rate dn/dt of this desorption can be expressed as an Arrhenius equation [105]

$$\frac{dn}{dt} = -n\nu_t \cdot e^{-\frac{E_B}{k_B T}}, \quad (2.25)$$

where n defines the amount of atoms bound to surface per unit area, E_B is the binding energy, ν_t a rate constant, k_B the Boltzmann constant, and T describes the cathodes temperature. From this, the temperature-dependent thermal desorption lifetime τ_{td} can be deduced as [105]

$$\tau_{td} = \frac{1}{\nu_t} \cdot e^{\frac{E_B}{k_B T}}. \quad (2.26)$$

As the NEA layer for GaAs cathodes consist of two elements, the desorption of both can contribute to QE decay. To calculate the contribution of Cs desorption, one

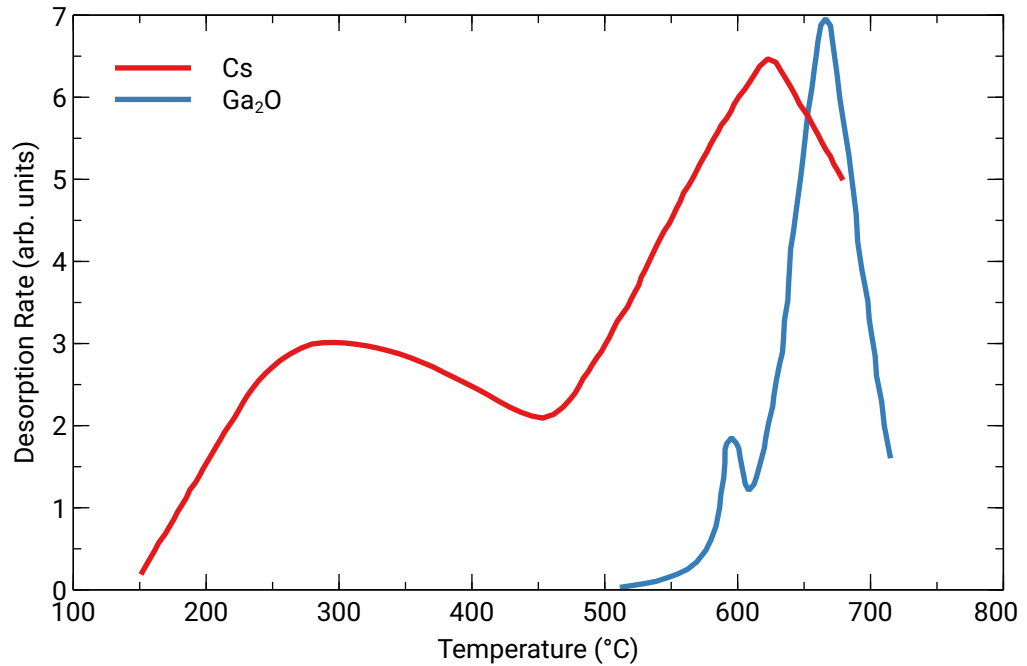


Figure 2.10: Thermal desorption rate for caesium and gallium (in the form of Ga₂O) for different temperatures. Source of data: [106].

can assume a rate constant of $\nu_t = 10^{13} \frac{1}{s}$ and a binding energy of $E_B = 1.6$ eV, for a typical activated GaAs cathode [104]. Using these values, a thermal caesium desorption lifetime at room temperature ($T = 300$ K) of around 2.4 million years can be approximated.

In contrast to caesium, oxygen binds with Ga and gets desorbed as Ga₂O. However, this phenomenon also does not occur significantly at room temperature, as shown by Goldstein and Szostak [106]. While significant Cs desorption starts at 150 °C, O₂ desorption starts at even higher temperatures above 500 °C. Figure 2.10 shows the thermal desorption rate for both, Cs and O₂ at different temperatures. At room temperature, thermal desorption in total can be neglected. However, the cathode itself can be significantly hotter than its surroundings, due to heating during operation by the incident laser light. This rise in temperature is highly dependent on the power and the spot size of the laser used.

Table 2.3: Temperature rises for some existing and planned electron sources [109]. Values are calculated using Equations (2.13) and (2.27), the thermal conductivity of GaAs at room temperature $0.455 \text{ W cm}^{-1} \text{ K}^{-1}$ [107], a laser wavelength of 780 nm, a quantum efficiency of 1% and a reflection coefficient of 0.57.

Source	Laser Spot (mm)	Current (mA)	Power	Temperature Rise (K)
CEBAF	0.05	0.2	31.8 mW	2.2
eRHIC	0.3	50	7.9 W	92.9
Cornell ERL ²	0.15	100	15.9 W	374.5
JLEIC	0.15	0.006	0.95 mW	0.023
LHeC	0.25	25	3.97 W	56.1

The maximum temperature rise induced by a laser with power P_L and a spot diameter ω ($1/e^2$, Gaussian beam), on a surface with temperature-dependent thermal conductivity $K(T)$ can be approximated by [107]

$$\Delta T \approx \frac{P_L}{\sqrt{2\pi} \cdot K(T)\omega}. \quad (2.27)$$

As not all light gets absorbed by the cathode, the reflection at the surface has to be taken into account, too.

For GaAs and a typical wavelength of 780 nm (see Section 4.7), a reflection coefficient of around 0.57 was measured [108]. Existing and planned electron sources use laser spot sizes from 0.15 mm to 5 mm, while the average electron current varies from 0.006 mA to 100 mA [109]. Using Equation (2.13) and assuming a cathode with 1% quantum efficiency, the required laser power ranges from around 2.4 mW to around 16 W. Table 2.3 shows the calculated values for some existing and planned sources. These calculations only hold true as long as the thermal conductivity of the cathode to its surrounding mount is at least as high as the conductivity of the cathode itself. This criterion is often not met, and higher temperatures are reported [110, 111]. But even under ideal circumstances, the temperature rise can reach over 300 K for high-current sources. This leads to the conclusion that the question whether thermal desorption can be neglected or if an active cooling of the cathode is needed highly depends on the parameters of the source.

The effect of thermal desorption is used to clean the cathode before the activation procedure.

²This source uses K_2CsSb cathodes.

- **Ion Back-Bombardment**

To accelerate the extracted electrons away from the cathode, either a negative potential applied to an electrode and the cathode itself, a positive potential applied to an anode or both are used. On their way, the electrons gain enough energy to ionize residual-gas molecules in collisions [112]. These ions, due to their positive charge, are then accelerated backwards onto the cathode, where they cause severe damage to the NEA layer. This effect is called ion back-bombardment (IBB) and was first described for photo cathodes by Schade et al. [113]. Ions can be produced either near the cathode surface between electrode and anode or in the beam line further away. In the latter case, the ions can drift back inside the beam to the cathode and increase the rate of ion back-bombardment [114]. As hydrogen is the dominant gas species in the vacuum chamber after bake-out (see Section 3.1), it contributes the most to IBB [115].

At the surface, the impinging ions reduce quantum efficiency in two ways. At lower energies, the bombardment sputters away the molecules that constitute the NEA surface [41, 116], while at higher energies, the ions get incorporated into the crystal structure [115, 116]. Both significantly reduce the lifetime of the NEA layer, however, the first effect is reversible through cleaning and reactivating the cathode while the ability to recover from the second effects depends on the energy of the ions [115].

The total number N_i of ionized gas molecules can be calculated by [117]

$$N_i = \rho_i \cdot \sigma_i \cdot l \cdot N_e, \quad (2.28)$$

with the density ρ_i and the ionization cross section σ_i of the residual gas as well as the number of electrons N_e and the distance l they have traveled.

There are some techniques to reduce the amount of IBB, e.g. the use of an anode as a positive potential barrier to inhibit the reflux of trapped ions inside the beam [114]. An offset of the anode to further reduce IBB has been proposed by Rahman et al. [118]. Another approach is to use a magnetic field to deflect the ions [113]. As can be seen from Equation (2.28), better vacuum conditions and therefore, lower density of residual gas molecules are beneficial in all cases. In addition, a lower pressure reduces residual-gas desorption. Therefore, this work focuses on increasing the vacuum conditions through cryopumping (see Chapter 3.4).

As IBB only occurs while electrons are emitted, IBB lifetime τ_{IBB} only contributes to the operational lifetime. Under the assumptions of a constant electric field, a fixed potential, and a symmetric gun geometry, one can assume IBB lifetime to be

proportional to the ratio of the beam area A_{EB} and electric field E , to the pressure p and the current of electrons I_p [83] like

$$\tau_{IBB} \propto \frac{A_{EB}E}{p_p I_p}. \quad (2.29)$$

- **Field Emission**

When an electric field on a metal surface is strong enough, it will overcome the restrictive forces, allowing electrons to tunnel through the potential barrier and be released from the surface into the surrounding vacuum. This is referred to as field emission. When electrons emitted this way hit the walls, they release secondary electrons and ions into the chamber, called electron-stimulated desorption (ESD) [119]. This increases the pressure and therefore, IBB and residual-gas adsorption. The emerging heat also increases thermal desorption [120]. As a consequence, field emission has no direct influence on the lifetime but affects it indirectly by increasing the other lifetime-limiting effects. In the worst case, it can lead to a complete voltage breakdown of the cathode-anode gap and damage the electrode, the insulators as well as the high-voltage power supply. However, by designing the electrode in a way that limits the field gradient at its surface [121] and by conditioning the gun before operation [23], field emission can be reduced to a level that can be neglected for quantum efficiency decay.

3 Ultra-High Vacuum

3.1 Fundamental Concepts

Not only for electron guns but for almost all particle physics experiments, the absence of other interfering particles is of great relevance. Therefore, in sources and accelerators excellent vacuum conditions need to be maintained. Since this is particularly important for the lifetime of electron guns based on GaAs cathodes, this chapter presents the key aspects of generating and maintaining high vacuum.

A Vacuum is defined as a volume with a lower pressure than in the surrounding volume. In experimental physics this is usually achieved by a set of different pumps, which either transport the gas from within the volume to the outside or capture the molecules inside the pump. The types of pumps used in this experimental setup are described in Section 3.3.

The effectiveness of a vacuum pump is usually measured in pumped volume per time (e.g. l/s), which is called the pumping speed S . Often, the pump is not directly attached to the experimental chamber but connected through pipes with different diameter and/or angles. This reduces the effective pumping speed S_{eff} , which can be calculated through [122]

$$\frac{1}{S_{eff}} = \frac{1}{S} + \frac{1}{C}. \quad (3.1)$$

The conductance C of the connecting elements can be calculated only for simple geometries like pipes or apertures. For more complex setups, solely measurements or simulations can provide reliable values. Multiple elements in series with known conductance can be added reciprocally like [122]

$$\frac{1}{C_{tot}} = \sum_1^n \frac{1}{C_n}. \quad (3.2)$$

If we introduce the flow resistance W as the reciprocal of the conductance

$$W = \frac{1}{C}, \quad (3.3)$$

Equation (3.2) becomes

$$W_{tot} = \sum_1^n W_n, \quad (3.4)$$

and for multiple elements in parallel,

$$\frac{1}{W_{tot}} = \sum_1^n \frac{1}{W_n} \quad (3.5)$$

holds.

The amount of gas in a volume can be measured by its mass. However, for vacuum applications, the product of volume and pressure ($p \cdot V$) is of more interest. In this dissertation, the outcome of this product will be called gas load. It has the dimension of an energy and is measured in mbar·l. From this, one can calculate the mass, if the temperature is known, using the ideal gas law [122]

$$m = \frac{p \cdot V \cdot M}{R \cdot T}, \quad (3.6)$$

where T represents the temperature of the gas, R the ideal or universal gas constant and M the molar mass. The gas load divided by time t is called the gas-flow rate and can be used to describe the throughput of a vacuum pump, often denoted by the letter Q [122]

$$Q = \frac{p \cdot V}{t} = \frac{d(p \cdot V)}{dt}. \quad (3.7)$$

This pump throughput should not be mixed up with the pumping speed S . The throughput is the gas load transported by the pump in one unit of time, measured in mbar·l/s, whereas the pumping speed is the provided transport capacity of the pump measured in l/s. For a constant pressure and volume, Q can be calculated from S by [122]

$$Q = p \cdot S. \quad (3.8)$$

For an element with conductance C with different pressures p_1 and p_2 on both ends, the gas flow from one side to the other can now be calculated as

$$Q = (p_1 - p_2) \cdot C = \Delta p \cdot C. \quad (3.9)$$

When dealing with multiple vacuum ranges, a clear definition of vocabulary for classification is beneficial. The vocabulary used in this dissertation follows the ISO norm 3529-1:2019, where vacuum pressure ranges are categorized into five groups, from atmospheric pressure of ~ 1000 mbar to below 10^{-11} mbar. The exact ranges are given in Table 3.1.

Table 3.1: Vocabulary used in this work to classify different vacuum ranges, following the ISO 3529-1:2019 norm.

Technical Term	Pressure Range (mbar)
low/rough vacuum (RV)	1000 - 1
medium/fine vacuum (FV)	1 - 10^{-3}
high vacuum (HV)	10^{-3} - 10^{-8}
ultra-high vacuum (UHV)	10^{-8} - 10^{-11}
extreme-high vacuum (XHV)	below 10^{-11}

3.2 Achieving Ultra- and Extreme-High Vacuum

To achieve a vacuum in the UHV or XHV regime, one has to assess all sources of gas flow into the system, as they are the primary limiting factor to reach a lower pressure. After pumping down, this flow is composed of the following parts [43]

$$Q_{tot} = Q_{out} + Q_{per} + Q_{dif} + Q_{lea} + Q_{pro}, \quad (3.10)$$

where Q_{out} refers to the outgassing of the chamber walls, Q_{per} and Q_{dif} describe gases entering the chamber by permeation and diffusion through the material of the chamber and Q_{lea} represents gas entering the volume through either real or virtual leaks. The last term Q_{pro} describes the process gas, which is introduced into the system on purpose for specific processes such as the hydrogen flow during atomic-hydrogen cleaning of a photo-cathode. To achieve a vacuum in the UHV or XHV regime, all individual components need to be minimized as much as possible.

The major contribution to the total gas load in the sub-UHV regime are leaks. They are split into two types, real and virtual. Real leaks are small holes in the boundary of the volume, often caused by gaps in the weld or an insufficient or incorrect tightened flange; whereas the gas load from virtual leaks does not come from outside of the system but from gas trapped in pockets within the chamber, such as the thread of a screw. It is often difficult to distinguish between those two, because both result in an increased pressure in the system. Real leaks can be identified using a leak tester and a tracer gas (e.g. helium). Once found, the leak can be repaired by replacing the metal-gasket of the flange or fixing the faulty weld.

Virtual leaks are harder to isolate, as they cannot be traced externally. Therefore, they need to be prevented by taking extra care during chamber manufacturing and assembling,

for example by placing venting holes in screws and near other possible gas traps. Depending on the size of the gas pocket, they may vanish after a certain time through outgassing, but will reappear after a chamber vent.

The second major factor to the gas flow comes from the outgassing of the chamber walls and other components in the system (Q_{out} and Q_{per}). The outgassing rate depends on the material and is proportional to temperature and inversely proportional to pressure. There are two commonly used procedures to reduce outgassing. The first step is a systematic cleaning procedure of all parts to remove contamination [123]. The cleaning procedure used in this work follows these four steps:

1. Wiping with clean cloth soaked in isopropanol,
2. ultrasonic bath, alternately with/without material dependent detergent and hot/cold deionized water (usually two times),
3. drying in clean room or hot-air oven, and
4. assembling in clean room or packing in polyethylene bags.

When a vacuum system is exposed to air, the water vapor contained in the atmosphere will contaminate the system. The water molecules will bond to the surface material by strong chemical adsorption forces. On top, further layers will build up by physical van der Waals forces. When pumping down, the water molecules are released into the chamber, very slowly at first, increasing greatly as the pressure falls to the molecular-flow regime. Now the pressure remains constant until the water is released completely and pumped out of the system [124]. As this process takes fairly long, one can accelerate the desorption of water and other reactive gases bound to the surface (O_2 , H_2 , CH_4 etc.) by heating the system to a temperature between $120^\circ C$ and $400^\circ C$, enabling to reach UHV conditions much faster. XHV conditions cannot be obtained within reasonable timescales without using this method to desorb water from the metal walls of the chamber. This procedure is called bake-out and takes several hours to weeks, depending on material, temperature and contamination level. The pressure during bake-out will rise due to the desired desorption of gas contamination. After cool-down the pressure will fall and hydrogen will be the prominent gas species in the system, mainly caused by diffusion of dissolved H_2 in the chamber walls (Q_{dif}). Figure 3.1 shows the residual gas spectra of the aluminum chamber used for the cryo source (see Section 4.5) before and after bake-out. As can be seen, the partial pressure drops by multiple magnitudes depending on the gas type.

When using a stainless-steel chamber, hydrogen diffusion can be reduced by annealing the material at high temperatures. The duration of this process depends on the temperature

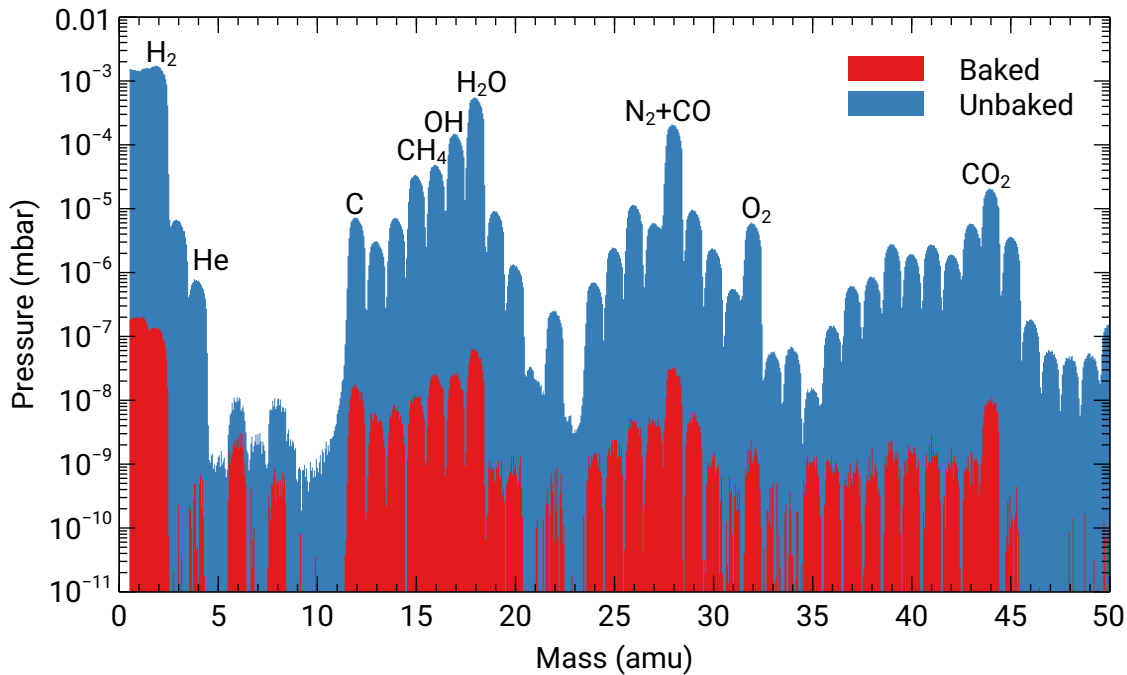


Figure 3.1: Spectrum of the residual gas inside the aluminum cryo gun chamber used in this work before and after bake-out. H_1 and CO is created by cracking of H_2 and CO_2 at the residual-gas-analyser filament. The internal photomultiplier of the RGA was used for both measurements, therefore, it is not possible to make a statement on the absolute pressures.

used, from a few hours at ~ 950 °C to days at ~ 400 °C [125, 126]. This process is called vacuum firing and is necessary to reach XHV when using stainless-steel chambers. For aluminum chambers, like the ones used in this work, vacuum firing is not possible but also not necessary to reach comparable outgassing rates.

3.3 Vacuum Pumps

There is no single pump that can directly pump down a chamber from atmospheric pressure to UHV or XHV conditions. Therefore, a set of pumps with different working principles is required. The first stage is usually a positive displacement pump like a diaphragm or rotary vane pump transferring the gas from within the system to the outside. They can

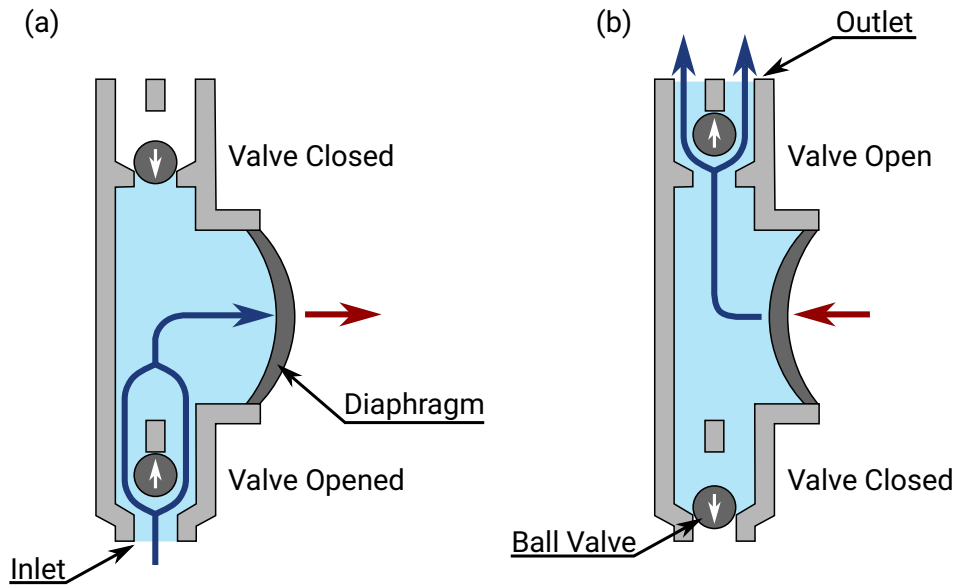


Figure 3.2: Working principle of a diaphragm pump. (a) The diaphragm is pulled outwards to increase the volume in the suction chamber and to create an negative pressure. Gas flows into the suction chamber due to the pressure differences. The outlet is closed through a ball valve preventing gas from the outside to enter the system. (b) After the chamber is filled with gas, the diaphragm gets pushed in. The increasing pressure closes the inlet while simultaneously opening the outlet. The gas gets pumped to the outside and the cycle repeats. As the valves are operated by the difference in gas pressure, pumps of this type are limited to pressures > 0.1 mbar.

provide a vacuum in RV or lower FV regime, which is a requirement for the operation of second-stage pumps. As an example of a positive displacement pump, the working principle of a diaphragm pump is shown in Figure 3.2.

For lower pressures, the turbo-molecular pump (often simply referred to as turbo pump) is the most commonly used. It transports the gas by transferring momentum to the gas molecules through a fast-moving wall or blades of a turning rotor. The momentum accelerates the gas into a desired direction. However, as molecular pumps are not capable of compressing and ejecting the gas against atmospheric pressure, a backing pump is required, which can remove the compressed gas from the system. Therefore, a positive displacement pump is usually directly connected to the turbo pump and serves as both, to

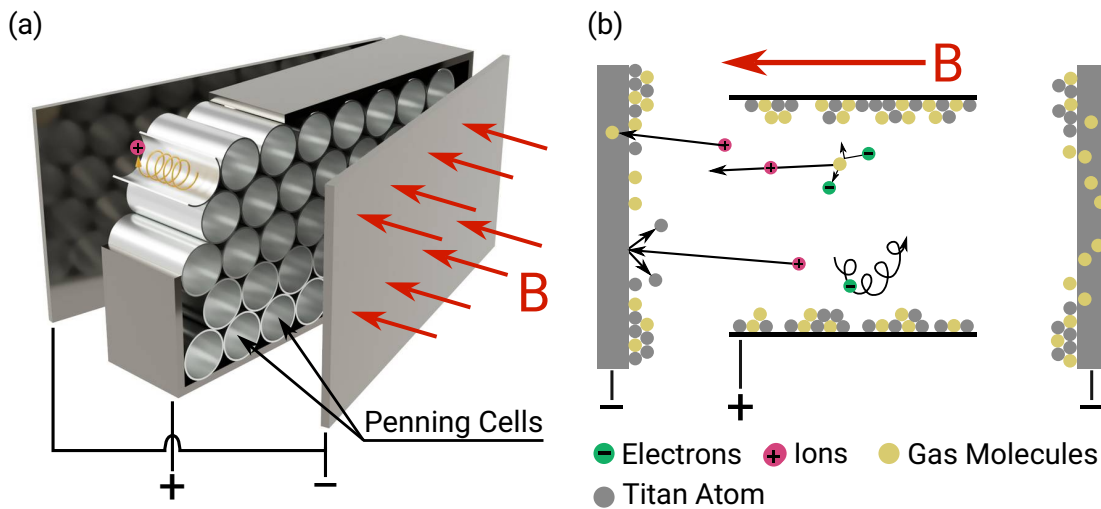


Figure 3.3: Setup and working principle of an ion getter pump. In (a) the construction is shown with cylindrical stainless steel anodes (Penning cells) packed perpendicular between two parallel cathode plates. A potential difference of a few kV is applied to both. Permanent magnets on the outside of the pump (not shown) create a permanent magnetic field. The working principle is illustrated in (b) for one Penning cell. Electrons are forced onto a spiral path towards the anode, ionizing more gas molecules on its way. The ions are accelerated towards the cathode, where they get buried deep into the bulk material. A rain of bulk material, sputtered by ion impact, binds and captures reactive gases at the anode surface. Graphic based on [122, Fig. 2.61 and 2.62].

create a RV/FV pre-pressure before activation of the turbo pump and as the backing pump. Both, positive displacement and turbo pumps require a viscous flow, but below HV the behavior of the molecules is determined by molecular flow. As a result the pumping speed of these pumps drops drastically. To achieve UHV or XHV, an additional pump based on the principle of gas trapping is mandatory.

Capture pumps utilize chemical or physical bondings to adsorb molecules and trap them in the bulk of the pumping material. Two commonly used representatives of these pumps are the ion getter pump (IGP, also known as sputter ion pump) and the non-evaporable getter (NEG). Both are used in this work and will be described here briefly. An illustration of the first type can be seen in Figure 3.3. Cylindrical stainless-steel anodes (Penning cells) are packed perpendicular between two parallel cathode plates. The potential difference

applied to both are of a few kV. The whole setup is placed in an homogeneous magnetic field, created by a permanent magnet on the outside of the housing. Electrons, created by the high voltage (h.v.¹) gas discharge, will be forced onto a spiral path towards the anode, ionizing more gas molecules on their way. The ions are accelerated towards the cathode, where they get buried deep into the bulk material and also sputter the cathode material at impact. This sputtered material operates as a getter film, which binds and captures reactive gases like oxygen, nitrogen and hydrogen at the anode surface. For hydrogen, however, the major pumping mechanism is the diffusion into the cathode material. Its pumping speed is typically two times higher than for nitrogen, but it is not capable of producing a sufficient sputtering yield on its own. The general pumping speed of IGPs depends on the pumped gas as well as the cathode material used (usually titanium). For the capture capabilities of different materials and more details on sputter ions pumps, see [122] or [127]. Due to glow-discharge at the Penning cells at high pressure, which would prevent the sputtering process, IGP requires a vacuum lower than 10^{-4} mbar. After a certain time of operation (usually multiple years), the cathode panels need to be replaced due to the damage created by the impinging ions.

The second capture pump used in this work is the non-evaporable getter (NEG). It utilizes chemical bonding with highly reactive alloys to adsorb gas. Molecules impinging on the sorbent material are dissociated and trapped in the form of stable chemical compound. Depending on gas and temperature, bound molecules quickly move from the surface deeper into the bulk material to make space for new gas particles [127]. Under atmospheric air, a thin protective passivating layer of oxides and nitrides is formed at the surface, which allows the NEG to be handled in air. In vacuum, the pump needs to be activated by bake-out, to first release the physically trapped gases and then to remove the passivating layer. The latter dissolves due to diffusion deeper into the bulk material, which returns the surface to its metal state, and thus, restores the ability to capture gases [128, 129]. The required time and temperature for activation depends on the used alloy and the time the pump was exposed to air. Commonly used alloy elements are titanium, zirconium, hafnium, tantalum and niobium. More information on used alloys and NEG pumps in general can be found in [127]. For hydrogen, NEGs provide a high pumping speed, but they cannot trap noble gases and CH_4 . Therefore, they are often combined with IGP to reach pressures in the XHV regime. The fact that they only require electrical power for the activation process makes NEGs highly flexible so that they can be build in almost any form. Even an entire vacuum chamber can be transformed into a large pump,

¹In most literature the acronym HV is used for high voltage, but to distinguish it from the acronym for high vacuum h.v. is used in this dissertation.

by coating the chamber walls with NEG material. They are also handy for setups without a permanent electrical connection like a transport chamber (see Section 4.6).

There are much more representatives of these pump types, but as they are not used in this work, they will not be discussed here. The interested reader is referred to [122] or [127] for more information.

3.4 Cryopumps

As a cryopump is the key element for the electron gun in this experimental setup, it will be covered in more detail than the other types. It follows in line with the report of Day [130].

Cryopumps are another prominent example for capture pumps. They use a surface, cooled down to cryogenic temperatures to capture gas particles. By international definition, the surface needs to be below 120 K to be classified as a cryopump². Like NEG^s, they need to be regenerated by heating to release the captured gas. Also, as for any high vacuum pump, an appropriate pre-pressure needs to be provided due to a limited capture capacity. In contrast to NEG^s, there is no chemical bond of the gas with the pump surface (with the exception of cryogetter pumps, see Section 3.4.1), but the involved forces are relatively weak as they are primarily van der Waals forces.

The pumping speed of cryopumps for a specific gas with temperature T and molar mass M can be calculated by [131]

$$S_{cryo} = c_s \cdot S_{id} = c_s \cdot A_c \cdot \sqrt{\frac{R \cdot T}{2\pi \cdot M}}, \quad (3.11)$$

with the area A_c of the cryosurface. The quantity S_{id} refers to the theoretical black-hole pumping speed, which in reality is reduced, firstly due to a limited transmission probability w to the cryopanel, and secondly because not all incident particles stick to the pump. The ratio of particles sticking to the surface and the number of particles impinging on it is called the sticking probability α_s . Both factors can be combined to the capture coefficient c_s by the reciprocal addition equation [131]

$$\frac{1}{c_s} = \frac{1}{\alpha_s} + \frac{1}{w}. \quad (3.12)$$

This equation holds only for a simple parallel arrangement of the cryopanel and a heat shield, as in most commercial pumps. However, one advantage of cryopumps is that they

²according to ISO 3529/1-3

can be custom tailored to the available space or a specific application. For a more complex setup, the capture coefficient can only be calculated using Monte-Carlo simulations of the pump's interior.

3.4.1 Pumping Mechanisms

Cryopumps can be categorized into four different types depending on the trapping mechanism used, described in the following sections.

Cryocondensation

Cryocondensation is the interaction between the gas and the particles of the same gas on a cryosurface. In theory, every gas could be pumped if the provided temperature is low enough. With 20 K, a pressure below 10^{-11} mbar can be achieved for all gases, except neon, helium (He) and hydrogen [132]. As the achievable pressure for cryocondensation is directly linked to the saturation pressure of the given gas at the provided surface temperature, a much lower temperature is needed for these three gases. Figure 3.4 shows the saturation pressure curve for the most relevant gases. For practical use an even lower temperature is needed, as the saturation curve shows the thermal equilibrium, which translates to a pumping speed of zero. For example a hydrogen pressure of 10^{-9} mbar requires a temperature of about 3.4 K [132]. Helium cannot be captured with condensation at all. Using cryocondensation, a selective pump can be build, pumping only the gases that get captured at the chosen temperature.

Cryosorption

If one wants to pump all gases, especially helium and hydrogen, cryocondensation requires temperatures too low to be practical in photo-gun applications. But the cryosorption effect allows these gases to be pumped at higher temperatures than the saturation pressure. The forces involved are also van der Waals forces but not between the gas particles among each other but between the gas and a chosen sorbent material, which is applied to the cryosurface. These forces are much stronger and allows the particles to be bound at higher temperatures. For helium temperatures < 4.2 K [133] and for hydrogen < 20 K [132] are sufficient.

The choice of sorbent material is of great importance for the performance of cryosorption pumps and is subject to recent studies [131]. In contrast to cryocondensation, the pumping process is determined not only by the temperature but rather by the chosen cryosorbent and its properties (chemical, mechanical, physical). Due to the interaction between the

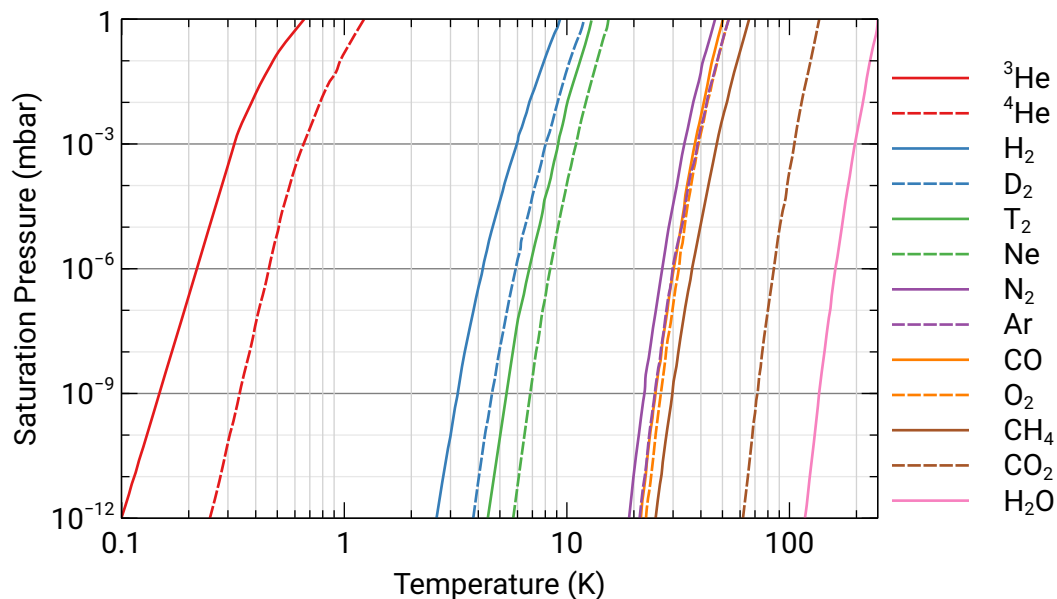


Figure 3.4: Temperature dependent saturation pressure for some common gases. Source of data: [130].

sorbent material and the gas molecules, the cryosorption pumping effect is limited to a few monolayers of absorbed gas on the cold surface, after which the pumping effect reduces drastically. To have a comparable and reproducible measure, the pumping is defined as the amount of gas that has been captured until the pumping speed drops down to 50% of its initial value [130]. The most popular types of sorbent materials are presented in Section 3.4.2. Most commercial available cryopumps use a combination of cryocondensation for heavy gases and cryosorption for light gases.

Cryotrapping

Another method to capture gases with weak cryosorption forces like helium, hydrogen and neon in under-saturated conditions was discovered in 1960 by Chuan[134]. The condensation temperature of a gas can be increased by adding a condensable gas and creating a gas mixture. If the gas with the weaker cryosorption force is not too dominant in the mixture, it gets incorporated into the condensate of the other gas with a higher cryosorption force, leading to a reduced vapor pressure. Efficient cryotrapping gases for hydrogen are Ar, CO₂ and NH₃ [135].

Cryogettering

Cryogettering is not a cryopumping effect per se, it rather improves the already existing chemisorption pumping effect of metal films by cooling the sorbent material, leading to an increased reactivity of the metal. This effect was discovered in 1962 in three different laboratories simultaneously, as they used a cooled LN₂ substrate for the film of a titanium sublimation pump [134]. Other materials like Mo, TiO, Nb, Ni and Ta were also investigated, but the most prominent representative of cryogetter pumps is the titanium sublimation pump. They are capable of pumping hydrogen at temperatures below 77 K, which makes them an attractive option for electron sources. The disadvantage of sublimation pumps are the need to renew the metal film after certain times during operation to maintain a pumping effect.

3.4.2 Sorption Materials

Since the efficiency of a cryosorption pump highly depends on the properties and selection of the sorption material, choosing the right material is critical when designing a cryopump. Due to the fact that the pumping effect vanishes with increasing layers of condensed gas, a material with high internal surface is needed to achieve a high pumping capacity. Extensive comparison and testing of different kind of materials were conducted at the Forschungszentrum Karlsruhe in Germany by Perinić in the 90s [136, 137] and later by Day [131], at Los Alamos in the USA by Sedgley et al. [138–141] and by Stern [132]. Xu and Matsui demonstrated the use of copper powder [142] and Ma et al. benchmarked MgO [143]. These studies indicate active charcoal, zeolite molecular sieves and condensed gas as the most suitable candidates. Therefore, they are the most commonly used materials in cryopumps today and will be discussed briefly in the following.

Condensed Gases

A porous surface can be created by infusing a gas, which condenses on the cold surface. Suitable gases are for example argon or SF₆ to capture helium or CO₂ to capture hydrogen [130]. There are two techniques to create a condensed-gas layer. The first is the pre-frost technique, where the gas is injected prior to the actual pumping. With this technique, a limited pumping capacity is created in the same way as when using coal or molecular sieves but with a lower achievable equilibrium pressure.

The second way to use condensed gases is to continuously inject the gas during operation. This gives the advantage of continuous renewal of the capture surface, giving a much higher total capture capacity compared to the pre-frost variant and providing a steady

pumping speed. Another advantage is a higher ratio of captured gas molecules to the sorbent gas molecules.

Nevertheless, both approaches have the disadvantage of a higher amount of gas load during regeneration, requiring more pumping power of the fore pumps. Because of the more complex setup and the need to introduce an additional gas into the chamber, gas sorbents are only used in exceptional situation today. All commercially available pumps use solid cryo sorbents.

Zeolite Molecular Sieves

Synthetic molecular sieves out of zeolite microporous aluminosilicate minerals can be manufactured with high reproducibility. Hence, their properties are very predictable and can be fine-tuned. Good results in pumping speed and capture capacity for hydrogen at 20 K [132, 144] and helium at 4.2 K [133] with molecular sieves have been reported. However, the regeneration process requires a high temperature of around 300 °C. This is the biggest disadvantage of molecular sieves, especially for this work, as the used aluminum chamber and the used cryocooler cannot withstand temperatures this high (see Section 4.5). Therefore, almost all commercial cryopumps use activated charcoal as sorbent material.

Activated Charcoal

Activated charcoal is a form of carbon, which possesses a large surface area due to a high degree of microporosity, consisting of small, low-volume pores. It can be manufactured from a wide variety of raw materials, such as wood, lignite, pitch, bitumen or coconut shell. The process of creating the microporosity in these materials is called activation. This can be done in two ways: through heating to 800 °C in an oxygen-free atmosphere followed by an activation with steam, CO₂ or air at 700 to 1000 °C, called physical or gas activation. Chemical activation is done by adding chemicals like phosphoric acid or zinc chloride to the raw material before carbonization. The properties and suitability of the different types of activated charcoal depends on the raw material, the activation and carbonization process, including used temperatures, and the ratio of different pore sizes present in the charcoal. The above mentioned benchmarks of different materials demonstrate that activated charcoal inhibits superior pumping capabilities compared to other tested materials. In addition, the required regeneration temperature of charcoal of about 130 °C [131] is significantly lower compared to molecular sieve. This is why almost all commercially available cryopumps are based on activated charcoal. Different types of charcoals have been tested by Day et al. at the Forschungszentrum Karlsruhe in Germany

[131]. They also developed a special spray technique to apply the charcoal coating to the cryopanel [145] which is used for the cryopumps at the International Thermonuclear Experimental Reactor (ITER) [146].

3.4.3 Pump Regeneration

Like other capture pumps, cryopumps exhibit a limited pumping capacity and need to be regenerated after a specific operation time to ensure high pumping speed. The time before regeneration becomes necessary depends on the pump itself and the operational parameters like gas load, pressure and type of pumped gases. Cryocondensation pump capacity is only limited by the temperature rise with increasing condensate layer and therefore, very high. The smaller capacity of cryosorption pumps is limited by full coverage of the cryo sorbent.

For regeneration, the cooling has to be turned off, the capture panel heated up and the released gas pumped down by a fore pump. Afterwards, the pump can be turned on again. The needed regeneration temperature depends on the captured type of gas. Condensed gas will be released immediately by sublimation, when the necessary temperature is reached, while the release of adsorbed gases can take up to some minutes depending on the pore properties of the cryo sorbent. Figure 3.5 shows a typical desorption curve for activated charcoal.

One has to take into account that, while the temperature is rising and condensed gases are released, the temperature of the sorbent material might still be low enough to directly reabsorb the previously condensed gases. Hence, the release characteristics for these gases also follow the one for desorption as shown in Figure 3.6 for CO₂.

3.4.4 Heat Influx

As low temperatures are essential for cryopumps, and they are usually in an ambient temperature vacuum chamber, one has to assess the heat transfer from the warmer outside to the refrigerated cryopanel. The total heat flux³ \dot{q}_{tot} consists of the heat from thermal conductivity of solid components \dot{q}_S , the heat transported by the residual gas \dot{q}_G , thermal radiation \dot{q}_R and for a working pump, the thermal loads due to cryosorption and/or cryocondensation, summarized as \dot{q}_P

$$\dot{q}_{tot} = \dot{q}_S + \dot{q}_G + \dot{q}_R + \dot{q}_P. \quad (3.13)$$

³In most literature, an uppercase \dot{Q} is used, but for a better separation from the gas throughput Q , a lowercase \dot{q} is used in this dissertation.

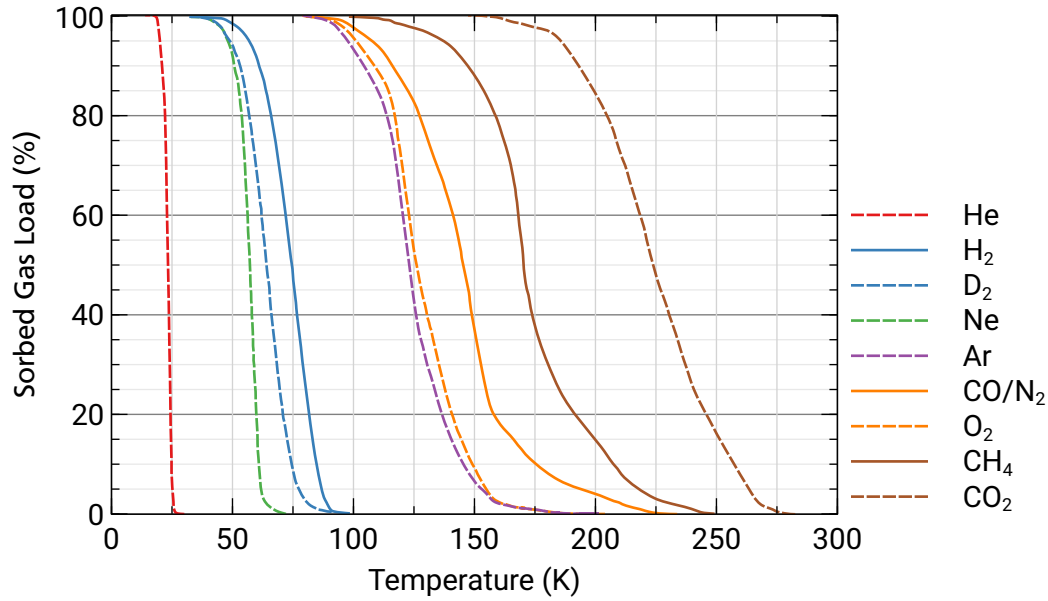


Figure 3.5: Desorption curves of activated charcoal for some gases. Source of data: [130].

For optimal pumping performance, q_{tot} has to be minimized by reducing its components.

The heat transfer of gas molecules \dot{q}_G is created by the energy transfer of collisions between the molecules and any surface. It depends on the mean free path and the number of molecules, in other words the pressure. Under molecular-flow conditions, the influence of gas heat conduction can be neglected [130] and will not be discussed here any further.

The heat transferred by a solid connected to the pump (e.g. via cable, fastenings, supply lines) \dot{q}_S is given by Fourier's law [147]

$$\dot{q}_S = k(T)A_s \frac{dT}{dx}, \quad (3.14)$$

with the cross section A_s of the solid and the temperature-dependent thermal conductivity $k(T)$. For a solid rod of length L with a temperature range from T_1 to T_2 , the equation can be rewritten in an integral form

$$\dot{q}_S = \frac{A_s}{L} \cdot \int_{T_1}^{T_2} k(T) dT. \quad (3.15)$$

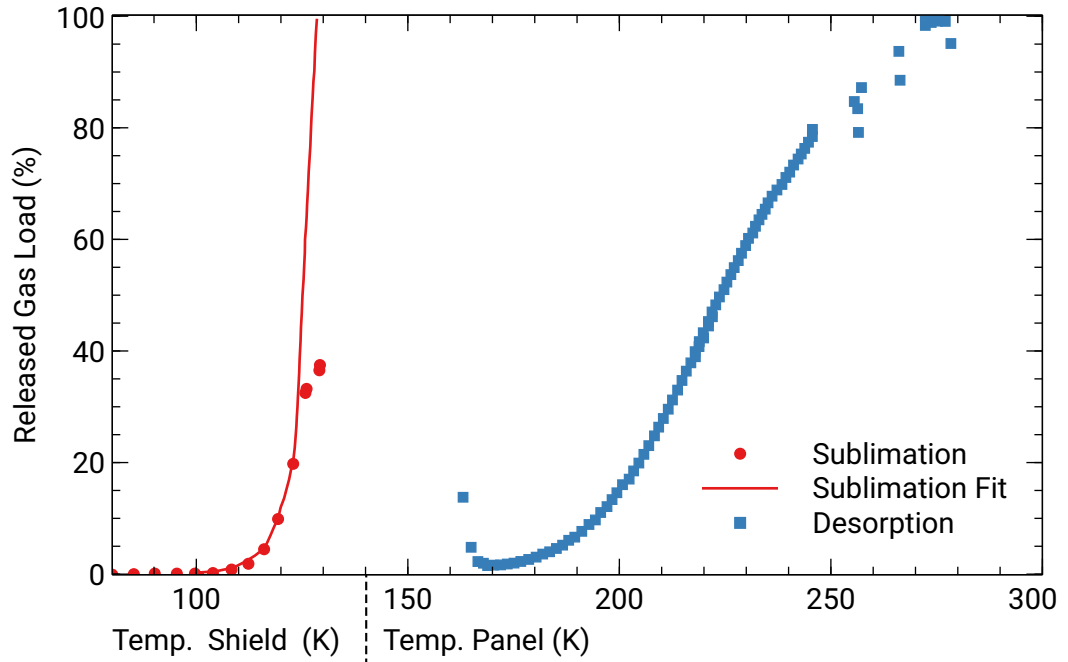


Figure 3.6: Regeneration process of CO_2 . The gas, condensed on the shield, gets released with rising temperature (sublimation) and directly reabsorbed by the cryopanel, which still possesses a pumping effect at that temperature. With further increasing temperature, the gas gets desorbed from the panel and regeneration is completed. Source of Data: [130].

The thermal conductivity integrals $\int_{T_1}^{T_2} k(T) dT$ of common materials are tabulated in literature. As thermal conductivity shows great differences between materials, its selection is of great importance to minimize heat load.

Another significant heat load will be caused by radiation between the vacuum chamber at room temperature and the cold cryopanel of the pump. The heat flux via radiation between two bodies with temperature T_1 and T_2 can be calculated by [130]

$$\dot{Q}_R = C_{12} \cdot A_1 \cdot (T_1^4 - T_2^4), \quad (3.16)$$

with the surface area A_1 of the warmer body, the emissivities ϵ_1 and ϵ_2 of both bodies and

the exchange number C_{12} . The latter is given by

$$C_{12} = \frac{\sigma \cdot \epsilon_1 \epsilon_2}{1 - (1 - \epsilon_1) \cdot (1 - \epsilon_2) \varphi_{12}}, \quad (3.17)$$

where σ denotes the Stefan-Boltzmann constant, and φ_{12} describes the view factor of both surfaces, which depends on the geometry and orientation of both bodies. It describes the percentage of radiation leaving surface 1 that is intercepted by surface 2.

As the radiant power increases with the 4th power with the temperature difference, it is the most relevant factor when reducing heat radiation. This is usually done by introducing a heat shield at a temperature typically between 50 K and 80 K. The shield needs a higher cooling power to compensate the introduced heat from the ambient temperature. This additional stage between the cold cryopanel and the warm vacuum chamber reduces the total heat flux significantly and is an essential component for most cryopumps. Another important aspect for thermal radiation is the emissivity ϵ , which depends on the materials involved as well as their surface structure. Polished surfaces usually show a smaller emissivity.

The last contribution to the total heat load is the load due to cryosorption and cryocondensation. It is proportional to the amount of molecules hitting the cryopanel and the per molecule transferred enthalpy ΔH . The heat flux is then given by [148]

$$\dot{q}_P = \frac{A_c \cdot \bar{v} \cdot p}{4 \cdot RT_G} \cdot [\alpha_s \Delta H(T_G \rightarrow T_C) + (1 - \alpha_s) \Delta H(T_G \rightarrow T_R) - \alpha(p_e/p) \Delta H_S], \quad (3.18)$$

with the area of the cryopanel A_c , the average thermal velocity \bar{v} of the incident molecules, the pressure p around the panel, gas temperature T_G and the capture coefficient α_s . The fraction of α_s gets captured, the fraction of $1 - \alpha_s$ reflected and the fraction $\alpha(p_e/p)$ re-evaporated. The terms $\Delta H(T_G \rightarrow T_C)$, $\Delta H(T_G \rightarrow T_R)$ and ΔH_S describe the corresponding amount of transferred enthalpy per mol. For high thermal accommodation, the temperature T_R of the reflected molecules can be assumed to be near the temperature T_C of the cryopanel [148].

3.4.5 Commercial Refrigerator-Cooled Cryopumps

In this section, one specific category of commercially available cryopumps will be presented briefly as it is the inspiration for the cryosource designed in this work. The cooling power for this types of pumps is provided by a closed-cycle refrigerator (cryocooler), which exploits the Gifford and McMahon process [149]. The working gas helium is circulated between a compressor and the refrigerator, where the gas gets expanded in two stages.

The first stage, which usually has an operation temperature between 50 K and 80 K, is used to cool a radiation shield and a baffle across the inlet of the pump. The shield is required to reduce heat radiation from the room-temperature vacuum chamber and thereby ensures a temperature of around 10 K and below at the second stage. Here the cryopanel is mounted and is usually coated with a sorbent material on the inside. An illustration of this pump type is shown in Figure 3.7.

Heavy gases are captured directly at the warmer baffle by cryocondensation, while nitrogen gets pumped at the uncoated outside of the cryopanel also by cryocondensation. The light gases like helium and hydrogen, which cannot be captured by condensation, will make their way to the inside of the panels where they get pumped by cryosorption.

Due to the limited cooling power provided by the cryocooler, these pumps are rather small. However, the closed loop cycle makes them easier to handle than other cryopumps like bath pumps, which require a constant supply of new liquid helium. For more information on bath- and additional cryopump types, see [127], [130] and [148].

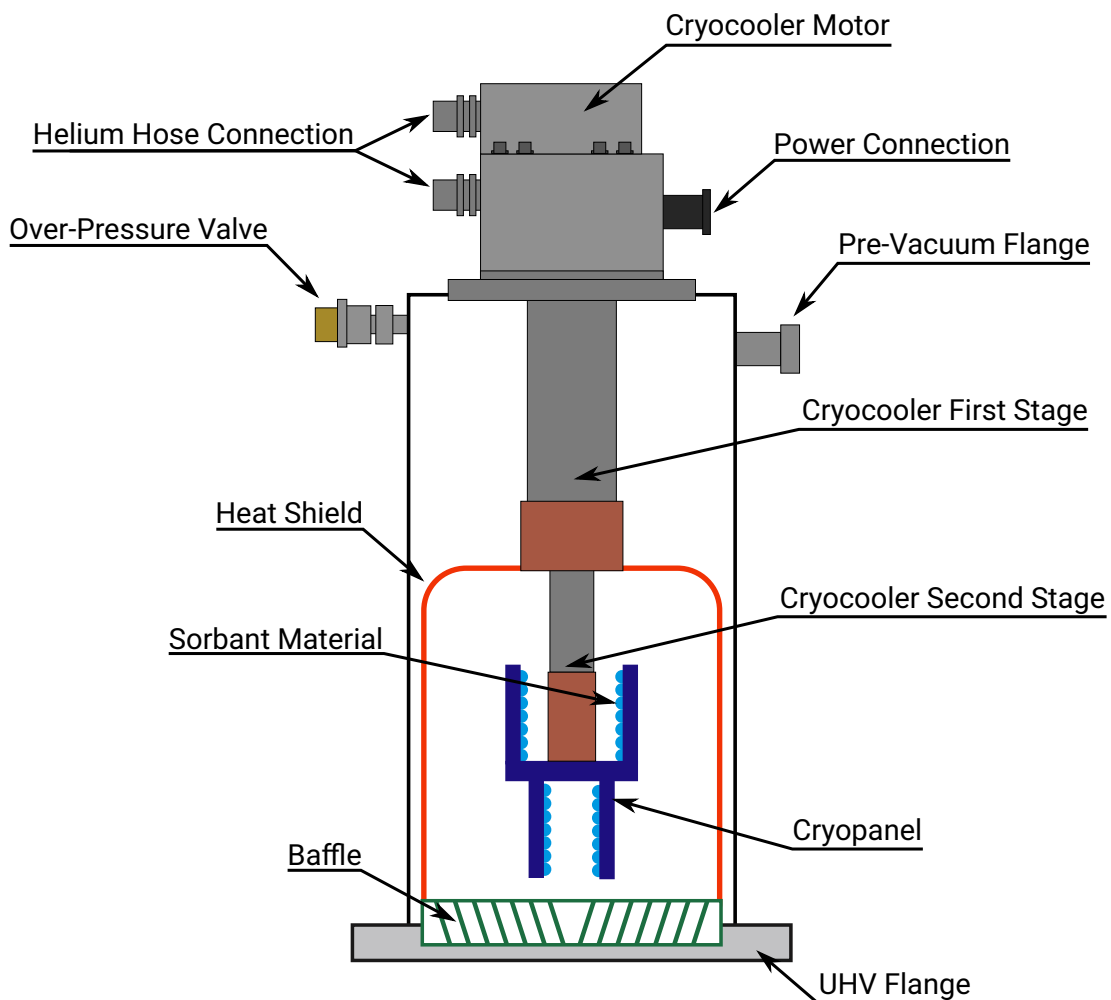


Figure 3.7: Schematic illustration of a refrigerator-cooled cryopump with integrated cryocooler. Heavy gases are captured directly at the baffle while nitrogen gets trapped by the uncoated outside of the cryopanel, both by cryocondensation. The lighter gases like helium and hydrogen cannot be captured by condensation. They are pumped by cryosorption with the sorbent material on the inside of the cryopanel. Illustration based on [127, Fig. 12.22].

4 Design of a Cryogenic Electron-Gun

4.1 Idea and Motivation

The purpose of this work is the design and construction of a source for highly polarized electrons with an improved photocathode lifetime especially for future high current (20-100 mA) applications. As can be seen in Table 2.3, a laser power in the regime of some Watts is required for such high currents. This will lead to a short cathode lifetime due to thermal desorption as described in Section 2.3.4. Hence, active cooling of the cathode is essential to counter the heat influx introduced by the laser. This however is not sufficient to ensure a lifetime long enough for high current experiments, as IBB is still present and increases proportional to the number of electrons and therefore, the extracted current. With sufficient cooling of the cathode to prevent thermal desorption IBB will be the dominant effect contributing to the decay of the NEA layer. Improvement in the vacuum conditions would be most effective in reducing IBB. As a cooling system is required in any case, a cryopump which makes use of the same system could be a viable option to reduce the pressure. The advantage of cryopumps are the very high pumping speed they provide and the fact that they can be custom tailored to fit any geometry. However, when placing the cryopanel of a commercial pump inside the source volume, the gas molecules originating from the chamber walls still need to find their way to the panel. When passing the electron beam the molecules can still be ionized. So in this work a different approach was chosen.

By taking advantage of a custom tailored pump, the cathode will be placed in an almost completely closed cryogenic sub-volume, effectively turning the whole sub-volume into a vacuum pump. This way when the cryopump is activated there will be no more outgassing in the sub-volume due to the cryogenic temperatures, while the existing residual-gas molecules will be pumped by the walls. The design is inspired by the commercially available refrigerator cooled cryopump described in Section 3.4.5. The cryopanel and baffle will be replaced by the sub-volume. As the electron beam needs to leave the volume it cannot be closed completely. In order to get sufficiently low pressure inside of the volume prior to activating the cryopump, an adequate gas flux due to a non-zero vacuum conductance is required (see Section 4.3.1). As this opening will be the only way new gas

molecules get introduced into the sub-volume a significantly improved vacuum condition inside the volume and around the cathode is expected. This would greatly reduce IBB as well as residual-gas adsorption thereby significantly improving both vacuum and charge lifetimes. Lee et al. showed that additionally an increase in beam quality parameters such as a smaller emittance (see Section 4.3.3) can be expected from a cooled cathode [150], which, however, is not the focus of this work and will not be investigated any further.

Photo-CATCH features a set of vacuum chamber for cleaning and activation of GaAs cathodes and therefore, provides a suitable base for the new cryogenic source. However, at the time of the setup a direct integration into Photo-CATCH was not possible due to the fact that the test stand was in active use for other experiments and longer reconstruction work of the chambers as well as the beamline would be required. Therefore, a separated independent smaller test stand with minimal diagnostics and no activation capabilities was developed. A transport chamber designed by Kurichiyani [43] was used to transfer cathodes, activated at Photo-CATCH, to the new test stand. The design of all components of the setup has been carefully chosen such that it allows future integration into Photo-CATCH. In the following chapters all parts of the cryogenic source, the new test stand and Photo-CATCH will be presented in more detail, starting with the latter.

4.2 Photo-CATCH and Cathode Preparation System

The test stand Photo-CATCH provides a set of vacuum chambers for photocathode cleaning and activation, as well as a -60 kV DC photo-gun and a beamline with diagnostic instruments. In this section the setup will be described along the lines of [42], [43] and [49] starting with an overview, followed by a more detailed description of the activation chamber, which was used to provide the cryo source with activated cathodes.

4.2.1 Photo-CATCH Overview

Photo-CATCH features four chambers, which are connected in a row and can be separated by all-metal valves. The transport of the cathodes between the chambers is done via magnetically-coupled linear transfer devices, here referred to as *manipulators*. A steel fork is connected to the manipulators, fitting into a molybdenum holder called puck, which houses the photocathode¹. Figure 4.1 shows a model of a transport fork and a puck with installed photocathode. An overview of the whole test stand is given in Figure 4.2. New

¹Molybdenum exhibits an expansion coefficient lower than stainless steel by the factor of 3 to 4. This way the puck will not get stuck in the fork or other holders during bake-out or heat cleaning.

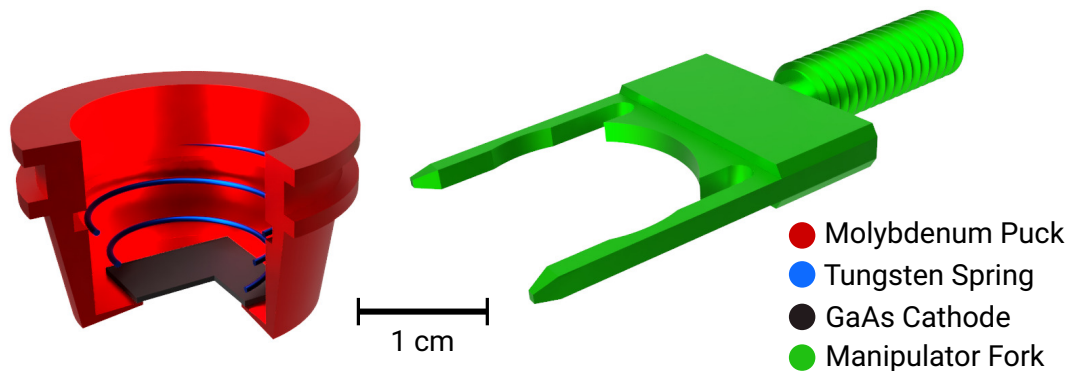


Figure 4.1: Cut view of the puck and the transport fork. The puck houses the cathode which is held in place by a tungsten spring. A hole in the bottom exposes the cathode to the laser beam. The fork is inserted into the gap around the pucks top for transfer.

cathodes are introduced to the system through the load-lock chamber (LLC) which is equipped with a 260 l/s turbo pump and reaches a pressure in the high 10^{-9} mbar regime, which is monitored by a combined Pirani and cold-cathode vacuum gauge. The chamber can be quickly vented, opened and closed again using a quick-CF-flange system (QCF). To prevent unnecessary contamination, venting is done using nitrogen. Newly inserted pucks are directly placed onto the fork of a manipulator used for transfer into the next chamber. For a first cleaning of new pucks and cathodes, a tungsten coil located inside the load-lock chamber can be used. It is a common procedure to first anneal the empty puck at a temperature of up to $500\text{ }^{\circ}\text{C}$ for 1 h to 2 h to remove contaminations prior to cathode installation.

The next chamber is the atomic hydrogen cleaning chamber (AHCC), which is dedicated to the cleaning of photocathodes. For this purpose it is equipped with a hydrogen atom beam source and two heating coils. To store the puck coming from the LLC a carousel that can be moved both vertically as well as radially is mounted at the top flange. It can hold up to two pucks at the same time. This chamber is pumped by a 100 l/s IGP and a 400 l/s NEG to a base-pressure in the low 10^{-11} mbar regime. The pressure can be measured by a cold-cathode ionization gauge and the IGP controller. After cleaning, the puck can be picked up from the carousel by a manipulator and can be transferred to the cathode activation chamber (CAC). There the activation procedure as described in Section 2.3.3 is conducted. It has been used in this work to prepare cathodes for the cryo source test stand and will be described in more detail in the next section.

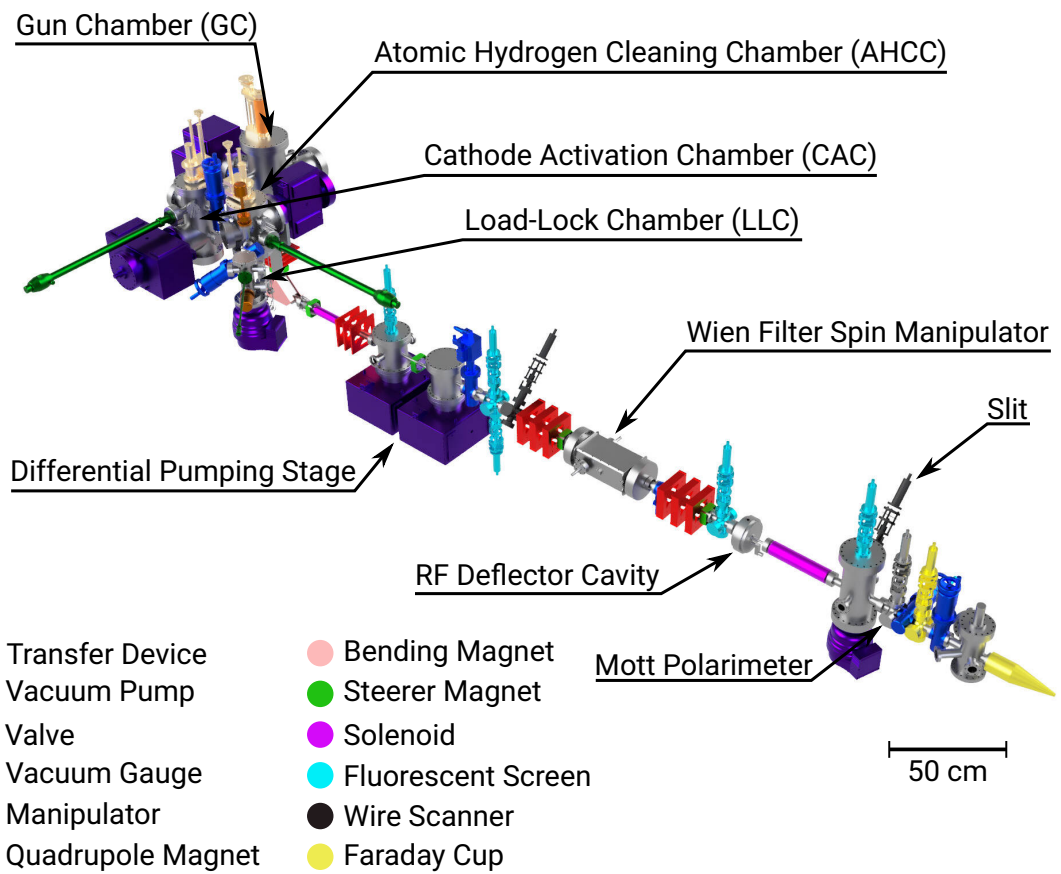


Figure 4.2: Overview of the Photo-CATCH test stand. Shown are the four chambers and the beam line. New photocathodes get introduced into the system using the Load-Lock Chamber (LLC) and transferred between the chambers by manipulators. The cleaning and activation procedure takes place in the Atomic Hydrogen Cleaning Chamber (AHCC) and the Cathode Activation Chamber (CAC). The DC electron gun inside the Gun Chamber (GC) produces the electron beam, which gets deflected by 90° by a bending magnet and directed into the main horizontal beamline. There different diagnostic instruments are located to measure the properties of the electron beam. For better visibility the support frame and the Helmholtz coils, which compensate for the earth's magnetic field, are not shown in the picture.

The last chamber before the beamline is the gun chamber (GC). It holds a DC photo-gun featuring a so-called inverted insulator geometry. A voltage of up to -60 kV can be applied to the electrode. The chamber is pumped by a combined 400 l/s IGP and 400 l/s NEG and an additional 2000 l/s NEG. The pressure is monitored by a hot-cathode ionization vacuum gauge. This gun was not used in this work. For more details on the chamber and the inverted geometry one may consult [42] and [43].

After a short vertical beamline, the electron beam from the gun and from a future cryo source gets deflected by 90° by a bending magnet into the main horizontal beamline. It is equipped with instruments for measurements of electron-beam parameters as well as low-energy experiments. The pressure at UHV level in the gun chamber and the vertical beamline is separated from the higher pressure in the main beamline (in the regime of 10⁻⁸ mbar) by two differential pumping stages. Multiple magnets such as quadrupole triplets, steerers and solenoids are used to focus, shift and control the electron beam. To compensate the influence of the earth's magnetic field, two Helmholtz coils are placed along the horizontal beamline. For monitoring of the beam position, retractable beryllium oxide (BeO) fluorescent screens are available. Two Faraday cups are located at the end of the beamline for beam-current measurements and a combination of a 3 GHz RF deflector cavity and a slit can be used to measure the longitudinal shape of the electron bunches. For emittance measurements two wire scanners are present at two positions along the beamline. The electron spin-polarization can be measured by a Mott polarimeter and the spin orientation can be manipulated using a Wien filter. Most of the components are controlled by in-house electronics based on the Controller Area Network (CAN) bus using the *Experimental Physics and Industrial Control System* (EPICS) [151], that is also used for controlling the S-DALINAC [152]. A detailed description of all Photo-CATCH diagnostic instruments can be found in [42].

4.2.2 Cathode Preparation System

The activation system of Photo-CATCH was used in this work to prepare activated GaAs-cathodes for the cryo source test stand. The complete system is shown as a schematic representation in Figure 4.3 and a 3D-model in Figure 4.4. Like the AHCC, it features a carousel mounted to the top flange to store and transport pucks. After bake-out a pressure in the lower 10⁻¹¹ mbar regime can be maintained by a 200 l/s IGP and a 400 l/s NEG. A cold-cathode ionization gauge connected to a remote-controllable multi-channel gauge controller measures the pressure. For transportation to the gun chamber, a manipulator is present and a large window allows visual observation of the manipulator and the carousel. In the upper part of the chamber, two tungsten coils are mounted and connected trough

an electric feedthrough. They provide an additional option for cleaning of the cathode, when the hydrogen cleaning is not used. The carousel allows positioning of the puck under the coils by rotation and vertical movement. Both are controlled from the outside by a rotary drive and a translator mounted to a bellow on top of the chamber. The position of the puck characterized by the height and the angle are displayed at the translator in mm and the rotary drive in degrees, respectively. During heat-cleaning the temperature of the cathode surface can be monitored by an infrared pyrometer attached to the window at the chamber bottom. For easier alignment of the pyrometer and the laser used for the activation procedure a camera module² is mounted to the bottom window as well.

On the mid-level of the chamber the activation assembly is mounted to an electric feedthrough. It features a ring-anode to measure the photocurrent and two dispensers, one for caesium and one for lithium. A positive bias voltage is applied to the anode through a connected power supply which can provide a voltage of up to 500 V, while the photocurrent received by the anode is measured with a current meter. To control the flux of caesium and lithium independently, the dispensers are driven by separate power supplies. Oxygen is provided through a piezo-electric controlled leak valve from a separated reservoir attached to the chamber. It is operated with a high-voltage module, providing a voltage of up to 1 kV. Through the bottom window incident light is introduced by either an array of white-light LEDs, an array of blue LEDs³ or a 780 nm red laser beam. The latter is provided by a separated laser setup and guided to the CAC through a polarization-maintaining fiber-optic patch cable mounted at the bottom window. A manual shutter directly behind the lens allows to block the beam. To measure the laser power right before entering the chamber a non-polarizing beam splitter and a photodiode are used. A constant fraction of the laser power is diverted to the diode and read out by an in-house-produced current meter. Two coated dielectric mirrors are mounted after the beam splitter, that allow the laser to be aligned onto the cathode. From the photodiode readout, the splitting ratio of the beam splitter $r = P_T/P_R = 1.908(1)$ (where the transmitted power P_T also takes the loss of the mirrors into account) and the transmission coefficient of the window $C_T = 0.90(2)$, the actual power of the laser on the cathode surface can be calculated. The power and current supplies of the ring anode, the dispenser and the piezo valve, as well as the current meter and the gauge controller are all connected to an EPICS input/output-controller (IOC) server. From a client PC connected to the server all values can be read out and controlled for the activation procedure. A Graphical User Interface (GUI) build with *Control System Studio* (CSS) [153] allows easy access to all relevant parameters. For a detailed description of the GUI see [49] and [154].

²Raspberry Pi® Camera Module 2 NoIR

³Currently six white and six blue 5050 LEDs of unknown spectrum are used.

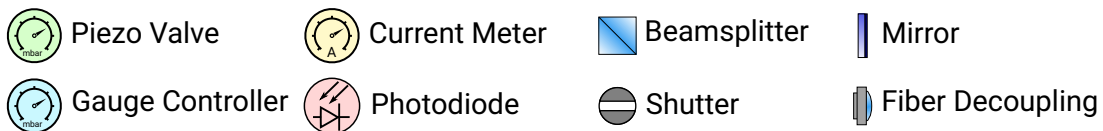
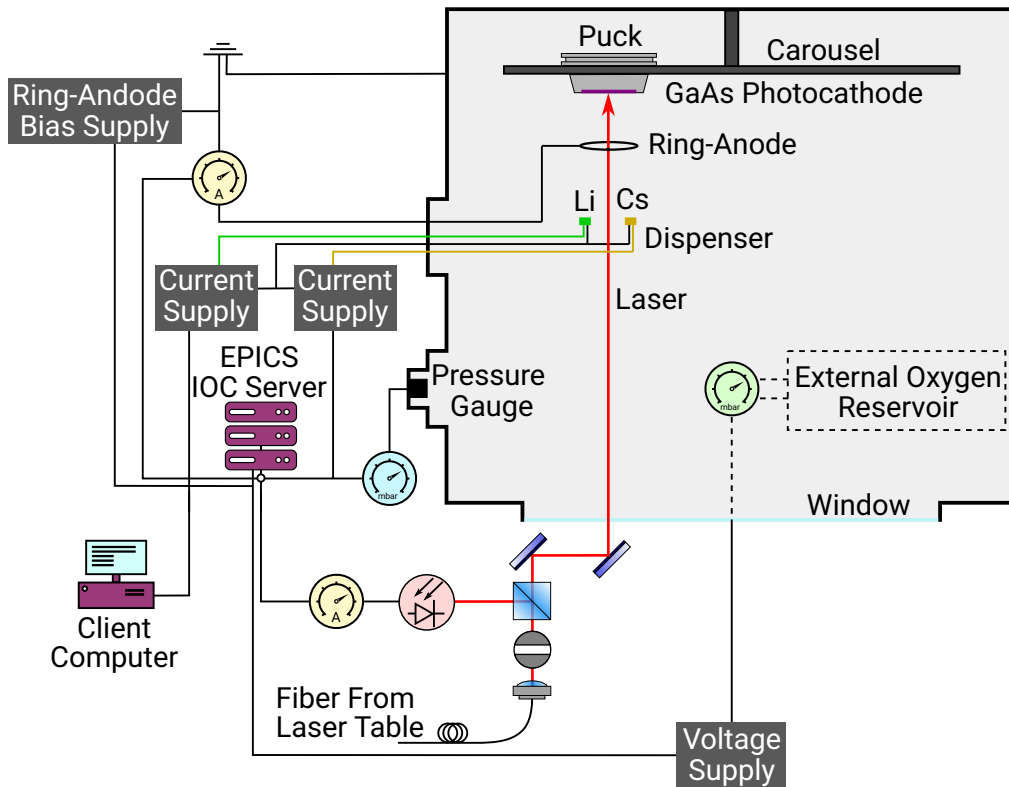


Figure 4.3: Schematic overview of the activation setup at the CAC. The cathode surface is coated with caesium and lithium by running a current through the respective dispenser, while oxygen is introduced through a piezo-electric valve from an external reservoir. A photo diode and a beam splitter cube located at the bottom window allows to monitor the power of the laser right before the beam enters the chamber. As an alternative light source a white-light or blue LED array (not shown in the picture) can be used. The pressure inside the chamber is measured by a cold-cathode ionization gauge and the emitted photocurrent by a ring-anode, which can be biased with a voltage of up to 500 V. An EPICS server allows remote control of all components and data acquisition. Figure based on [49, Fig. 3.3].

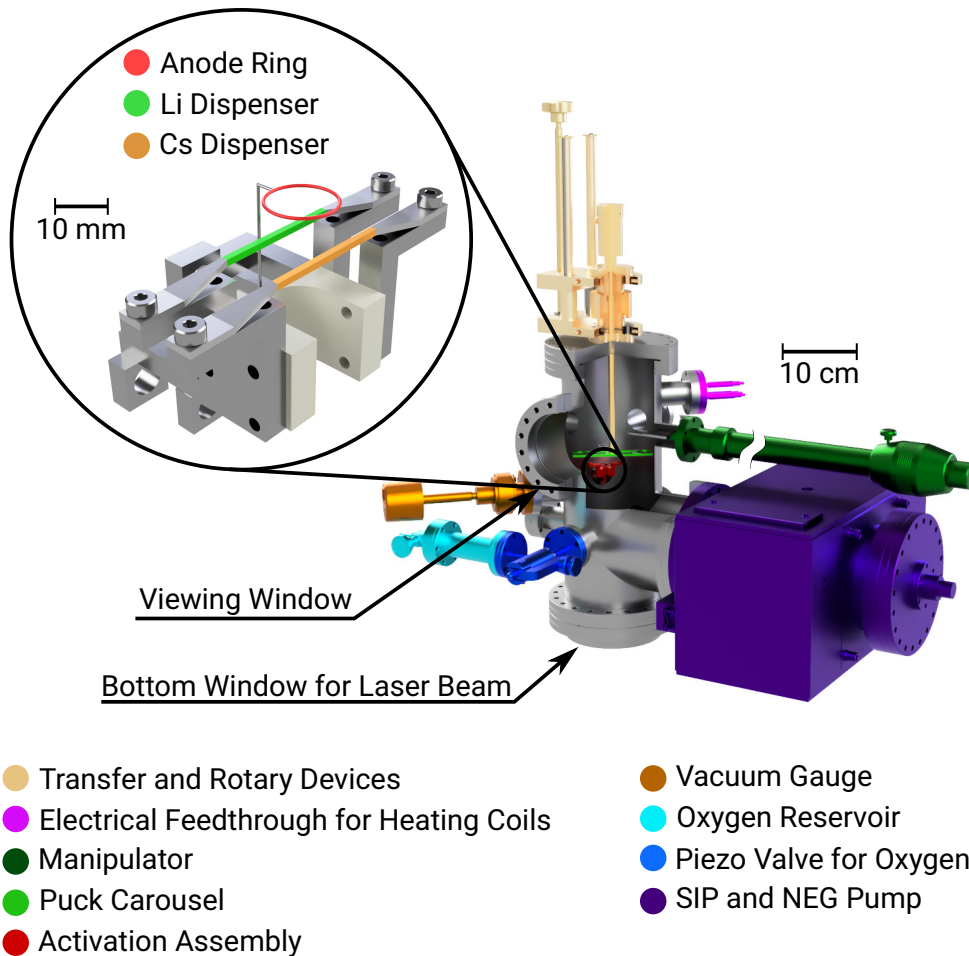


Figure 4.4: Cut-away view of the Cathode Activation Chamber (CAC), with a zoom on the activation assembly. Cathodes held by a puck are transferred into the chamber by the manipulator and placed in the carousel. A z-translator and rotary device allow the carousel to be moved and rotated to place the puck near the two heating coils (not visible in the picture) or over the activation assembly. Caesium and lithium is applied to the cathode using dispensers while oxygen is provided from an external reservoir through an piezo-electric leak valve.

4.3 Cryogenic Sub-Volume

The core component of this source is the cryogenic sub-volume (also referred to as *inner chamber* in this dissertation) in which the cathode will be placed. The design of this volume exhibits some challenges and specific demands on the used materials listed below:

- The volume requires an integrated electrode and anode, which needs to be electrically isolated from each other.
- All materials must be suited for XHV, which includes to be bakeable to a temperature that ensures low outgassing.
- All materials require a high thermal conductivity to achieve the low temperatures necessary for cryosorption.
- A good thermal conductance between the individual parts is essential.
- Thermal radiation and emissivity of all materials needs to be in a regime which allows temperatures low enough for a cryopump.
- The material and the design of the electrode must prevent field emission.
- The design needs to be compatible with the pucks used at Photo-CATCH.
- The size of the source has to be small enough to fit into the available space at Photo-CATCH to make a future integration possible.

The final design of the sub-volume is shown in Figure 4.5 as an exploded view. The top cylinder represents the tip of a closed-cycle cryostat (also referred to as cryocooler), which was chosen to provide the needed cooling power. It will be presented in more detail in Section 4.4. On the copper tip of the cooler a 5 mm thick disc with a diameter of 120 mm made from Oxygen-Free High Thermal Conductivity Copper (OFHC) is screwed to provide a mounting base for the rest of the volume. Between the electrode and the copper disc another 5 mm disc made from aluminum oxide⁴ Al₂O₃ (also called alumina) is located to electrically insulate the cryocooler from the electrode. Aluminum oxide features a high dielectric strength of > 25 kV/m while also showing a high thermal conductivity. Figure 4.6 shows the temperature dependent thermal conductivity for all used and some additional materials, which may be interesting for future experiments with different designs.

⁴A-997 aluminum oxide (99.7% purity) ordered from BCE Special Ceramics GmbH

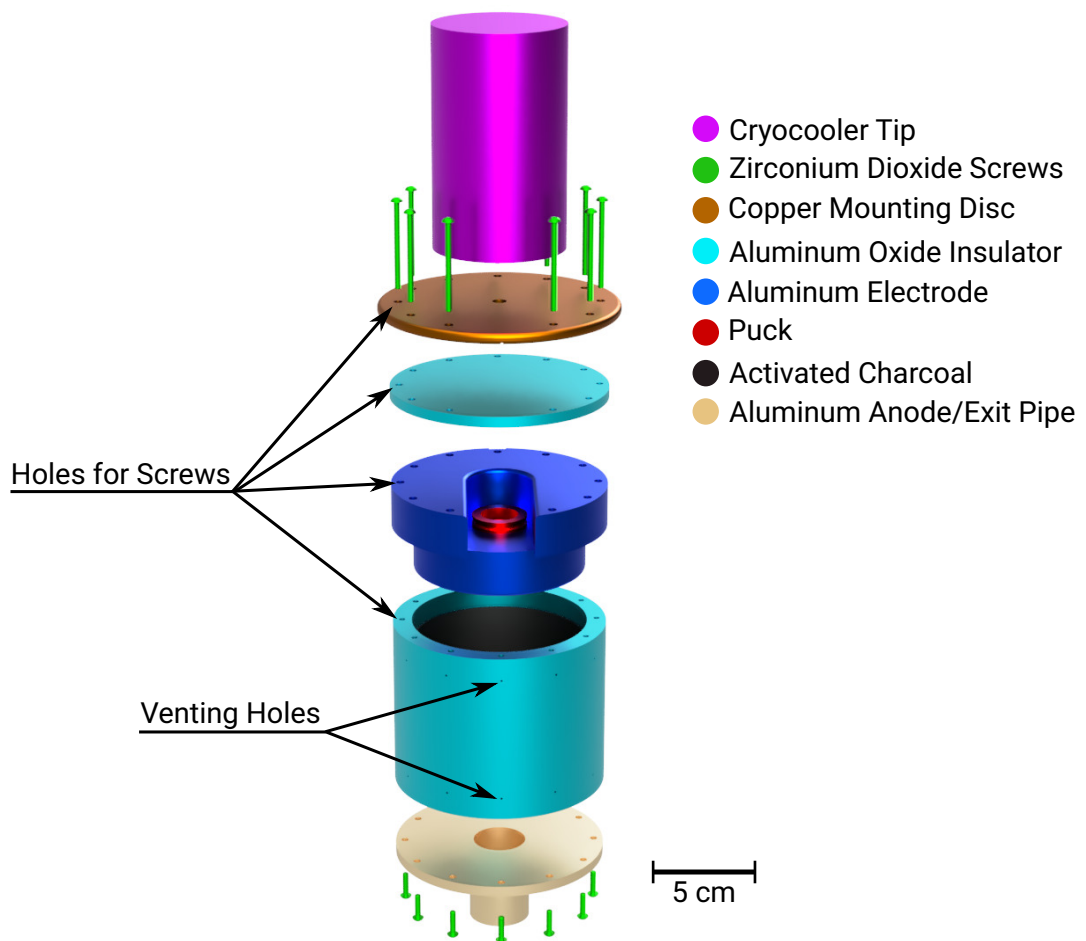


Figure 4.5: Exploded view of the cryogenic sub-volume. The top cylinder represents the tip of a closed cycle cryostat, which provides the cooling power. As a mounting base a copper disc is directly screwed to the cooler. An aluminum oxide disc electrically insulates the sub-volume from the cooler. The electrode and anode are made from aluminum and a hollow aluminum oxide cylinder acts as the walls of the sub-volume insulating the electrode from the anode electrically. The inner surface of this cylinder is coated with activated charcoal to create a cryo-pumping surface. The puck gets inserted into the electrode from the side via a manipulator. All parts are connected with zirconium dioxide screws.

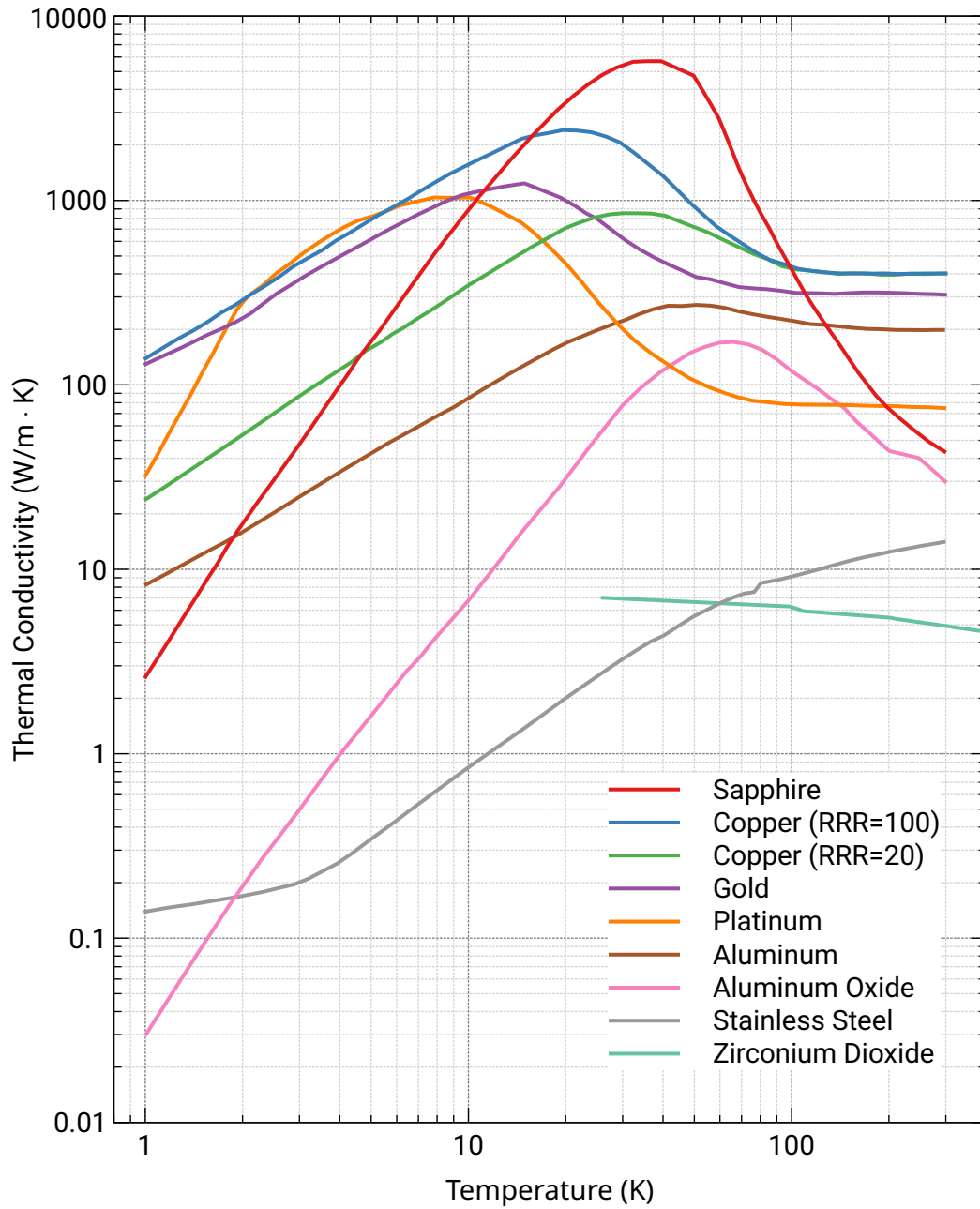


Figure 4.6: Thermal conductivity of the materials used and some additional, which may be relevant for future designs, plotted over the temperature. RRR stands for residual-resistance ratio and describes the ratio of the resistivity at room temperature and at 0 K. Source of data: [155, 156].

For the electrode, aluminum was chosen as it also shows a high thermal conductivity and requires lower bake-out temperatures compared to the commonly used stainless steel. The latter is of importance as the cryocooler only allows a maximal bake-out temperature of 170° C [157]. The electrode design of the Photo-CATCH gun, where the puck is inserted from the bottom via a lift cannot be copied. A z-translator on top of the chamber is necessary to move the lift, which is not an option as the top of the chamber is already occupied by the cryocooler. So a lateral insertion of the puck is the only feasible alternative. For this the electrode was cut out on one side to allow a manipulator to insert the puck from the side. To place the puck in the recess of the electrode, the manipulator needs to be movable vertically. Figure 4.7 shows a model of the electrode and the puck insertion process. To reduce a broadening of the electron beam or bunch due to space charge effects, the electrode features a so-called Pierce geometry with an angle of 67.5° at the bottom [158]. A small recess on the top allows to connect the h.v. cable.

Connected to the electrode is an insulating hollow cylinder also made from aluminum oxide, which forms the wall of the sub-volume. The inner surface of this cylinder is coated with activated charcoal to create a cryosorbing surface around the cathode. On the bottom, a cover disc with a hollow pipe for the electron beam to exit and the laser to enter made from aluminum closes the sub-volume. It also acts as a grounded anode to form an accelerating electric field.

All parts are connected using M3 screws made from zirconium dioxide⁵ (ZrO₂). They are screwed in through holes near the edge in each part from the top and the bottom into the aluminum oxide chamber walls. Zirconium dioxide like aluminum oxide is an electric insulator but exhibits a higher fracture toughness which makes the screws more resistant to breaking which could destroy the sub-volume, if the screw cannot be removed any more. Robuster screws also allow a higher torque and contact pressure, increasing the thermal conductance between each component. On the downside the thermal conductance of the zirconium dioxide screws itself is lower by a factor of about 10 compared to aluminum oxide screws. Small venting holes drilled through the chamber wall from the outside into the screw hole allows trapped gas to be pumped to prevent virtual leaks. To further increase the thermal conductance, indium foil⁶ was placed between all components. As the surface of the components are not perfectly planar, small gaps are present which result in a reduced contact area and a smaller thermal conductance. The soft indium foil fills these gaps.

⁵Z-700 E zirconium dioxide ordered from BCE Special Ceramics GmbH[®]

⁶0.1 mm thick 99.99% indium foil by Cryoandmore Budzylek GbR

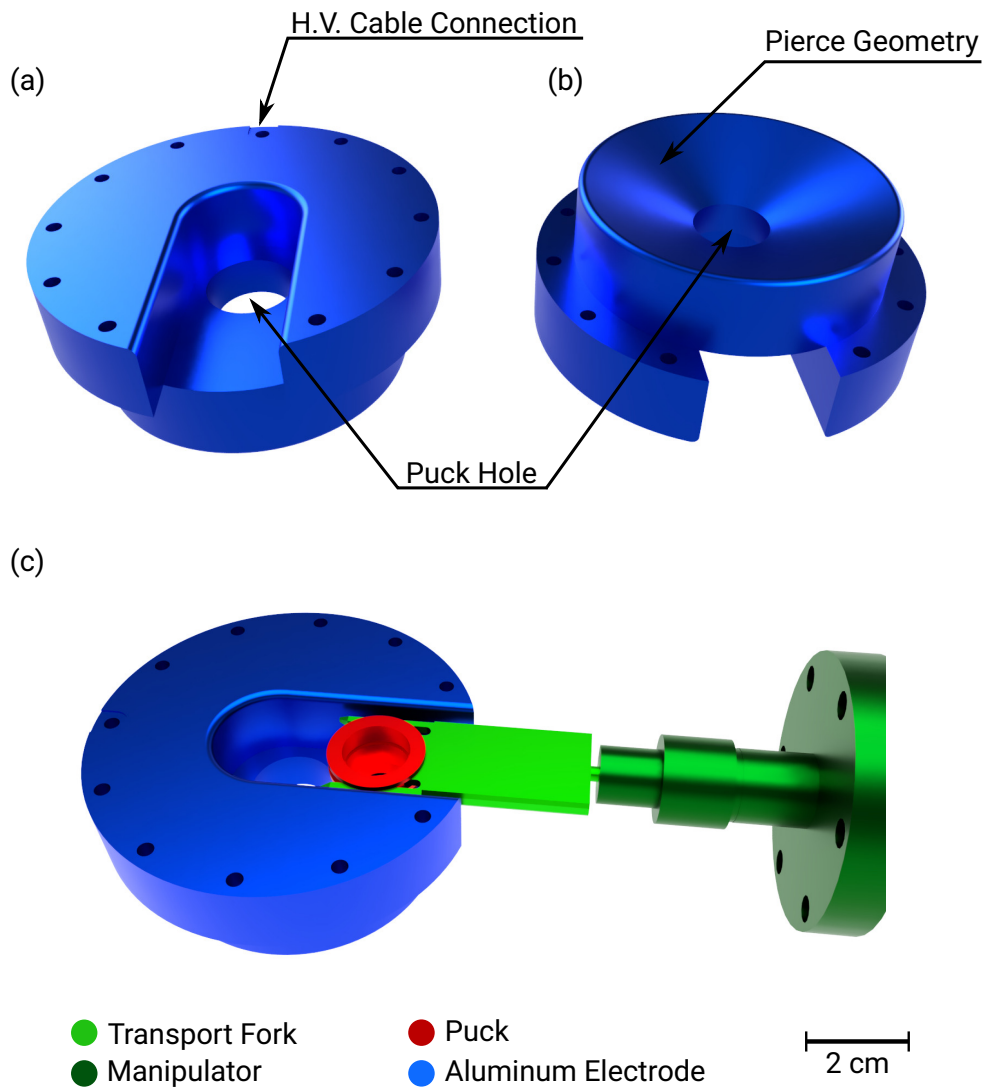


Figure 4.7: Top (a) and bottom (b) view of the electrode without puck. On the backside in the top view a recess for an eyelet to attach the h.v. cable using a screw can be seen. On the bottom of the electrode the Pierce geometry with an angle of 67.5° to reduce beam broadening due to space charge effects is visible. In (c) the insertion of the puck into the electrode is shown. The puck is held by a transport fork attached to a manipulator, which needs to be movable in the vertical axis to place the puck into the hole.

4.3.1 Exit-Pipe Dimension

The dimension of the pipe located at the bottom of the sub-volume (here called the *exit-pipe*) are of utmost importance for the vacuum condition inside the sub-volume and therefore, for the increase in lifetime. There are a few aspects to consider when choosing diameter and length of the pipe. Firstly, there are only two small openings to the sub-volume: the exit-pipe and one for the puck. Before inserting the cathode and activating the cooling, a sufficient initial pressure inside the inner chamber has to be achieved to not exceed the capacity of the cryopump. A larger diameter and a smaller pipe length result in a higher conductance and therefore, a better initial pressure will be reached in a shorter time. However, a higher conductance also result in a higher end-vacuum pressure in the sub-volume as more particle find their way into the inner chamber from the higher outside vacuum after the activation of the cryopump. Hence, one has to find a compromise between initial pressure, pump-down time and end-vacuum.

As the capture capacity of the cryopump (see Section 3.4) highly depends on the properties of the cryosorbent used and no data is available for the activated charcoal used in this work (see Section 5.1) the capacity of the pump cannot be calculated. However, one can get a rough estimate by comparison to a commercially available pump. Choosing a rather small cryopump with a comparable setup as described in Section 3.4.5 and a similar size of the cryopanel to the size of the cryogenic-sub volume the VCP 100 by HSR AGs[®] offers a capacity of 100 bar·l for argon and nitrogen and 4 bar·l for hydrogen. As argon and nitrogen get pumped on the uncoated outside of the cryopanel by cryocondensation, only the hydrogen capacity is relevant for the estimation. Assuming the used charcoal and the design of the source to be not ideal for a cryopump, the capacity is estimated to be worse by a factor of 10 compared to the commercial pump. This leads to a hydrogen capacity of 400 mbar·l. There will be two stages of the usage of this capacity, first the residual gas from the initial pressure inside the sub-volume gets captured, after that only gas molecules finding their way to the inside through the exit-pipe contribute to the gas load. To calculate a maximal acceptable initial pressure some simplifications have to be made. First it is assumed that all gas molecules inside the sub-volume gets captured⁷ by the charcoal and contribute to the depletion of the capacity in the same way. Second it is determined that a maximum of 1 % of the total capacity should be consumed by the initial gas load. Using the volume of the sub-volume of about 0.32 l, the calculation results in a maximum acceptable initial pressure of 12.5 mbar, which should be reachable even with a positive displacement pump only. As a result, the capacity of the cryopump should not be something to worry about when choosing the pipes dimensions. The used values

⁷Helium actually will not be pumped at the achievable temperature.

Table 4.1: Values and result for the calculation of the maximum acceptable initial pressure inside the sub-volume, without depleting the pumping capacity of the cryo sorbent.

Parameter	Value
volume of sub-volume	0.32 l
hydrogen capacity of VCP 100 cryopump	4 bar·l
assumed sub-volume capacity	400 mbar·l
maximum capacity consumed by initial gas load	1 % $\hat{=}$ 4 mbar·l
resulting maximum acceptable initial pressure	12.5 mbar

and the result of the calculation are summarized in Table 4.1.

However, the final pressure and the time to pump down the whole system remain important factors. The pressure ratio inside the chamber to the outside can be estimated by the flux of particles into the sub-volume and the capture rate of the cryo-surface. The former can be calculated using Equation (3.9) with the conductance C of the openings and the difference between the pressures p_{out} outside and p_{in} inside the sub-volume as

$$Q_{in} = C \cdot (p_{out} - p_{in}). \quad (4.1)$$

As the opening for the puck will be blocked by the puck itself during operation, only the exit-pipe contributes to the conductance and can be calculated for a gas with given temperature T and molar mass M by⁸ [159]

$$C_{pipe} = \frac{\pi \cdot d_{pipe}^3}{3l_{pipe}} \cdot \sqrt{\frac{R \cdot T}{2\pi \cdot M}}, \quad (4.2)$$

with the diameter d_{pipe} and length l_{pipe} of the pipe.

The absorption rate of the cryopump is the product of the pumping speed S and the pressure p_{in} in the chamber

$$Q_{out} = S \cdot p_{in}. \quad (4.3)$$

The pumping speed S can be calculated using Equation (3.11)

$$S_{cryo} = c \cdot S_{id} = c \cdot A \cdot \sqrt{\frac{R \cdot T}{2\pi \cdot M}}.$$

⁸This equation only holds for the molecular-flow regime.

Table 4.2: Estimated hydrogen pressure ratio between the inside of the cryogenic sub-volume and the surrounding outer chamber for different combinations of diameter and length of the exit-pipe. The dimensions chosen for this setup are marked in red.

Diameter (mm)	Length (mm)	p_{in}/p_{out}
40	30	0.366
30	30	0.196
30	40	0.155
25	40	0.096
24	40	0.086
20	50	0.042
10	50	0.005

In the equilibrium state, the flux into the chamber and the absorption rate are equal. From this the pressure ratio can be calculated by:

$$Q_{in} = Q_{out} \rightarrow \frac{p_{in}}{p_{out}} = \frac{C}{C + S}. \quad (4.4)$$

The ratios for some pipe diameter and length combinations have been calculated in Table 4.2 for hydrogen using a capture coefficient of 0.3 at 12 K [130].

Before bake-out, the outgassing of metal is dominated by H₂O which decreases over time. The rate of this decrease depends on the properties of the surface, its contamination and history. This cannot be calculated or simulated, only measurements can provide reliable data. Therefore, the time for the sub-volume to reach its final pressure cannot be estimated by calculations. The decision for an exit-pipe with 25 mm diameter and 40 mm length was made based on the calculated pressure ratios and experience with pump-down times for different vacuum systems [160].

However, Monte Carlo simulations can be used to calculate the final pressure inside and outside of the sub-volume. They have been conducted with the chosen pipe parameters using the software Molflow+⁹ developed at CERN [161], to determine the hydrogen pressure with the foreseen cryo gun chamber design and pump setup (see Section 4.5). A simplified model of the chambers was used to calculate the pressure at three locations;

⁹Molflow+ version 2.9.4 was used for the simulations.

Table 4.3: Hydrogen outgassing rates used in Molflow+ simulations of the cryogenic source and the Photo-CATCH gun chamber.

Material	Bake-out	H ₂ Outgassing Rate (mbar· l/s· cm ²)
aluminum	20 h at 100 °C	$4 \cdot 10^{-14}$ [162]
stainless steel	20 h at 200 °C	$2 \cdot 10^{-13}$ [162]

Table 4.4: The final hydrogen pressures calculated by Molflow+ for the cryo source and the Photo-CATCH gun chamber at cryogenic temperatures.

Location	Pressure (mbar)
sub-volume	$4.7 \cdot 10^{-16}$
between sub-volume and shield	$1.7 \cdot 10^{-14}$
outside of shield	$3.4 \cdot 10^{-14}$
inside Photo-CATCH gun chamber	$2.8 \cdot 10^{-14}$

inside the sub-volume, between the sub-volume and the heat shield, and outside of the shield. An activation of the NEG pumps to 50 % of their maximal pumping speed was assumed as they cannot be heated to the temperatures required for 100 % (see Section 4.5). It was presumed that the outgassing from all cryogenic components is so low that it can be neglected for this simulation, but there will also be no pumping effect from the non-coated cryo-surfaces for hydrogen. Only the inner wall of the sub-volume was set to a capture coefficient of 0.3 [130]. As a comparison to a conventional source the simulation was also done for the gun chamber of Photo-CATCH. The used outgasing rates for the involved materials can be seen in Table 4.3 and the pressure results in Table 4.4. Figure 4.8 shows the geometries of both chambers and the pressure at the defined locations.

As can be seen, the simulation predicts a pressure ratio (~ 0.0138) of about one magnitude lower than the calculations (~ 0.096). This is probably caused by the heat shield which was not included in the calculations but in the simulation. Comparing the results with the simulation of the Photo-CATCH gun chamber, a pressure in the same magnitude outside the shield in the cryo source and in the Photo-CATCH gun chamber can be expected.

Concluding from both, a hydrogen pressure one to two magnitudes lower than in the gun chamber of Photo-CATCH can be expected inside the cryogenic sub-volume. Assuming IBB to be the dominating lifetime limiting effect and IBB intensity to be proportional to

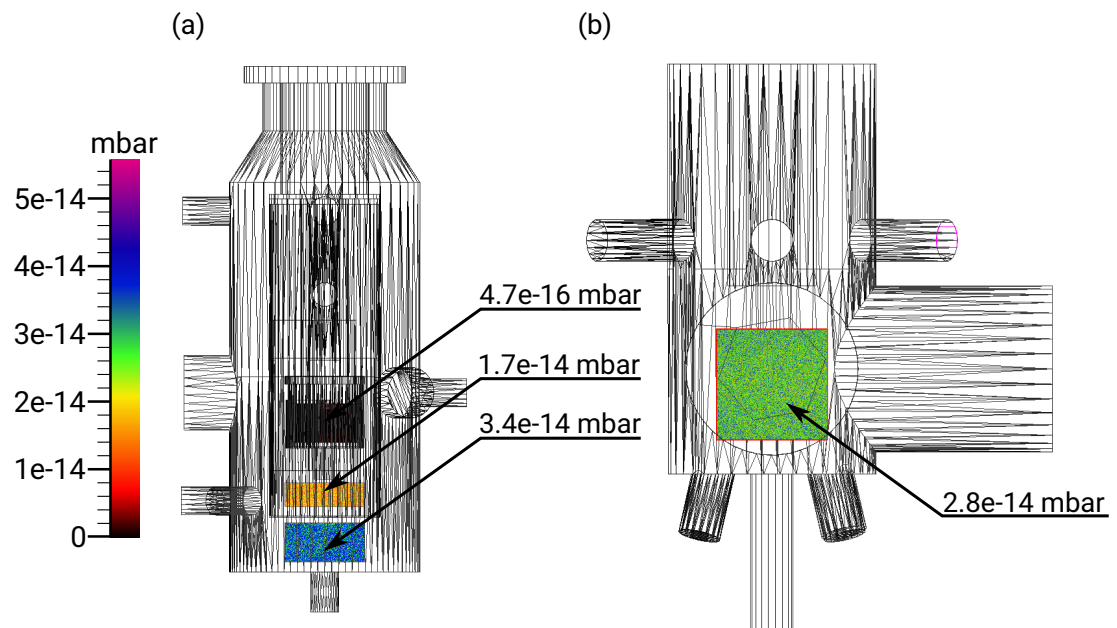


Figure 4.8: Simplified geometries of the cryogenic source chamber (a) and the Photo-CATCH gun chamber (b) used in Molflow+ simulations. The shown pressures are averaged over the colored evaluation planes by the software.

the amount of residual hydrogen molecules, an increase in charge lifetime by up to two magnitudes can be anticipated.

4.3.2 Electric Field and Field Emission

When the electric field gradient of the electrode reaches a critical value, electrons start to tunnel through the potential barrier and will be released into the surrounding vacuum. This so-called field emission will reduce the photocathodes lifetime (see Section 2.3.4) and needs to be prevented by a proper design of the electrode as well as the choice of a suitable material. The core aspects to reduce field gradient are to avoid sharp corners and to increase the space between the electrode and other conducting parts with different potential. Additionally, a proper polishing of the material is of importance as it produces a smooth surface without micro-edges and increases the field gradient limit. Before the maximum potential can be reached, a conditioning procedure of the electrode must be conducted. The potential is slowly increased until field emission occurs. This eliminates field

emitters from the electrode surface through ion bombardment and the resulting sputtering and ion implantation [163]. The effectiveness of this procedure can be increased by a gas conditioning technique with helium or krypton. A constant flow of the gas is introduced to the vacuum system to a pressure in the 10^{-5} regime while the ion pumps are turned off [164]. The voltage is increased until a field emission excess current is measured, then the increase is paused until field emission extinguishes and the voltage is increased further.

The most commonly used metal for electron gun electrodes is stainless steel, which shows an upper field emission limit of around 10 MV/m [120]. However, the thermal conductance of stainless steel is too low to achieve the necessary temperature. Also, steel requires a bake-out temperature between 200 °C and 220 °C for an acceptable outgassing rate, which is not compatible with the maximum bake-out temperature of the used cryocooler (see Section 4.4). Therefore, aluminum was chosen as electrode material. Mamun et al. measured a field emission limit between 5 MV/m and 5.4 MV/m with a mechanically polished bare aluminum electrode¹⁰ [165]. After a conditioning procedure with helium a limit between 8.5 and 12.0 MV/m could be reached.

For copper electrodes, an increase of the maximum field gradient of up to 50 % was observed by cooling it to 30 K [166]. Concluding from this a similar increase for aluminum is expected.

To assess the field gradient and estimate an upper limit for the potential, the electric field of the electrode was simulated with the software CST Studio¹¹. CST offers different solvers for different problems, like an electrostatic solver for the electric field or the particle in cell (PIC) solver for particle tracing. For the calculations CST creates a mesh by decomposing the space and the model into discrete cells. Depending on the problem and the used solver a hexahedral or tetrahedral mesh can be chosen. For round objects a tetrahedral mesh provides better results with less cells, however, the PIC solver only allows a hexahedral mesh. In each cell the Maxwell equations are solved based on the finite integration technique using a matrix formalism [167].

To reduce calculation time, a simplified 3D-model of the sub-volume including the heat shield was created and loaded into CST. The mesh type was set to tetrahedral. A material library is included in CST to define the properties of the components, however, for conductors CST only offers the choice of a perfect electrical conductor (PEC), other electrical resistivity and conductivity are not taken into account in the simulation. Therefore, the

¹⁰Two electrodes were measured, the first one performed worse with a maximum field gradient between 3.0 and 3.6 MV/m.

¹¹CST Studio Suite 2020®

electrode, all other metal parts and the activated charcoal was specified as PEC. For the insulator, aluminum oxide from the included library was chosen. The potential of the electrode was altered between -5 kV and -30 kV, while the potential of the anode was set to 0 kV (grounded). The resulting electric fields are shown exemplary for 30 kV in Figure 4.9. As can be seen, the highest field gradient occurs at the edge of the Pierce angle geometry at the bottom of the electrode. There is a small gap between the electrode and the chamber wall to prevent the creation of virtual leaks in the space between them. The second highest gradient is at the top between the electrode and the copper mounting disc. The graph in Figure 4.10 shows the maximum field gradient according to the simulations for different electrode potentials. As expected, a linear relation can be observed. At -30 kV a maximum field gradient of 11.1(1) MV/m can be expected. Depending on the conditioning results and the effects of the cooling -30 kV may be achievable with this design. Electron guns used at accelerators usually operate with potentials of up to -300 kV, so -30 kV is rather low. This is owed to the design limitations such as the lateral insertion of the puck, the size limitations at Photo-CATCH and to the fact that the electrode is placed inside the sub-volume and not freely like in most other guns. For an operation at the S-DALINAC or other accelerators higher currents or bunch charges are needed, requiring higher electron energies and electrode potentials. However, this source is designed as a proof of concept to demonstrate a lifetime increasing effect by the means of placing the cathode inside a cryogenic sub-volume. For this purpose a lower potential will be sufficient.

4.3.3 Simulation of the Electron Beam

Besides calculating the electrical field, CST is also capable of calculating the movement of charged particles in the field numerically, taking the Lorentz force and space-charge effects between the particles into account. Using the PIC solver the electron beam was simulated to assess the transversal spread and the center shift of the electron beam. The algorithm calculates the movement of the particles in time steps Δt using the Newtonian equations. The size of the time steps are defined by the smallest mesh cell [168]. Since for the simulation of a 10 pC electron bunch over $6 \cdot 10^7$ particles and over $18 \cdot 10^{14}$ interactions would be required, CST uses so-called macro-particles to reduce calculation time. The total charge q_b is distributed over the total number of macro-particles N

$$q_b = \sum_{i=1}^N q_i. \quad (4.5)$$

Where the charge q_i of a single macro-particle can be larger or smaller than the elemental charge of $e = 1.602 \cdot 10^{-19}$ C. The charges below the elemental charge are used by the

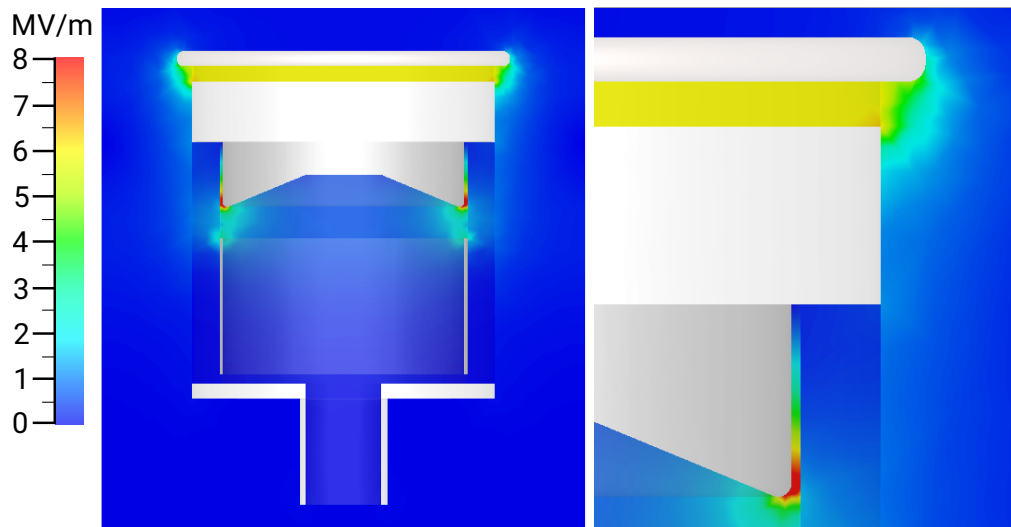


Figure 4.9: Electric field gradient around the electrode for a potential of -30 kV. The highest gradient can be observed at the edge of the pierce geometry and between the top and the copper disc. For illustrative reasons the color scale was limited to 8 MV/m, the actual maximum field gradient at -30 kV is 11.1 MV/m.

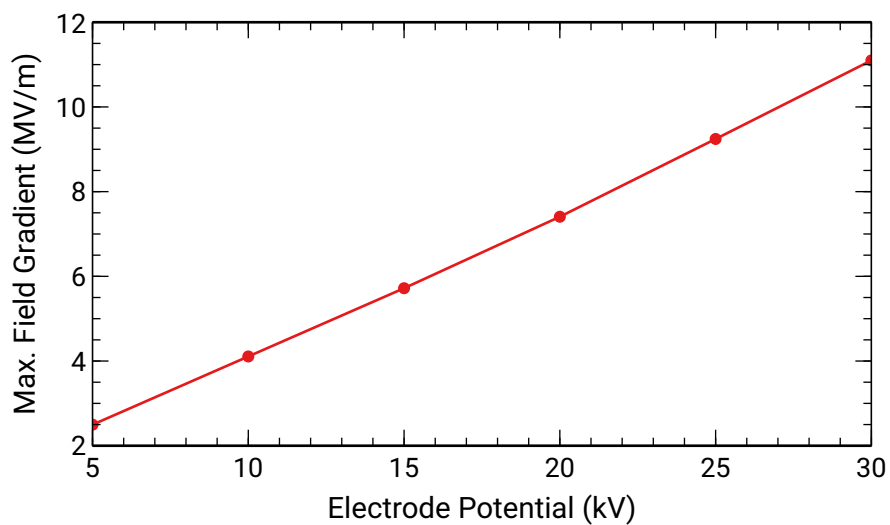


Figure 4.10: Maximum electric field gradient according to CST simulations for different electrode potentials. A linear relation can be observed.

software to represent a charge density lower than the density of macro-particles at that location. The count of macro-particles is defined by the number of emission points on the particle source surface, which can be configured in the settings. More emission points result in longer calculation times and larger data files but better statistics.

At the surface of the electrode, where the cathode will be located, a circular particle source was defined. There are multiple settings to specify the parameters of the source. The particle type can be chosen and was set to electrons. As the used laser system (see Section 4.7) only allows a DC operation, the electron beam was set to a DC beam as well. The cutoff radius of the emission surface was set to 500 μm and the transverse emission profile to a Gaussian distribution following the profile and size of the laser spot.

The emission direction of the i -th particle is characterized by the polar angle θ_i and the azimuth angle ϕ_i . In CST they are distributed uniformly among all particles with $0^\circ \leq \theta_i \leq \theta_{max}$ and $0^\circ \leq \phi_i \leq 360^\circ$, where θ_{max} can be set in the particle source properties. It was set to the maximal possible value of nearly¹² 90° which corresponds to a root mean square (RMS) angle θ_{rms} of

$$\theta_{rms} = \sqrt{\langle \theta^2 \rangle - \langle \theta \rangle^2} = \frac{\Delta \theta_{max}}{\sqrt{12}} \approx 26^\circ. \quad (4.6)$$

This angle is below the angle of $\theta_{rms} \approx 29^\circ$ derived from experimental data in [90], but it is the highest possible in CST, as the uniform distribution is fixed in the software. Figure 4.11 shows the emission point distribution on the circular surface as well as the emission angles.

The emission energy of the electrons was calculated for the used laser wavelength of 450 nm which corresponds to a photon energy of 2.76 eV. The energy gap of GaAs at the minimal achievable temperature of the puck of 19 K is 1.52 eV. From this follows an upper energy limit of the emitted electrons of $2.76 \text{ eV} - 1.52 \text{ eV} = 1.24 \text{ eV}$.

The 3D-model was oriented in a way that the electron beam travels along the z-axis and the origin is located in the middle of the emitting surface. Table 4.5 summarizes the used source parameters. An example of the visual beam representation created by CST is shown in Figure 4.12 for -12 kV electrode potential and a beam current of 500 μA . The particles shown are the macro-particles and do not provide insight into the real charge distribution. In the figure a shift of the beam's center can be seen. This is an artifact created by the way the software places the mesh, which does not create a symmetrical mesh distribution.

The results of the simulation can be exported as a table of all macro-particles at a specified time, which contains the phase-space information $(x_i, y_i, z_i, p_{x,i}, p_{y,i}, p_{z,i}, q_i)$ of

¹²An angle of exactly 90° would mean a non-physical emission in only transverse direction.

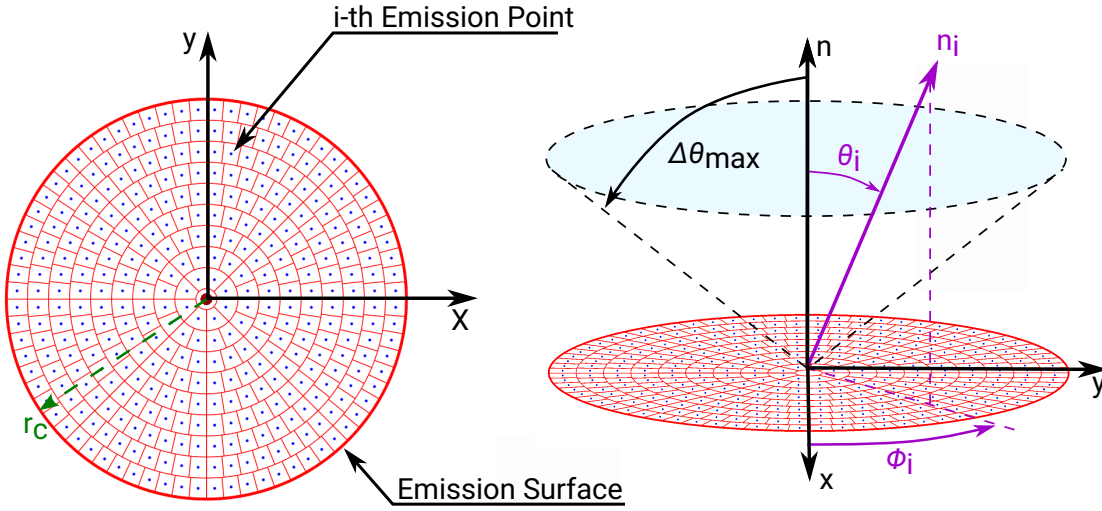


Figure 4.11: On the left side the circular emission surface as defined in CST with the individual emission points (blue) of the macro-particles is shown. The surface is limited by the set cutoff radius $r_c = 500 \mu\text{m}$. The right side shows the emission angle for an arbitrary particle, which is emitted in a polar angle θ_i and azimuth angle ϕ_i to the surfaces normal. The angles for all particles are distributed evenly with $0 < \theta_i < \theta_{max}$ and $0 < \phi_i < 360$. Graphic based on [169, Fig. 4.8].

all $i = 1, \dots, N$ macro-particle of the beam. From these date the beam envelope can be obtained. It describes the transverse electron spread along the beam line. For that a weight factor w_i for each macro-particle needs to be defined as

$$w_i = \frac{q_i}{q_t}, \quad \sum_{i=1}^N w_i = 1. \quad (4.7)$$

Using this factor, the arithmetic mean $\langle x \rangle$ and the variance $\langle x^2 \rangle$ can be calculated by [169]

$$\langle x \rangle = \sum_{i=1}^N w_i x_i \quad \langle x^2 \rangle = \sum_{i=1}^N w_i (x_i - \langle x \rangle)^2, \quad (4.8)$$

here shown for the x component. In accelerator physics usually the root mean square values are calculated. As the source is cylinder symmetrical with the beam center in the

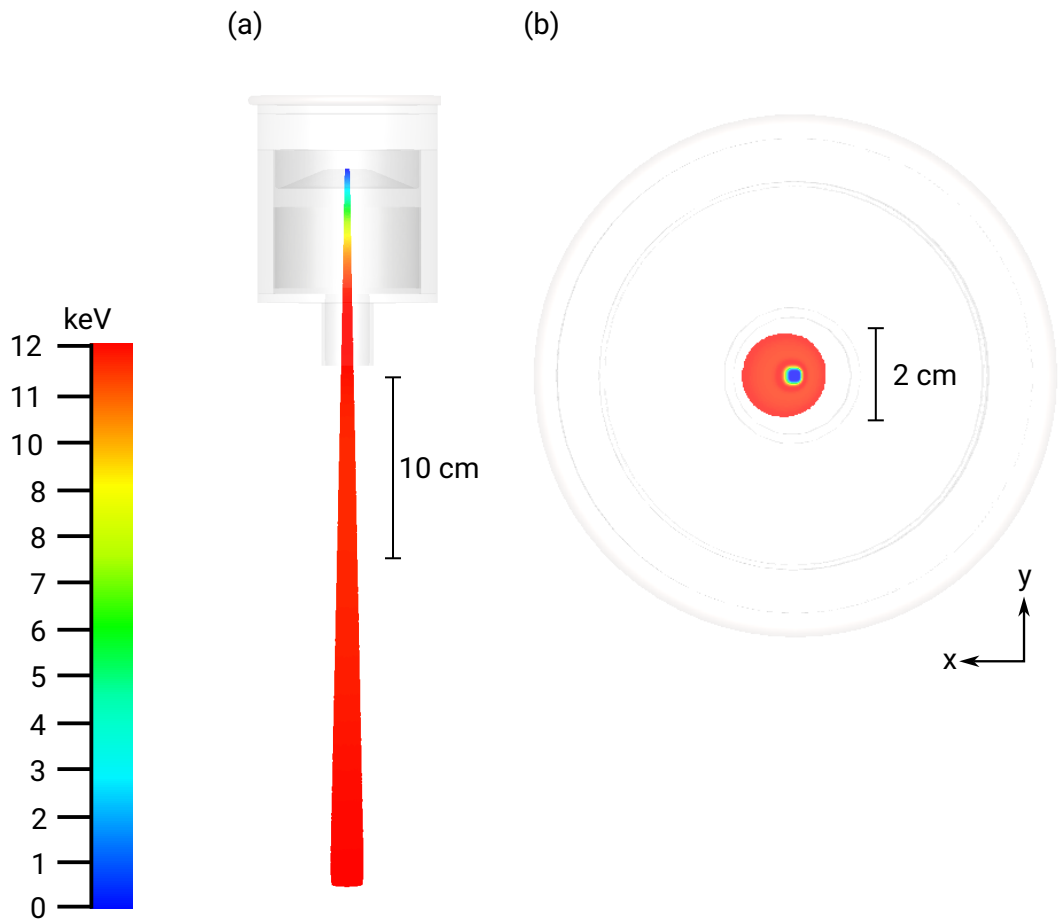


Figure 4.12: Visual representation of the macro-particle beam generated by the PIC solver of CST. The beam originates from the cathode surface inside the sub-volume, gets accelerated by the set potential, exits the volume and is terminated at a distance of 33 cm where the first quadrupole magnet is located. The energy of the particles increases from the cathode to the exit-pipe and stays constant after leaving the sub-volume and the accelerating field. The shown beam only represents the spatial distribution of the macro-particles used by the solver, which does not provide insight into the real distribution of the charge and the electrons. In (a) the beam is shown in a side view and in (b) from the top. One can see a small shift of the beam center. This is an artifact created by the way the software places the mesh. The shown simulation was conducted with -12 kV electrode potential and a current of $500 \mu\text{A}$.

Table 4.5: Parameters of the particle source used to simulate the electron beam in CST.

Parameter	Value
anode potential	0 V
electrode potential	-12 kV to -30 kV
particle type	electron
transversal emission profile	Gaussian
longitudinal emission profile	DC
laser spot cutoff radius	0.5 mm
emission angle	89.999°
DC beam current	10 μ A to 100 μ A
number of emission points	841
number of mesh cells	44 · 10 ⁶

origin the arithmetic position mean $\langle x \rangle$ equals to zero¹³. So in this case the standard deviation equals the root mean square diameter envelope $d_{rms,x}$ which can be written as

$$d_{rms,x} = \sqrt{\langle x^2 \rangle} = \sqrt{\sum_{i=1}^N w_i x_i^2}. \quad (4.9)$$

To be consistent with nomenclature in literature the term root mean square is used in this dissertation.

The envelope for the x and y components should be identical due to the cylinder-symmetrical geometry. However, due to the mentioned placement of the hexahedral mesh slight differences can be observed. Therefore, the values for both axis were averaged as

$$d_{rms} = \frac{d_{rms,x} + d_{rms,y}}{2}. \quad (4.10)$$

The effect of the heat shield on the results was evaluated in one simulation comparison¹⁴, which showed a maximal difference of 2 % for all calculated values. Therefore, the shield was removed from all further simulations to reduce simulation time. The differences were taken into account in the given errors accordingly.

For the evaluation the particle positions were exported at 6 ns, when the beam reached a distance of around 33 cm, the point where the first beam-shaping element (quadrupole

¹³Here the shift due to the mesh placement is neglected.

¹⁴The simulation was done with -12 kV electrode potential and 100 μ A beam current.

Table 4.6: Beam divergence for different potential and beam current combinations calculated from the beam waist at 0.2 m and 0.33 m. All values are in mrad.

	10 μA	100 μA	500 μA	1000 μA
-12 kV	4.04(1)	4.13(1)	4.51	5.00(1)
-15 kV	3.66(1)	3.73(1)	4.02(1)	4.41(1)
-20 kV	3.18(1)	3.23(1)	3.43(1)	3.68(1)
-25 kV	2.87(1)	2.90(1)	3.05(1)	3.24(1)
-30 kV	2.62(1)	2.65(1)	2.76(1)	2.91(1)

magnet) will be located in the final setup (see Section 4.8). The envelope was calculated at multiple points along the beam, for which the beam was cut into slices of 1 cm length, which provided enough statistic in each slice of around 80.000 macro-particles. The simulation was run for different electrode potentials from -12 kV to -30 kV and different beam currents from 10 μA to 1 mA. The results are plotted in Figure 4.13. As can be seen the potential has a greater influence on the envelope than the beam current. The highest RMS beam-diameter of 3.5(1) mm can be observed for -12 kV and 1 mA after a distance of 33 cm. Higher currents are not possible with the current laser system (see Section 4.7). The pipe diameter at the quadrupole magnet is 40 mm and the diameter of the sub-volume exit-pipe 25 mm. Beam loss due to the broadening of the beam caused by space charge effects is not expected according to the simulation.

The divergence Θ_{div} is an angular measure describing the increase in RMS beam-radius with distance from the cathode. It is typically measured in milliradian (mrad = mm/m) and can be calculated from the envelope

$$\Theta_{div} = \frac{\Delta r_{rms}}{\Delta z} = \frac{\Delta d_{rms}}{2\Delta z}, \quad (4.11)$$

with the envelope radius $r_{rms} = 0.5 d_{rms}$. The divergence for all simulated potential and current combinations were calculated from the RMS values at a distance of 2 cm and 33 cm. They are listed in Table 4.6 and reach from 2.62(1) mrad for a 10 μA beam at -30 kV to 5.00(1) for a 1000 μA beam at -12 kV. For comparison the electron gun STEAM at the Mainz University shows a divergence of 2.2 mrad at -100 kV while the newly developed PKA gun exhibits a divergence of only 0.6 mrad [169]. The difference may originate from different parameters like differing potentials, laser spot diameters, space charge or starting energy of the electrons due to another laser wavelength.

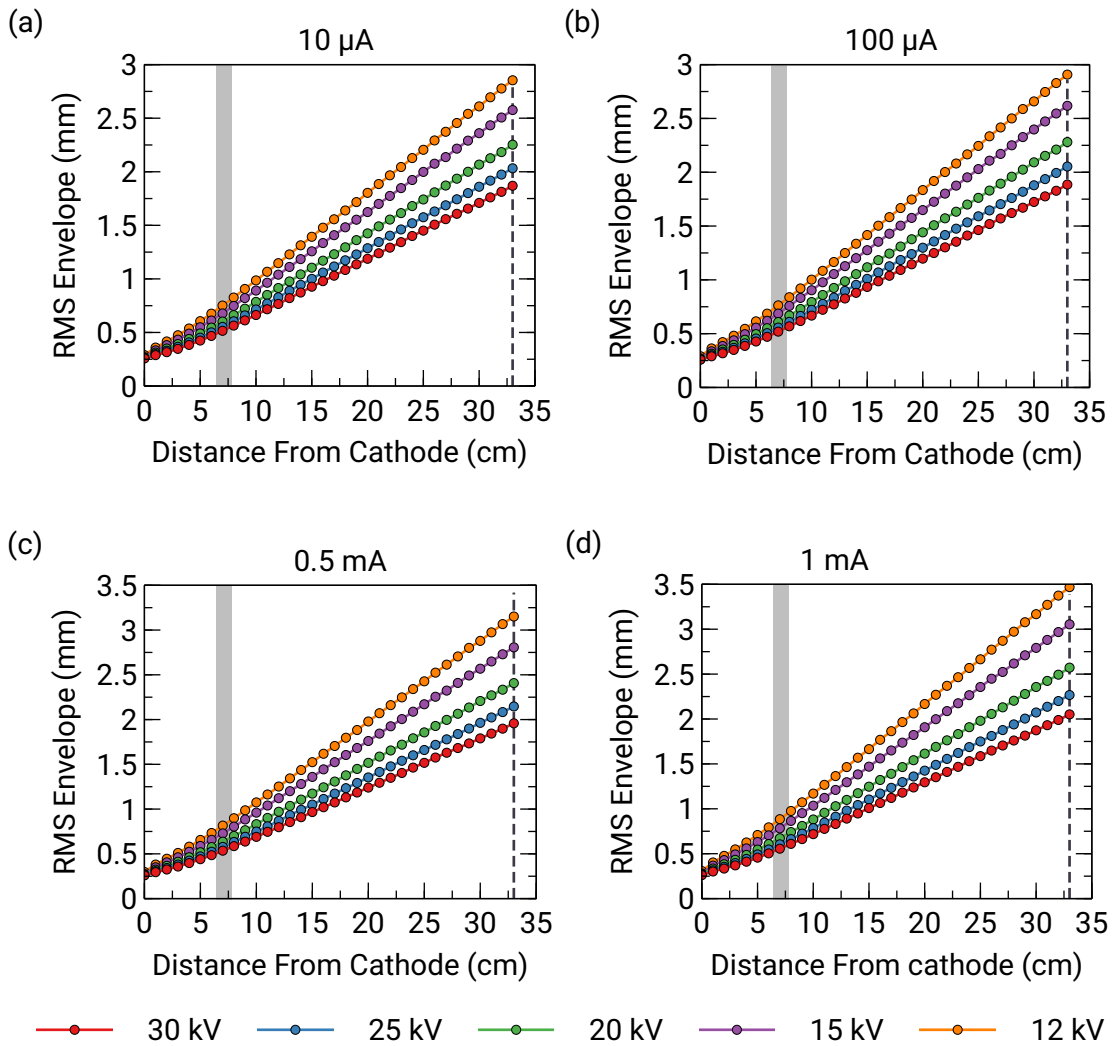


Figure 4.13: CST Simulation results of the electron beam-diameter envelope at different distances from the cathode surface for multiple beam currents and electrode potentials. Marked is the location of the exit tube at 7.1 cm to 10.1 cm in gray and the beginning of the quadrupole magnet at 33 cm in black. Note the different scales for the different beam currents in (a) and (b) vs. (c) and (d).

A perfectly centered alignment of the laser spot on the cathode may not be possible due to the limited visibility into the closed sub-volume. Therefore, the behavior of an off-axis beam was simulated. The particle source was moved 5 mm to one side, which corresponds to the radius of the puck opening. The macro-particle distribution for a potential of -12 kV and a beam current of 500 μA , illustrated in Figure 4.14, shows no particle loss even under maximum misalignment of the laser. However, a transverse shift of the beam center of 9.7(1) mm after 26 cm can be observed. At that distance the first steerer magnet is located, which can compensate the shift and re-center the beam. For comparison the shift due to the mesh placement at that position is 0.1(1) mm in both axis.

Another source for a beam shift is given by the earth magnetic field. The first setup of the test stand will not feature a Helmholtz coil like Photo-CATCH to compensate this field. Later along the beamline the shift can be compensated by the steerer magnets, but in the space between the cathode and the first steerer the beam is most prone to the external field. Especially the inside of the sub-volume is critical as the electrons have not yet reached their final velocity. In CST a vertical magnetic background field in x-direction with 20 μT [170] was configured and the simulation has been carried out for different electrode voltages and beam currents. Figure 4.15 illustrates the macro-particle beam for -12 kV with 500 μA and shows that no particles are lost inside the sub-volume. For other currents no significant change in the shift could be observed. At the location of the first steerer (26 cm) a center shift of 1.9(1) mm was calculated.

The new test stand is not designed to measure beam-quality parameters (see Section 4.8). Also, the focus of this work is the improvement of the lifetime, not beam quality. Therefore, additional beam quality parameters are not discussed and calculated here. However, the emittance which describes the volume of the electron ensemble in six-dimensional phase space has been used as starting point for further simulations to determine the compatibility of the Photo-CATCH beamline with the cryogenic source (see Section 4.9).

4.4 Cryocooler and Heat Assessment

There are two options to provide the cooling power for the cryopump. The first would be the use of a cooling fluid like liquid nitrogen or helium. This would require a steady flow of new fluid. In our laboratory no supply for any kind of cooling fluid is available, so there would be the choices of building one or to use a tank which needs to be refilled by hand periodically. Both options are not feasible as building a supply would go beyond the financial and time scope of this work and manually filling a tank inside the laboratory

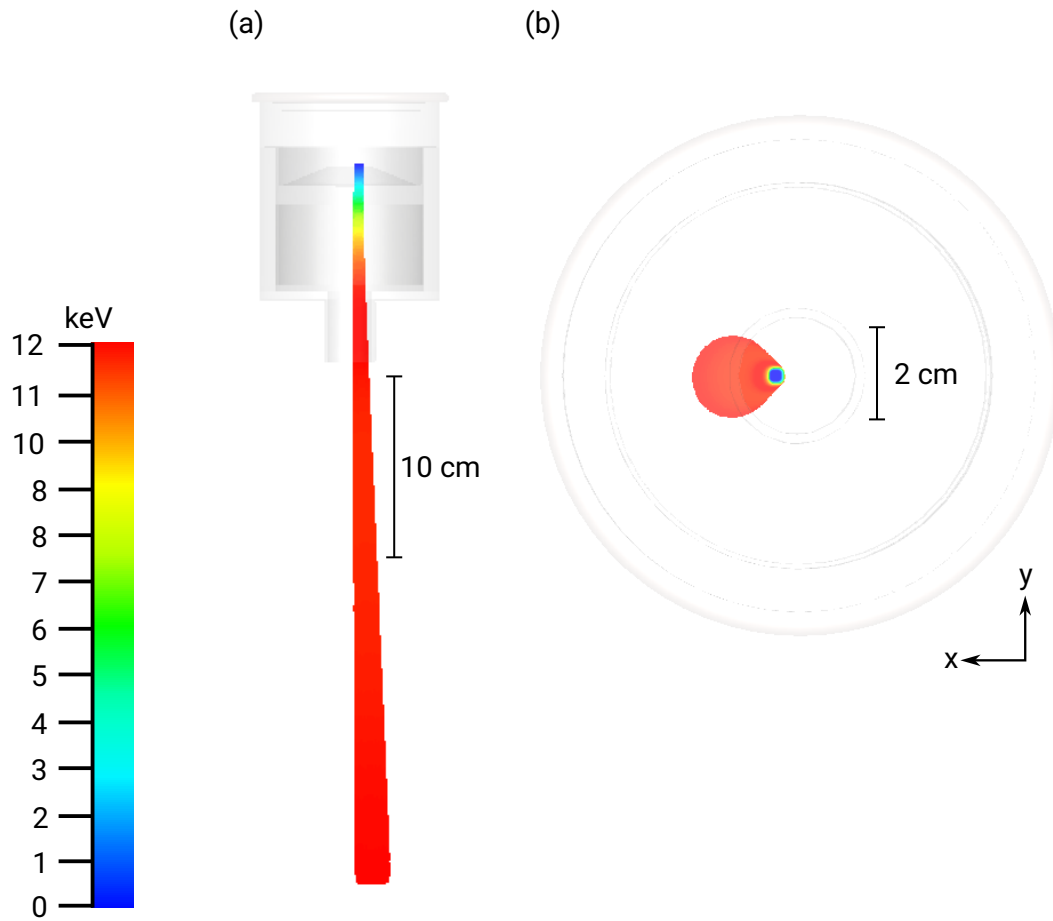


Figure 4.14: Visual representation of the macro-particle beam when the source origin is shifted by 5 mm in positive x-direction. This analyses the influence of a not perfectly centered laser spot. In the side view (a) it can be seen that no particle gets lost by hitting the walls. In the top view (b) the shift is clearly visible. The shown simulation was conducted with -12 kV electrode potential and a current of $500 \mu\text{A}$.

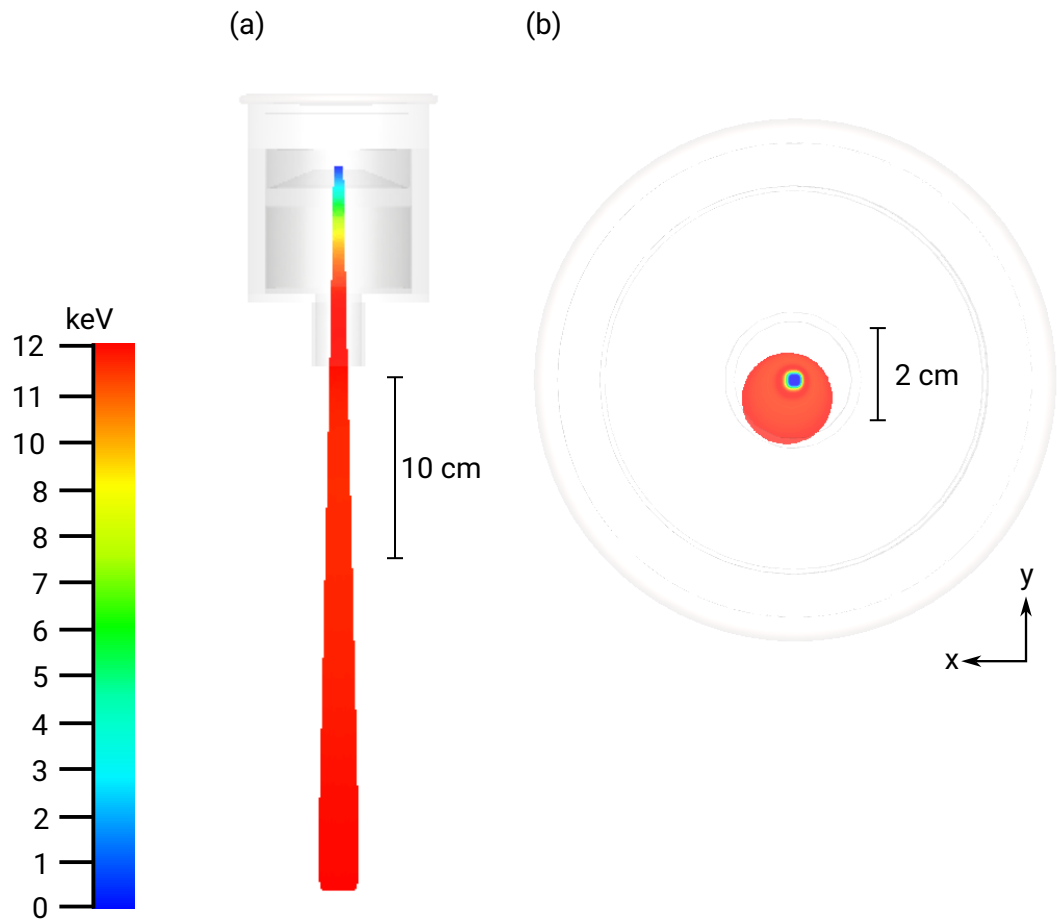


Figure 4.15: Visual representation of the macro-particle beam with a $20 \mu\text{T}$ horizontal magnetic background field in x-direction representing the horizontal component of the earth magnetic field at the location of the laboratory. In the side view (a) it can be seen that no particle gets lost by hitting the walls. In the top view (b) a shift in x and y-direction is visible, where the latter is created by the magnetic field while the x-shift is the already mentioned artifact of the mesh distribution. The shown simulation was conducted with -12 kV electrode potential and a current of $500 \mu\text{A}$.

is not possible while the source is in operation due to safety reasons. So the only option remaining is to use a refrigerator with a closed cooling fluid cycle (also referred to as cryocooler). There are a variety of commercially available options for such a device, with different cooling power and properties. Most of them use helium as cooling fluid and a compressor to create a closed circle. The gas gets compressed, transferred to the refrigerator where it gets expanded. There are two stages with different temperatures. On the warmer first stage a heat shield is attached to reduce heat radiation from the outside onto the cooler second stage at which the experimental setup, in this case the cryogenic sub-volume, gets attached.

A cryocooler from Advanced Research Systems¹⁵ (ARS) was chosen. It provides a cooling power of 1.1 W at 4.2 K and can reach a minimal temperature of < 4 K. One disadvantage that this type of refrigerators shows is a vibration of the cooler tip with an amplitude of 10 - 30 μm caused by the expansion of the cooling gas/fluid. This vibration would transfer to the electron beam and render it unusable for most experiments. ARS solves this problem with a low-vibration interface which reduces the vibrations to an level acceptable for the use in an electron gun operated at an accelerator. Figure 4.16 shows a schematic representation of the setup. The interface sits around the cooler and is connected through soft rubber mounts which dampen the vibration. The transfer of the cooling power is done via an exchange gas, in this case helium, between cooler and vibration interface. The interface reduces the cooling power to 1 W at 4.6 K but also dampens the vibration to an amplitude of < 500 nm. Even lower vibrations below 50 nm can be achieved by removing the soft mounts and mounting the head to a separated rig, which is detached from the interface mount. As vibrations < 500 nm are sufficient for a first evaluation of a lifetime-increasing effect a setup with soft mounts were chosen. However, for future sources e.g. at the S-DALINAC or when developing cold sources for large-scale accelerator applications a separated rig may be a way to increase beam quality. The vibration interface like the cryocooler itself, features two stages of which the first one is used to connect a heat shield and the second for the experimental setup. To allow higher bake-out temperatures, the cooler can be removed from the interface without breaking the vacuum. However, this requires enough space on top of the cooler as it needs to be pulled out upwards. Due to a limited room height in the Photo-CATCH laboratory, however, the bake-out needs to be done with the cryocooler in place. An inlet allows to refill the exchange gas on first setup or after removal of the cooler. On the upper part the self-sealing tubes for the cooling fluid are connected. For a flexible placement of the compressor tubes with 9 m have been ordered. For temperature measurement three sensors are included, one is directly integrated into the cooler's tip, the others can be placed freely. A 75 Watt heater is

¹⁵Advanced Research Systems Inc. CS210SF-GMX-20B

Table 4.7: Relevant properties of the cryocooler (CS210SF-GMX-20B by ARS) given by the manufacturer. The values for cooling power are with the use of the low-vibration interface.

Property	Value
1. stage cooling power at 77 K	60 W
2. stage cooling power at 4.5 K	1 W
minimal achievable temperature 2. stage	< 4 K
cooldown time to 5 K (no additional load)	2 h
vibration amplitude using soft mounts	< 500 nm
vibration amplitude using separated rig	< 50 nm
maximum bake-out temperature cryocooler	170 °C
maximum bake-out temperature low-vibration interface	200 °C
maximum magnet field at sampleholder	< 50 μ T
heater power	75 W

integrated into the cooler to stabilize the temperature at a set value. A DN150 CF-flange on top allows the cooler and the interface to be placed into a vacuum chamber.

The heat shield is made from aluminum and was electro-polished to reduce emissivity. It exhibits 8 holes, one on the bottom for the electron and laser beams, one to insert the puck, two for high-voltage cables and four to increase the vacuum conductance for a faster pump-down time.

The helium compressor is run by a 380 V 3-phase 50 Hz power supply and is connected to the supply of cooling water available in the laboratory to take away the heat load from the cryocooler. Table 4.7 summarizes the most important properties of the cryocooler and the vibration interface.

4.4.1 Heat Assessment

To assess if the provided cooling power will be sufficient, a rough estimation of the heat load onto the cryocooler was calculated. As written in Section 3.4.4 there are four components which contribute to the total heat load of which the heat load through residual gas can be neglected in the molecular-flow regime [130]. Therefore, it will not be considered in the estimation of the total heat load.

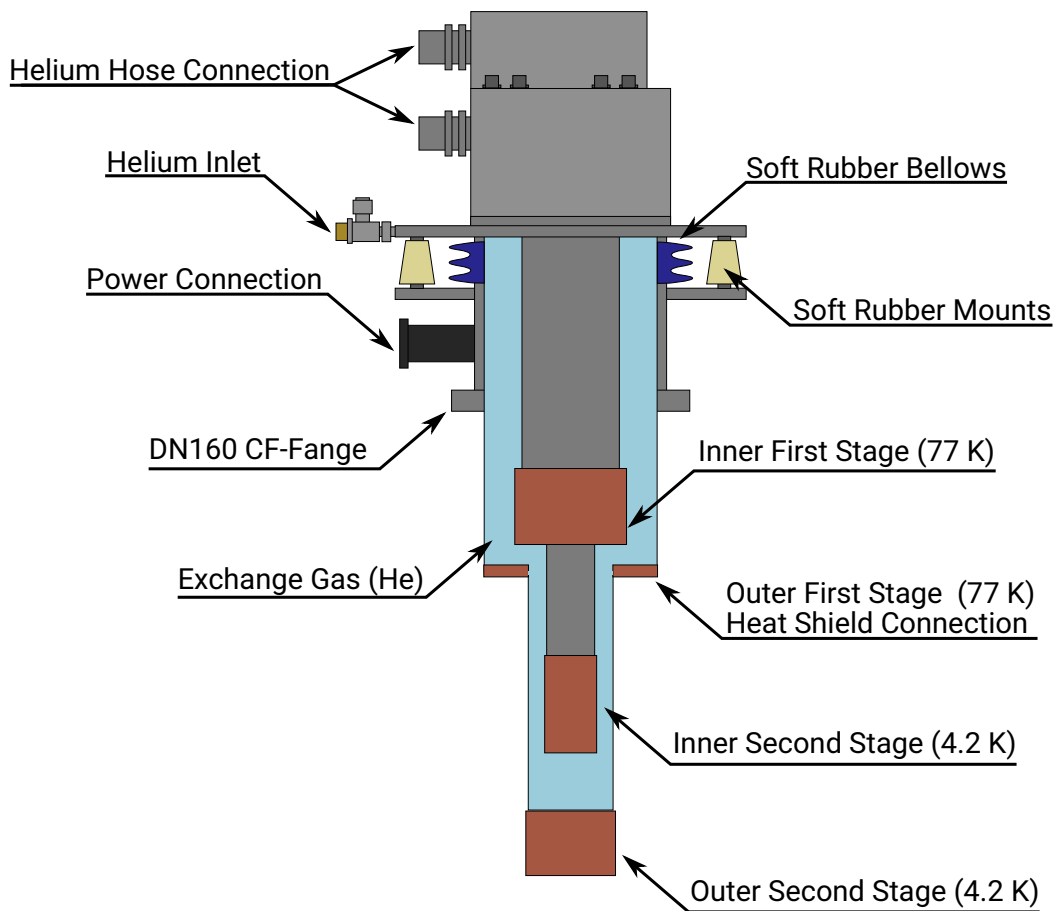


Figure 4.16: Schematic representation of the used cryocooler with attached low-vibration interface. The cryocooler sits inside the vibration interface and is only connected through soft rubber mounts which dampens the vibrations from the cooler. Soft rubber bellows contain the exchange gas helium between vibration interface and cooler. The gas transfers the cooling power to the interface without transferring the vibrations. It can be refilled through a helium inlet. On top of the cooler two connections for the helium hose to the compressor are located. To connect the cooler to a vacuum chamber a DN 150 CF flange can be used. The heat shield gets mounted at the first stage of the vibration interface.

Table 4.8: Emissivity of relevant materials used in the heat assessment calculations. The nearest fitting temperatures were used.

Material	Temperature (K)	Component	Emissivity
aluminum, mech. polished	370	outer chamber	0.095 [172]
aluminum, mech. polished	4.2	inner chamber	0.06 [147]
aluminum, electro-polished	77	heat shield	0.08 [147]
stainless steel, mech. polished	77	cryocooler	0.12 [147]
aluminum oxide	not given	insulator	0.4 [173]
copper, unpolished	4.2	mounting plate	0.06 [147]

The heat load q_R introduced by thermal radiation can be calculated using Equation (3.17). But to get accurate values the viewing factor is required. It can be calculated analytically for simple geometries, but for more complex ones only simulations using raytracing can produce accurate values. The used geometry is rather complex with different materials of not exactly known emissivity. However, a rough estimate can be done using Reference [171] which yields

$$\dot{q}_R = \frac{\sigma A_1 (T_1^4 - T_2^4)}{\frac{1}{\epsilon_1} + \frac{A_1}{A_2} \left(\frac{1}{\epsilon_2} - 1 \right)}, \quad (4.12)$$

with the Stefan–Boltzmann constant σ and the area A_i , the temperature T_i and the emissivity of the inner (1) and outer (2) surface, respectively.

There are two radiation components to consider. The first is the radiation coming from the heat shield to the sub-volume. The temperature of the sub-volume is assumed to be 20 K as this is the temperature limit over which no significant hydrogen pumping is possible [132]. For the temperature of the shield the official information from the manufacturer of 77 K were used. The cooling power at that temperature is specified with 60 W. A heat load of 0.02 W was calculated using the emissivity values given in Table 4.8. The second radiation heat load origins form the holes in the shield. It can be calculated to 0.21 W, which is one magnitude higher than the radiation from the heat shield. Due to a temperature dependence of the power to 4 and the room temperature of the outer chamber this was to be expected. A compromise between heat load and gas flux had to be made when choosing the size and number of holes in the shield.

Table 4.9: Enthalpy differences $\Delta H(80\text{ K} \rightarrow 4\text{ K})$ for some gases in kJ/mol [148].

N ₂	H ₂	D ₂	T ₂
9.3	3.308	3.483	4.075

The heat load due to conduction through the high voltage cable¹⁶ can be calculated using Equation (3.15). The used cable has a radius of 0.5 mm and an approximate length of 0.7 m. With the thermal conductivity integral from 0 K to 290 K of 152 kW/m [147] a heat load of 0.23 W follows.

When using Equation (3.18) with the enthalpy transfer values given in Table 4.9 and the pressures from simulations in Section 4.3.1 one finds that the heat load created by the cryosorption and condensation can also be neglected, as they are multiple magnitudes below the load created by radiation and conduction through the h.v. cable.

An additional heat source in photo-guns is introduced by the power deposited by the laser. For an estimate the power absorption or reflection coefficient of the cathode needs to be taken into account. For GaAs the reflection coefficient for a laser with 450 nm lies between 0.6 and 0.7 [108]. So a heat load of 60-70 % of the laser power can be assumed. However, parts of the reflected light may not leave the sub-volume, hit the walls instead and get absorbed eventually. Therefore, as an upper limit estimation it is assumed that 100 % of the lasers power contributes to the heat load. The used laser diode (see Section 4.7) has a maximal power of 80 mW where only a fraction arrives on the cathode surface due to reflections and absorption on different components as mirrors, lenses and the fiber. A maximal power of around 12 mW was measured after the window at the setups bottom.

Table 4.10 summarizes all heat-load sources and shows the total heat load of 472 mW, which is below the 1 W provided by the cryocooler at 4.2 K. So a temperature below the critical 20 K can be expected. However, due to a limited thermal conductivity especially at lower temperatures a final temperature above 4.2 K should be anticipated.

4.5 Vacuum Chamber

The used cryocooler only allows a bake-out temperature of up to 170 °C with the cooler attached [157]. Removing the cooler from the low-vibration interface allows higher temperatures. However, due to the limited room height and the lack of a crane at the location of the setup, the removal was not possible. Therefore, the vacuum chamber housing

¹⁶© KAP-BAND-L-AWG20-HV30

Table 4.10: Estimated heat load onto the cryogenic-sub volume and the cryocooler due to different effects.

Component	Heat Load \dot{q} (W)
radiation through holes in shield	0.21
radiation from heat shield	0.02
conduction through h.v. cable	0.23
heat due to laser power	0.012
total heat load	0.472

the source was made from aluminum¹⁷, which requires a lower bake-out temperature of 120 °C compared to stainless steel. An additional advantage of aluminum is the lower total outgasing rate after bake-out compared to stainless steel [174]. The lowest record for total outgasing of U15C stainless steel is actually lower than the one of aluminum but requires annealing of the chamber at 1000 °C and a bake-out at 360 °C which is not feasible for a cryogenic source at our facility [175].

To better distinguish this chamber from the sub-volume housing the cathode (see Section 4.3) it will be called *outer chamber* or in accordance with the gun chamber of Photo-CATCH cryo gun chamber (CGC) from here on. A rendered image of the chamber is displayed in Figure 4.17. The whole chamber was split into two parts connected by a DN250 CF-flange for easier assembly and disassembly. This is necessary for the installation of the high voltage cable, which needs to be attached to the inner chamber and the feedthrough before closing the chamber. For this purpose two DN40 CF-flanges are attached to the top part as a feedthrough. One for the high voltage of the electrode and a second for a future test with a potential applied to the anode. On the top a DN160 CF-flange is attached for the cryocooler. On the lower part multiple DN40 CF-flanges are present for a residual-gas analyzer (RGA), a vacuum gauge, the feedthrough for the NEG activation cables, for the insertion of the puck and one at the bottom as an exit for the electron beam. Two DN63 CF-flanges for viewing ports allow to see the puck when inserting into the heat shield and the inner chamber. To connect an IGP¹⁸ a DN100 CF-flange is attached. For a future integration of the source into Photo-CATCH the whole chamber was designed in a way to fit into the test stand. As there will be little space on the sides the viewing port and the puck insertion flange are oriented towards the front, while the remaining flanges are oriented towards the back of the chamber.

¹⁷The AluVac® series chamber was manufactured by Vakuum Komponenten & Messtechnik GmbH.

¹⁸Gamma Vacuum 45S-CV-4D-SC-N-N

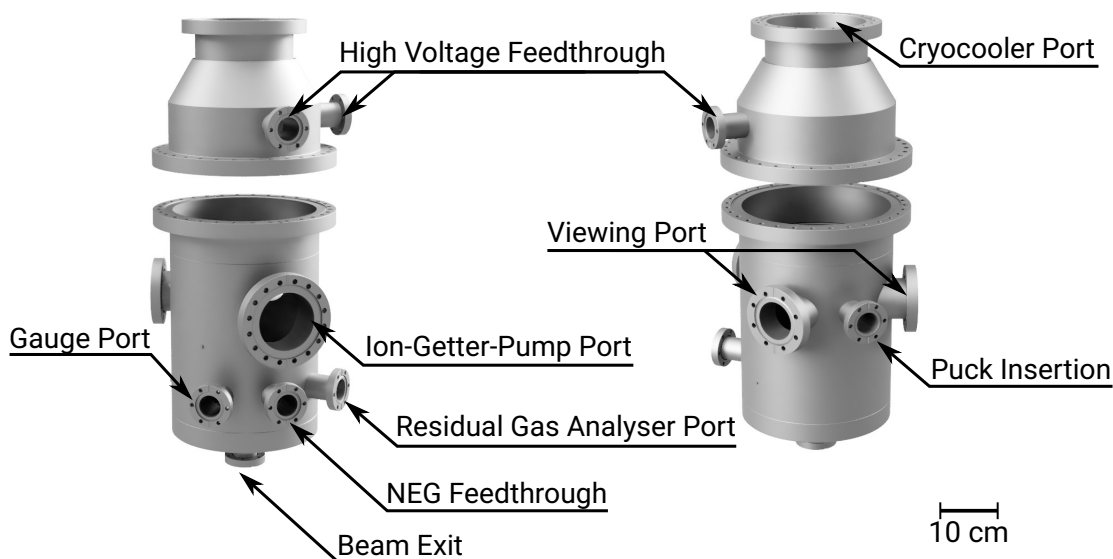


Figure 4.17: Render of the outer DN250 vacuum chamber of the source. The whole chamber is split into two parts for easier assembly and disassembly. The upper part is equipped with flanges for the cryocooler, the high voltage feedthrough for the electrode and a second feedthrough for the anode. The lower part includes flanges for a vacuum gauge, a residual-gas analyzer, the feedthrough for the NEG activation cables, an exit for the beam, an insertion port for the puck and two viewing ports. 3D file courtesy of [®].

On the inside mounts for four NEG wafer modules are attached to the walls. The used modules¹⁹ require a relative low activation temperature for NEG pumps. Figure 4.18 shows the activation times and temperatures needed for different efficiency percentages. guarantees a safe bake-out of the aluminum chamber up to 120 °C with a short exceed to 160 °C for 30 minutes. As can be seen from Figure 4.18 even for 20 % efficiency a higher temperature is required. Due to limited space at Photo-CATCH the size of the chamber only allows a mounting of the modules close to the chamber walls as well as to the aluminum heat shield. So an activation of the NEGs without heating the chamber and the shield to much cannot be guaranteed. To work around this problem a pulsed activation is planed, where the NEGs are heated until the chamber wall temperature increases too much, then the activation is turned off until the chamber temperature drops and the

¹⁹Saes[®] WP 950-St 707[®] wafer module

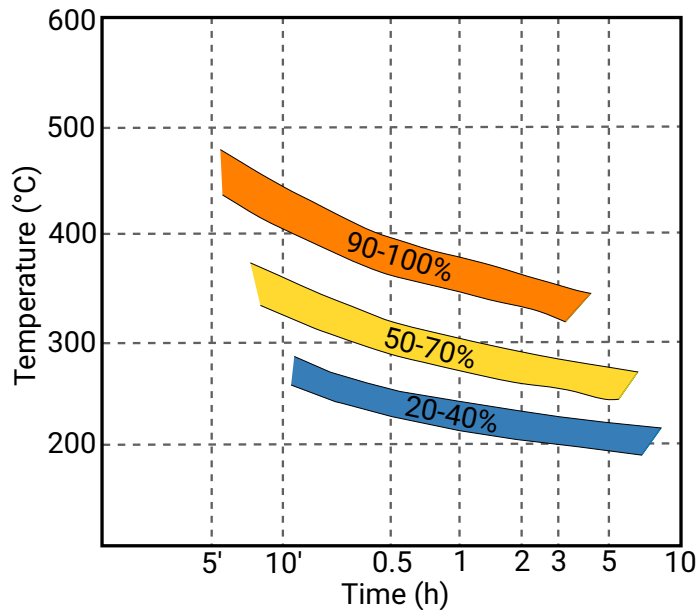


Figure 4.18: Temperature and time required for the activation of the NEG modules installed in the CGC to a certain efficiency. At temperatures below the shown curves no activation can be achieved, even with longer durations. Source of data: [176].

activation is started again. This procedure is repeated until a sufficient pumping efficiency is reached. Figure 4.19 shows a cut view of the complete assembled CGC including the sub-volume, vacuum pumps, gauge, heat shield and the cryocooler.

4.6 Transport Chamber

As the separated test stand for the cryogenic source does not feature any activation capabilities, activation of the cathode need to be done at Photo-CATCH. Hence, a way to transfer the cathodes without destroying the NEA layer is required. A transport chamber, designed by Kurichyanil [43] and assembled in corporation with him was used for this task. It was originally intended to transfer cathodes cleaned at Photo-CATCH using hydrogen cleaning to SPIIn at S-DALINAC. As it was never tested with activated cathodes, its performance in keeping the NEA layer in place was measured as part of this work. In this section the chaber design will be presented, for the measurement results see Section 5.2.

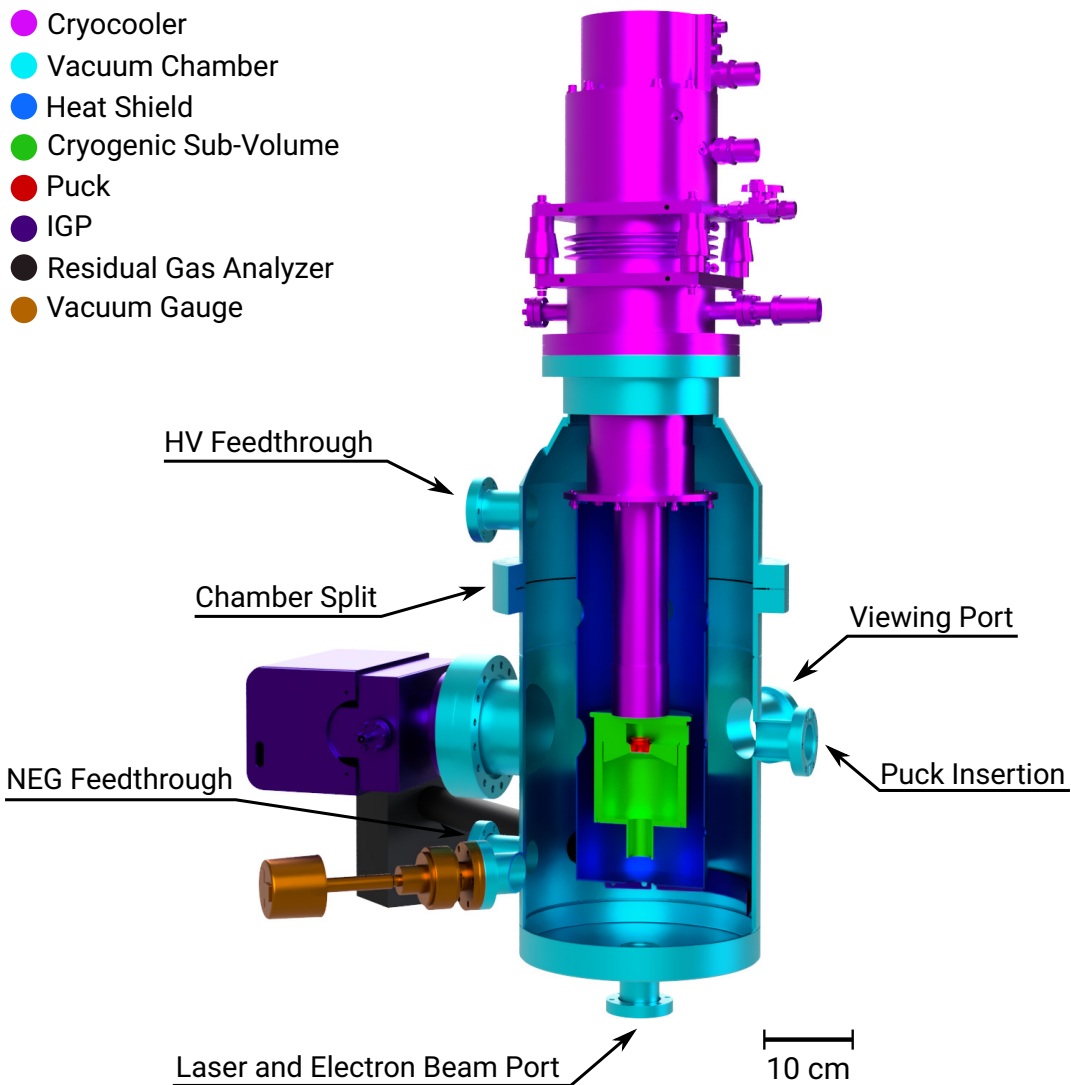


Figure 4.19: Cut-away view of the cryo source assembly with cryocooler, cryogenic sub volume, heat shield, pumps, manipulator and vacuum gauge. Not visible are the NEG pumps as they are located behind the shield and at the cutout. 3D file of the chamber courtesy of VACOM®.

A 3D design of the transport chamber is shown in Figure 4.20. It consists of a DN40 stainless-steel chamber equipped with a 400 l/s NEG pump which can maintain a vacuum in the lower to mid 10^{-11} regime after bake-out. On the other end a window is located to view the stored cathodes. At the chamber bottom a hand-operated gate valve and a quick CF-flange system²⁰ (QCF) adapter is connected. The QCF system features a special flange with a clamping chain and allows fast docking to the load-lock chamber of Photo-CATCH and the cryo test stand, reducing transfer times. A vacuum sensor allows monitoring of the pressure inside the chamber. Pucks with cathodes are stored in two stacked carousels, which can hold up to three pucks each. For insertion of the pucks the carousels are attached to a manipulator which allows them to be lowered into the LLC, where the local manipulator can be used to place or remove pucks into or from the carousel. Using a magnetic coupled manipulator instead of a z-translator with a threaded rod like the ones used on the chambers of Photo-CATCH ensures a faster transfer time into the transport chamber. This is especially important as the load-lock chambers are usually the ones with the highest pressure (low 10^{-8} mbar to high 10^{-9} mbar regime) and therefore, degenerate the NEA layer the most.

4.7 Laser Setup

Figure 4.21 shows a measurement of the quantum efficiency and the degree of polarization as functions of the laser wavelength for superlattice GaAs cathodes. As can be seen the peak polarization lies around 780 nm while QE increases continuously with lower wavelength, but the slope drops significantly below 775 nm. At Photo-CATCH a diode laser with 780 nm is used as it provides the best compromise between QE and polarization for most experiments with polarized electrons. However, this measurement was done with a cathode near room temperature and therefore, does not apply to a cryogenic cathode. Sturck et al. showed a shift of the absorption coefficient of GaAs with lower temperatures [177]. From these results a shift of the QE and polarization curve is expected as well for cryogenic cathodes. Using Equation (2.14) the temperature-dependend energy gap can be calculated. Using the values of Table 2.1 result in an energy gap of about 1.42 eV or 870 nm for room temperature and about 1.52 eV or 817 nm for 19 K, which is the lowest temperature achievable for the puck with the setup used in this work (see Section 5.3.3). So a maximal shift of 53 nm can be expected for the energy gap. If one assumes the same shift for the quantum efficiency and polarization the ideal wavelength for optimal polarization and reasonable QE would be 727 nm. However, high polarization is not the focus of this work but longer lifetime. Therefore, measurements will be made with bulk

²⁰QCF flange with clamping chain VaCFix[®]

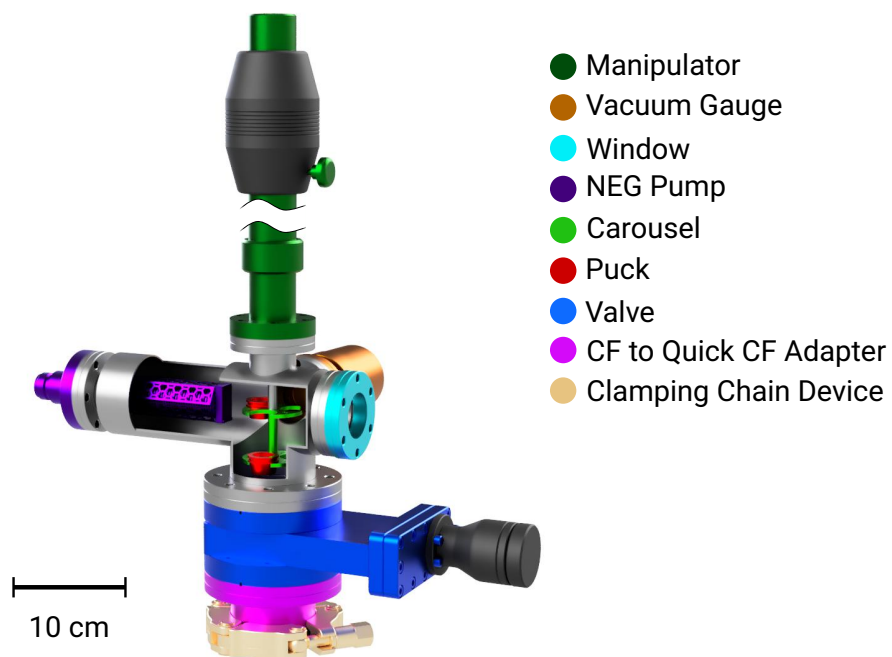


Figure 4.20: Transport chamber used to transfer cathodes activated at Photo-CATCH to the cryogenic test stand. A hand-operated gate valve and a quick CF flange system with clamping chain allows fast docking of the chamber to the Load-Lock chambers. Pucks housing the cathodes are stored in two carousels attached to a manipulator, which allows transfer of the carousels to the attach chamber. Pressure is maintained by a NEG pump and monitored during docking by a vacuum sensor. A window allows viewing of the stored pucks.

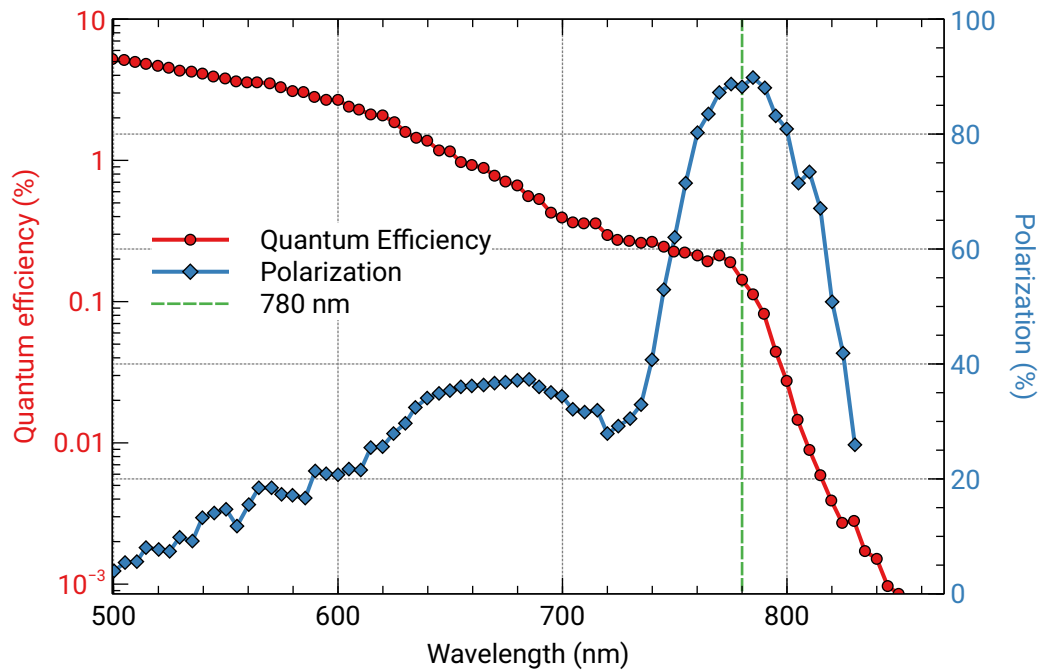


Figure 4.21: Quantum efficiency and the degree of polarization as function of the laser wavelength, measured for a previously used strained superlattice GaAs cathode from SVT Associates. The polarization shows a peak at around 780 nm while the QE rises continuously with lower wavelength and shows a drop of the slope at around 780 nm. The wavelength used at Photo-CATCH (780 nm) is marked in green. Source of data: [178].

GaAs cathode rather than superlattice, due to limited availability of the previously used SVT strained-superlattice cathodes. A diode laser with 450 nm was chosen to ensure a high QE even after a possible NEA degeneration due to the transport from Photo-CATCH.

The laser setup consists of two parts, one assembled on a laser table with a laser diode coupled into a fiber and a small assembly at the cryo test stand where the beam gets coupled out of the fiber, and directed through a window onto the cathode surface. Both can be seen schematically in Figure 4.22. The setup on the laser table starts with a 450 nm 80 mW laser diode²¹ which is mounted in a collimation package²² consisting

²¹Roithner Lasertechnik SHD4580MG

²²Thorlabs® LTN330-A

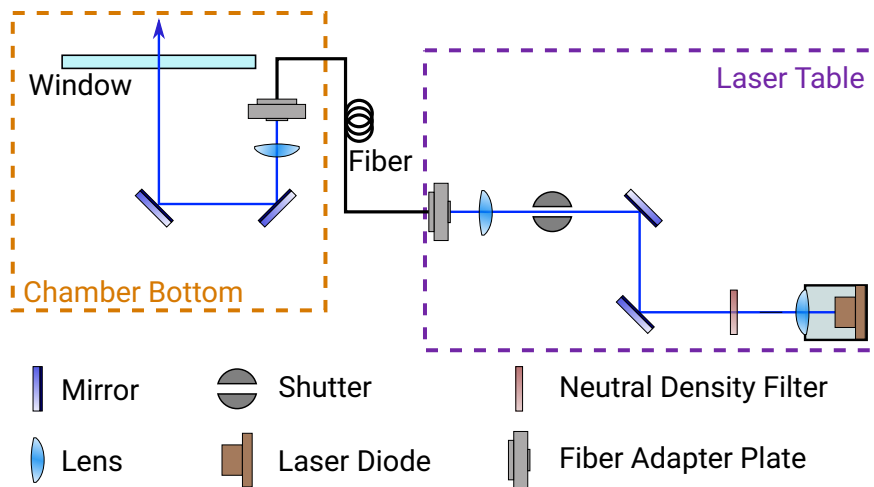


Figure 4.22: Schematic representation of the cryo-source laser system. The setup consists of two parts; the first with the laser diode coupling into an optical fiber is located at a laser table. The second part is mounted to the bottom window of the cryogenic test stand. It features a decoupling and two mirrors to align the beam onto the cathode surface.

of a mounting tube and a aspheric lens. The tube is mounted in a self designed and in-house manufactured mount including a thermo-electric cooling element connected to a temperature controller²³. After the mount a neutral density filter is located to control the laser power. Two adjustable silver mirrors²⁴ follow to guide the beam into a lens²⁵ and a multi-mode optical fiber patch cable²⁶ mounted to a fiber adapter plate²⁷. Between the focus mirrors and the lens a remote controlled shutter is located to block the beam when not needed. Because a later implementation of the cryogenic source into Photo-CATCH will use a 780 nm laser, not all components were optimized for a wavelength of 450 nm, and the laser-beam diagnostics did not feature an online measurement of the laser power. Therefore, a hand held power meter²⁸ has to be used.

²³Toptica DTC 110

²⁴Thorlabs[®] PF10-03-P01

²⁵Thorlabs[®] C220 TMD-A

²⁶Thorlabs[®] M42L05

²⁷Thorlabs[®] SM1FC FC/PC

²⁸Thorlabs[®] PM100D with S121C power sensor

Due to the closed design of the cryogenic source the laser alignment proved to be a complex task, which has to be done before closing the chamber (see Section 5.3.2 for the exact procedure). Also, the laser assembly on the chamber needs to be removed after alignment for the bake-out procedure. Therefore, a high mechanical stability and reproducibility are essential. From experience with the laser setup on the activation chamber a more complex setup with a live power measurement before the beam enters the chamber leads to a higher mechanical instability of the array resulting in larger fluctuations of the laser spot on the cathode. Therefore, a design with only essential components was chosen for the cryo source which reduces the lever effect of a longer laser beamline and ensures higher mechanical stability. The setup consists of a fiber adapter plate²⁹, a collimation lens³⁰ and two dielectric mirrors³¹. All components are mounted to an in-house manufactured mount. It can be seen attached to the test stand in Figure 4.23

4.8 Dedicated Test Stand

At the time of the assembly of the cryo source Photo-CATCH was not available for greater reconstruction works as it was in active use for other experiments. Therefore, a separated dedicated test stand was designed and assembled. It is shown as a model in Figure 4.24. As it is intended as a temporary solution for a first validation of the expected lifetime improvement, only essential elements are included in the design. The core components are the cryo source itself inside the aluminum vacuum chamber and a Faraday cup, which is used to measure the current of the electron beam [179]. From the decay of the beam current over time the cathodes lifetime can be calculated. As the laser beam enters the source chamber from the same direction the electron beam exits it, the cup cannot simply be placed at the end of the aluminum chamber.

To solve this problem, a magnet is attached at the end of the source chamber, bending the electron beam in an alpha-shaped path, therefore, called alpha magnet [180]. The beam is bent by 270° or effectively 90° which allows the laser beam to enter from the bottom unhindered while the electrons get deflected to a horizontal beamline. The magnet is placed on the outside of a rectangular shaped so-called *alpha chamber*, which provides enough space for the beam to be bent without hitting the walls. Wheels and a 45° angled rail on which the alpha magnet sits, allows the magnet to be transferred out of the way for bake-out of the alpha chamber. The rail is connected to a frame which allows movement in all three directions as well as tilting to some degree.

²⁹Thorlabs® SM1FC FC/PC

³⁰Thorlabs® AC254-060-B-ML

³¹Thorlabs® BB1-E02

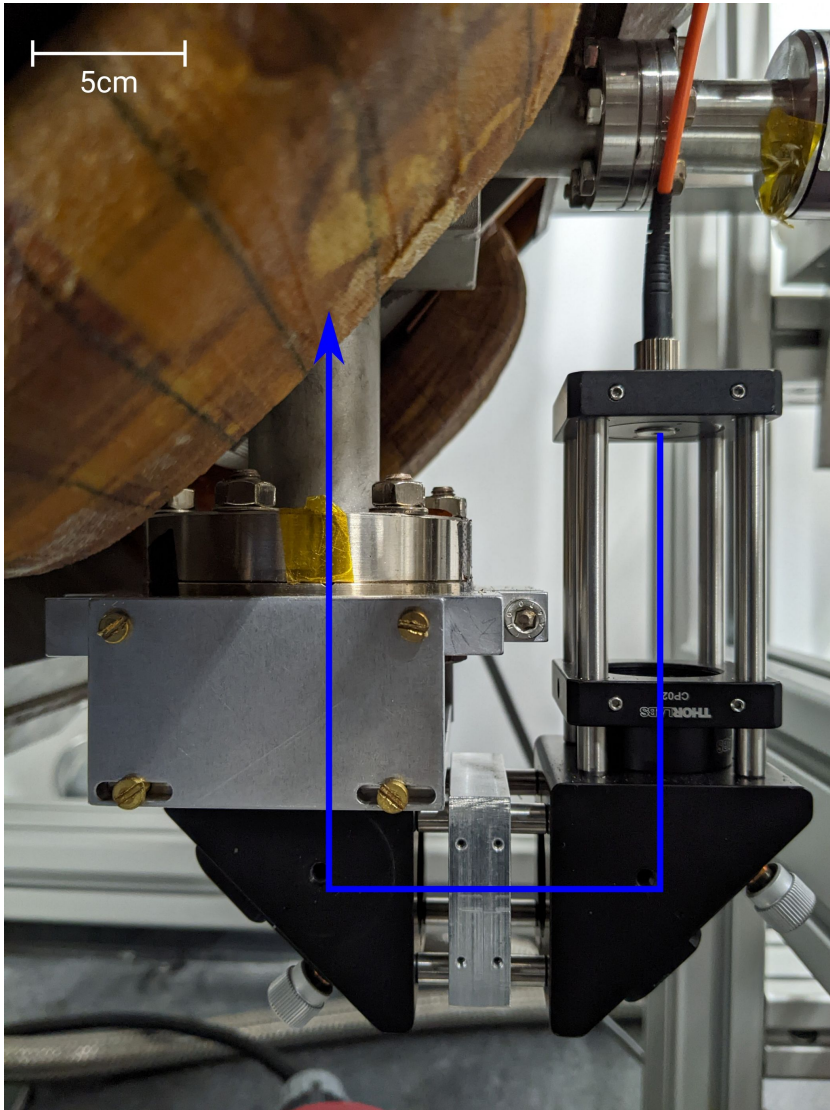


Figure 4.23: Mirror array for the decoupling of the laser beam mounted at the bottom window of the cryogenic test stand. In orange the fiber patch cable can be seen. The path of the laser is marked in blue.

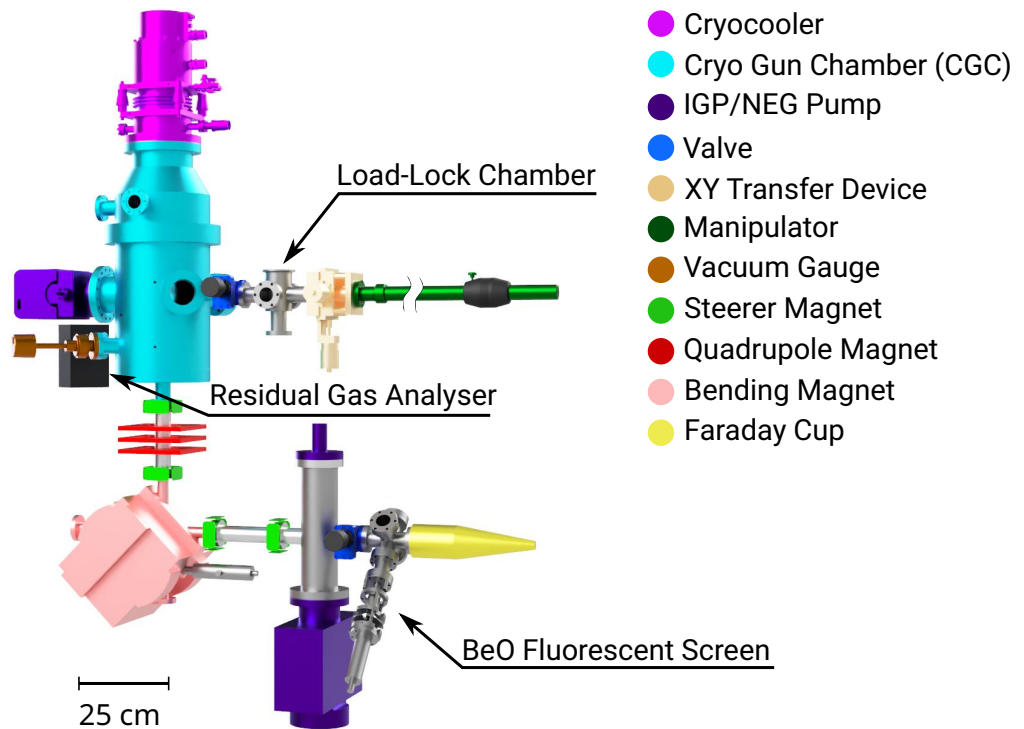


Figure 4.24: Dedicated test stand to measure a potential lifetime improvement of the cryo source. New cathodes activated at Photo-CATCH are inserted into the Load-Lock chamber and transferred to the cryo source via a manipulator and a XY transfer device. The electron beam leaves the source chamber at the bottom, gets focused by a quadrupole magnet triplet and deflected by 90° by an alpha bending magnet. A Faraday cup measures the current of the beam. A vacuum chamber equipped with an IGP and NEG pump sits between the cup and the alpha magnet, reducing the pressure increase created by the electrons hitting the cup. A retractable BeO fluorescent screen right before the cup allows observation of the beam position required for an alignment of the beam through the quadrupole triplet and multiple steerer magnets. A residual-gas analyzer is used to measure the effects of the cryo pump on the gas spectrum inside the source chamber. For better visibility the support frame is not shown in the picture.

As the electrons diverges after leaving the source a triplet of quadrupole magnets between source chamber and alpha magnet focuses the beam to prevent electron loss. One quadrupole magnet focuses the beam in one axis but defocuses in the other. With a set of two a focusing effect in both axes can be achieved, while a set of three allows the same focus strength in both axes. Due to limited laboratory space the same small magnets also used in the vertical beamline of Photo-CATCH are installed. To align the magnets, they are placed on a frame which can be moved in all three axes. For more information on the used quadrupoles and the alpha magnet one may be referred to [180].

When the electrons hit the Faraday cup they can increase the pressure in the cup and in connected components. To stop the pressure increase from reaching the source chamber a 400 l/s NEG and an 100 l/s IGP pump are placed between the cup and the alpha magnet attached to a small stainless-steel chamber, here referred to as the *pump chamber*. An Beryllium Oxide (BeO) fluorescence screen located right before the Faraday cup allows to check the alignment of the beam into the cup. Both can be sealed off from the rest of the test stand by a manual gate valve between screen and pump chamber.

A small chamber with 6 flanges one in every direction is attached to the puck insertion port on the aluminum chamber. It is used to dock the transport chamber and will be called load-lock chamber (LLC) in accordance to the equivalent chamber at Photo-CATCH. It features a quick CF-flange on top and two DN40 CF-windows. Other than the one at Photo-CATCH this LLC is not equipped with a turbo pump, but features a DN40 CF-flange on the bottom, to connect a separate mobile pumping cart, which is also used at Photo-CATCH to provide a pre-pressure for the CAC, AHCC and GC. The cart is equipped with a diaphragm pump, a turbo pump, a vacuum gauge, a needle valve for venting and a flexible connection hose. A residual-gas analyzer can be attached optionally but is currently directly connected to the CGC to measure the influence of the cryopump on the residual-gas spectrum. To transfer the puck from the LLC to the CGC a manipulator equipped with a transport fork is attached to the LLC. Between load-lock chamber and manipulator an XY transfer device³², here also referred to as XY-manipulator, is installed. It allows the linear manipulator to be moved up, down and sideways by ± 12.5 mm, which is essential to place the puck into the slot inside the electrode. To seal the LLC off from the CGC after transferring the puck, a second hand-operated gate valve is placed between those two chambers.

All chambers other than the CGC are made from stainless steel. All flanges are connected using annealed or unannealed silver-plated copper gaskets and silver-plated screws. The silver plating prevents the individual parts from baking together due to thermal expansion during bake-out. A rack using aluminum profiles³³ and in-house manufactured supports

³²McAllister Technical Services MC1000-1.1.5

³³KriTec GmbH aluminum Profile 8 80x40 light and accessories

was designed to provide a mounting platform for the chambers and other components. The test stand does not feature Helmholtz coils, so the influence of the earth's magnetic field needs to be compensated by the steerer magnets.

4.9 The Integration Into Photo-CATCH

A future integration of the cryo source into Photo-CATCH is foreseen allowing to measure additional beam parameters such as the beam shape, the emittance and the degree of polarization. As the cryo source is planned to be an extra option and the already existing gun chamber (GC) should not be replaced, some modifications on the chamber setup are required. An additional chamber called transfer chamber (TC) (not to be confused with the transport chamber) was designed and manufactured to allow an activated cathode to be transferred either to the gun chamber of the conventional source or the cryo source. A model of this transfer chamber is shown in Figure 4.25.

As space at Photo-CATCH is limited there is no room for an IGP and the transfer chamber is only equipped with an NEG and a vacuum gauge. On top either a z-translation like on the CAC and AHCC or a manipulator like on the transport chamber will be placed. An attached carousel allows storage and transfer of the pucks. On the bottom a flange is available for the residual-gas analyzer or a connection to the mobile pumping cart. In the first case the residual-gas spectrum of all three attached chamber can be measured by opening the valve to the corresponding chamber and closing the others. The manipulator and the XY transfer device currently used at the dedicated test stand can be reused. For a view on the carousel two windows are available. The transfer chamber will be placed between AHCC and CAC, all separated by valves. After activation the puck can be transferred either into the GC as usual or back into the transfer chamber where it is picked up by the manipulator and transported further into the CGC. Figure 4.26 shows the modified chamber setup of Photo-CATCH with the integration of the CGC and the transfer chamber. The CGC sits over the beamline and the electron beam needs to be bent by 90°. The alpha magnet currently used at the dedicated cryo test stand is well suited for this task. In contrast to the magnet used for bending the beam from the conventional gun the alpha magnet allows a horizontal beam to pass it, as the alpha chamber is open to all four directions. Therefore, the cryo and the conventional source can share the same beamline.

To study whether the beamline is suited for an operation of the cryo source or if modifications have to be made, a simulation was conducted using the software *elegant*³⁴ [181]. *Elegant* is developed and maintained by Argonne National Lab and uses a matrix

³⁴The name *elegant* is an acronym for ELEctron Generation ANd Tracking.

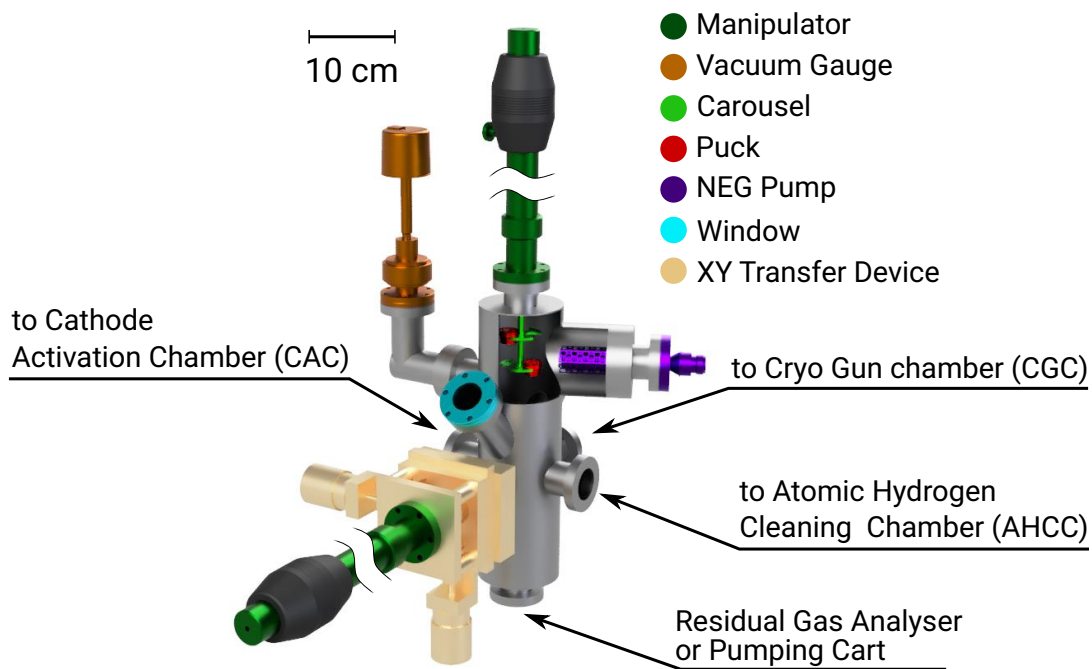


Figure 4.25: Model of the transfer chamber, which will be inserted between CAC and AHCC. It is necessary to allow a transfer of the activated cathode into the CGC as the conventional source should not be replaced. The XY transfer device and the manipulator currently used at the dedicated cryo source test stand can be reused. To store the cathode for handover from one manipulator to the other either a linear rotary device with a carousel can be used or the manipulator and carousel currently in the transport chamber can be reused. At to bottom a port for the mobile pumping cart or a RGA is available. The latter can be used to analyze the residual-gas spectrum in the CGC, AHCC and CAC by opening the corresponding valve.

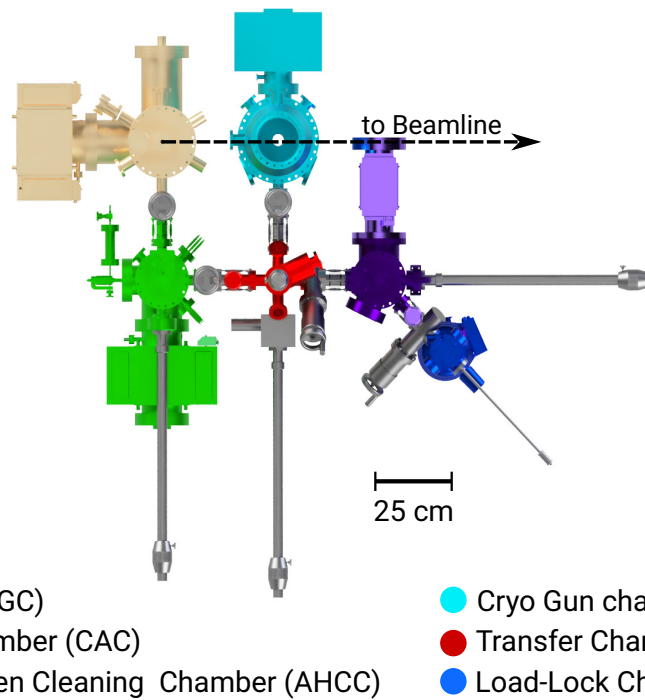


Figure 4.26: Top view of a rearrangement of the Photo-CATCH chambers for a future integration of the cryo source. The AHCC and LLC have to be moved to the right to give way for the transfer and cryo gun chamber. The GC and CAC do not have to be moved or modified.

formalism among others to describe and calculate different parameters of electron and other particle beams in accelerators. In addition elegant is capable of optimizing the beam control elements (in this case the magnets) in position and current for a given beam-parameter goal. The software requires two files, in the first part of the lattice file the used control elements are defined while in the last part these elements are combined to a sequence describing the beamline. In the command file a start particle bunch is defined and generated as well as the parameters for the optimization are characterized. The beamline of Photo-CATCH was modeled and a bunched beam was generated with elegant. The starting beam parameters were obtained with a CST simulation using a -30 kV potential. A bunched beam was simulated since elegant and a possible future use in accelerators requires an electron bunch. The optimization goal was to stay in the diameter of the beam tubes and the diagnostic elements. For this the beamline was split into four segments, each containing one quadrupole triplet. The optimization process was set to optimize the focusing right before the quadrupoles. Figure 4.27 shows the position spread envelope of the beam from the cryogenic source after optimization process, while the beam angle envelope is shown in Figure 4.28. The results of the simulations shows that the beam line can be used for an operation with both sources. The only necessary modification is a shift of the beamline to give way for the placement of the alpha magnet. Currently at the foreseen position of the alpha magnet a solenoid is located. As the space in the laboratory is limited a replacement of the solenoid with a narrower version may be a more feasible option. For more details on the conducted elegant simulation including the currents for the magnets found by the optimization algorithm one may consult [182].

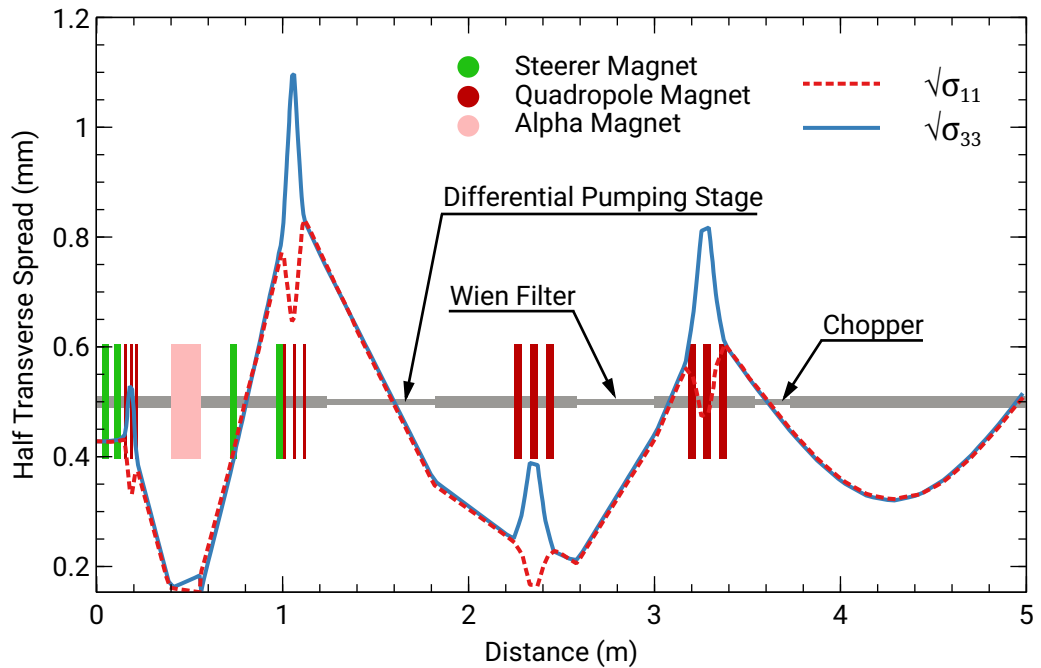


Figure 4.27: Half transverse spread of the bunch along the beamline according to simulations with elegant. Shown are the magnets included in the simulation. At the alpha magnet the vertical beamline becomes horizontal. Also marked are the differential pumping stage, the Wien filter and the chopper as they exhibit a smaller vacuum pipe diameter. $\sqrt{\sigma_{11}}$ and $\sqrt{\sigma_{33}}$ refer to the matrix elements describing the transverse position spread of the electrons. The graph has been interpolated linearly between the calculated values resulting in the displayed angular shape.

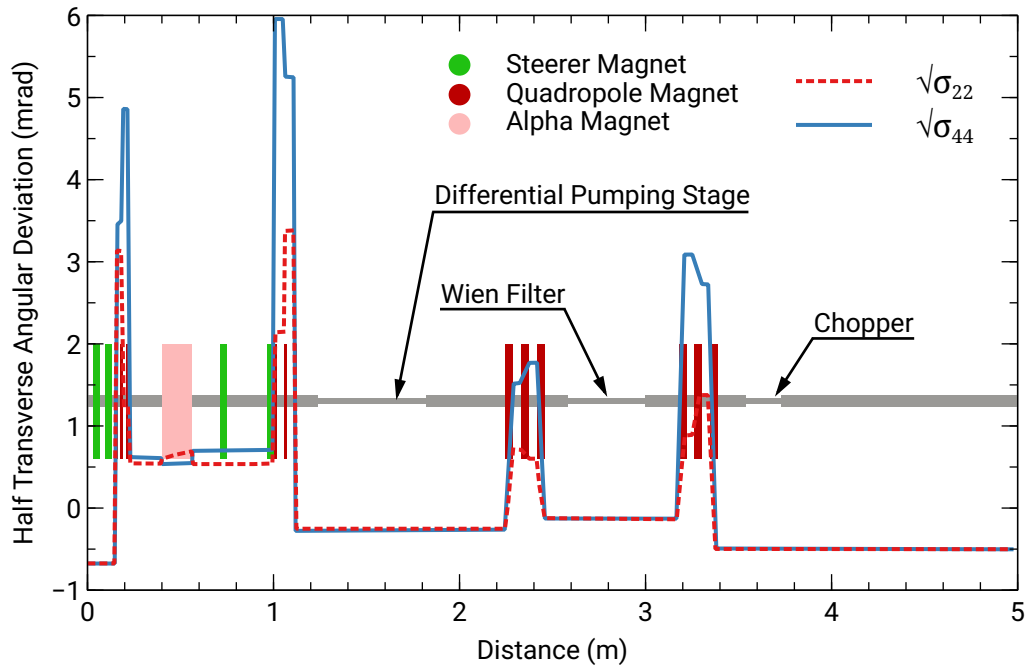


Figure 4.28: Half transverse angular deviation of the bunch along the beamline according to simulations with elegant. Shown are the magnets included in the simulation. At the alpha magnet the vertical beamline becomes horizontal. Also marked are the differential pumping stage, the Wien filter and the chopper as they exhibit a smaller vacuum pipe diameter. $\sqrt{\sigma_{22}}$ and $\sqrt{\sigma_{44}}$ refer to the matrix elements describing the transverse angular deviation of the electrons. The graph has been interpolated linearly between the calculated values resulting in the displayed angular shape.

5 Assembly and Commissioning

5.1 Cryo Gun Chamber Assembly

The following section describes the assembly process of the sub-volume and the cryo gun, which was conducted in a clean room to prevent contamination of the cleaned components.

In the first step the sub-volume walls were coated with activated charcoal. As the properties and efficiency of the cryopump are determined by the sorbent material the choice of charcoal is significant. A selection of four different charcoal materials have been characterized by Day in 2001, with *CHEMVIRON SCII* showing the best results [131]. But it is no longer available. *Aquacarb 207C SC 12x30* was recommended as an equivalent replacement [183]. This variant was not obtainable in Germany at the time of this work, either. Therefore, an available alternative¹ made from the same source material (coconut husk) with the same particle size and similar characteristics was chosen. The detailed properties are listed in Table 5.1. As bonding agent Thermoguss² was used, which is suited for XHV and withstands the bake-out temperature. The Thermoguss was applied to the inner walls of the sub-volume manually using a silicon brush, leaving a gap of around 1 cm to the top and the bottom to maintain the electrical isolation between electrode and anode. The charcoal was scattered on top and pressed slightly into the Thermoguss. After curing for a day excessive charcoal was removed and the uncoated parts cleaned. The result is shown in Figure 5.1. For future studies with alternative sorbent materials and bonding agents, four additional alumina walls are available.

The tip of the cryocooler features one screwed hole for mounting. To provide a larger mounting base a copper plate was screwed to it. Between both 0.1 mm indium foil³ was placed to increase thermal conductivity as well as friction to prevent the mounting plate from turning. For easy assembly the cryocooler was positioned on a rack and a small lifting platform was used to align the components of the sub-volume. This way the ceramic screws could be inserted straight without the risk of breaking. Additional indium foil

¹The charcoal was ordered from JaPeBi Contor GmbH.

²Thermoguss 3000 by Harold Patscheider GmbH

³99.99 % indium foil from Cryoandmore Budzylek GbR

Table 5.1: Properties of the activated charcoal used.

Property	Value
source material	coconut husk
particle size	12x30 mesh (1.68-0.60 mm)
bulk density	420-550 kg/m ³
ash content	≤ 3 %
hardness (ASTM 3802)	≥ 90 %

was placed between every connection to ensure good thermal conductivity. The h.v. cable was attached at the recess using one of the ceramic screws. One of the free temperature sensors was mounted to the sub-volume bottom using one of the anode screws. For better thermal conductivity vacuum grease⁴ was applied to the sensor. Figure 5.2 shows the h.v. cable and Figure 5.3 the anode with attached temperature sensor. The completely assembled sub-volume attached to the cryocooler can be seen in Figure 5.4. The heat shield was attached to the first stage of the cooler using the manufacturer provided screws while the h.v. cable was fed through one of the shields openings. This is shown in Figure 5.5.

The NEG modules mounted inside the lower part of the vacuum chamber need to be insulated from the chamber walls but connected to each other and the electrical feedthrough. Therefore, the modules were mounted with ceramic screws and washers and connected to each other using copper plates. The four modules are grouped in two pairs and mounted on opposing sides. In order to connect both pairs one longer copper plate was routed in an arc along the chamber wall to not block the space for the sub-volume. Figure 5.6 shows a view inside the chamber with mounted NEG modules, Figure 5.7 the connection of the modules to the feedthrough and Figure 5.8 a closer view onto the copper plate attached to one module.

The cryocooler and sub-volume were inserted into the top part of the vacuum chamber and the h.v. cable fed through one of the DN40 CF-flanges. For insulation of the high voltage, ceramic beads were threaded onto the cable and the tip connected to the electric feedthrough. Photo 5.9 shows the feedthrough with connected cable right before closing the flange.

In the last step the chamber was closed, transferred into the laboratory and mounted to the test stand rack. Figure 5.10 shows the completely assembled chamber.

⁴Apiezon N grease



Figure 5.1: Sub-volume walls coated with activated charcoal.

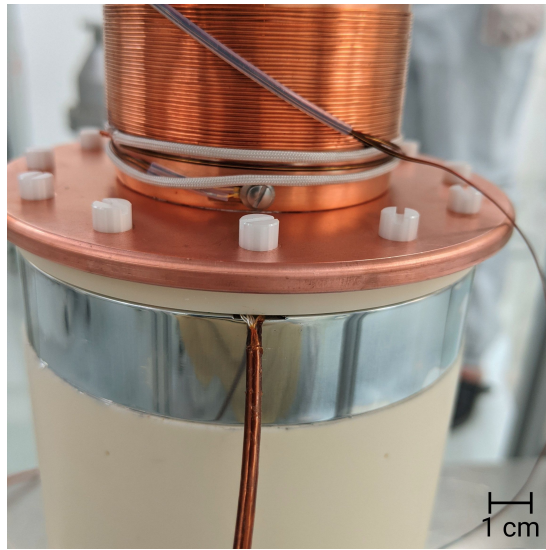


Figure 5.2: h.v. cable attached to the electrode of the sub-volume.

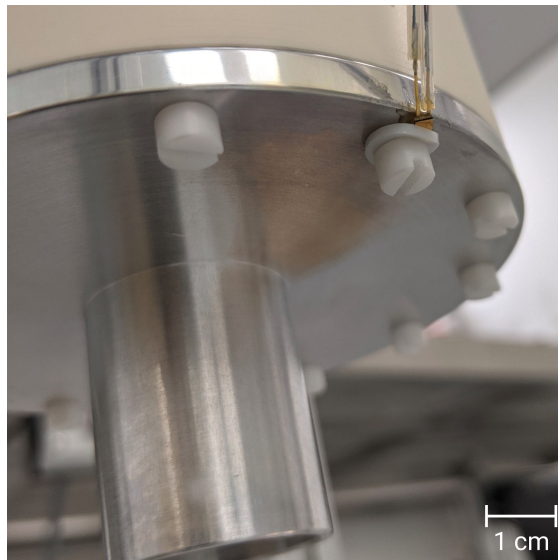


Figure 5.3: Temperature sensor attached to the bottom of the sub-volume held by a teflon washer and a ceramic screw. For better thermal conductance Apiezon[®] N grease is applied between sensor and sub-volume.



Figure 5.4: Complete sub-volume mounted to the tip of the cryocooler. On the left side of the volume the temperature sensor cable can be seen and on the right side the h.v. cable without ceramic beads.

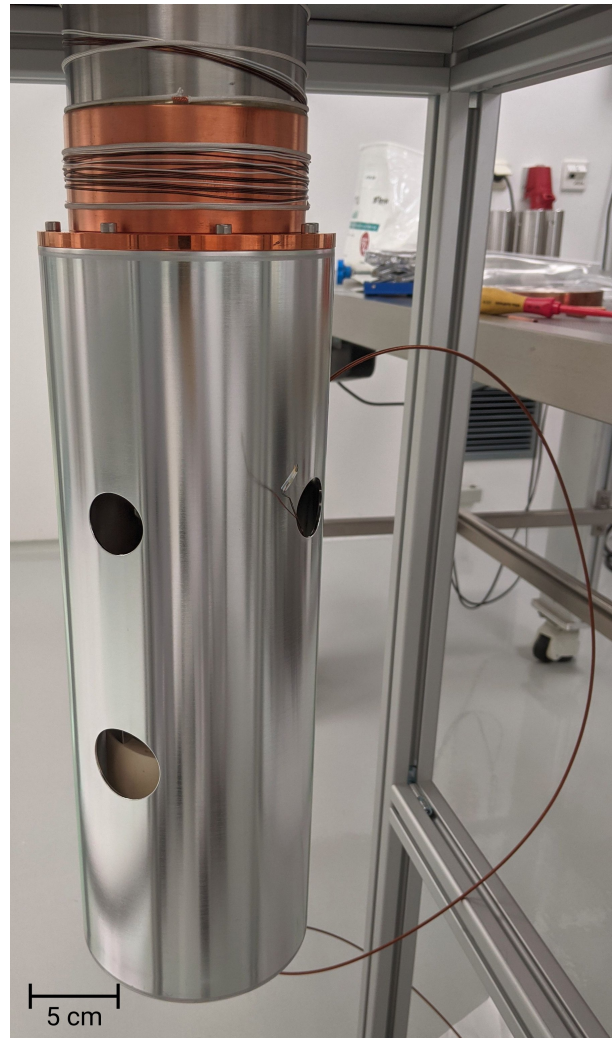


Figure 5.5: Cryocooler with mounted sub-volume and heat shield. The h.v. cable can be seen on the right side.

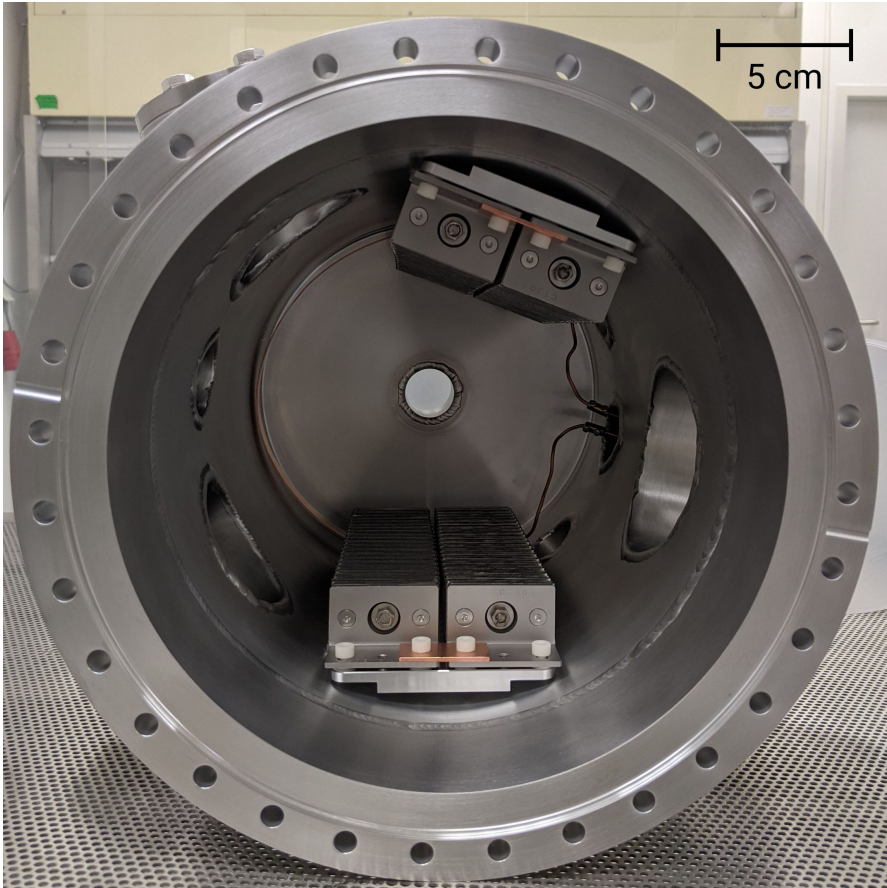


Figure 5.6: View into the vacuum chamber. On the chamber walls the mounted NEG modules can be seen. They are connected to each other through copper plates.

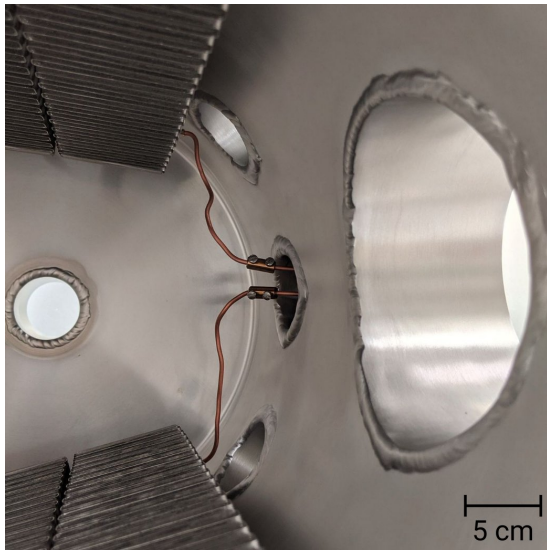


Figure 5.7: Connection of the NEG panels to the electric feedthrough.

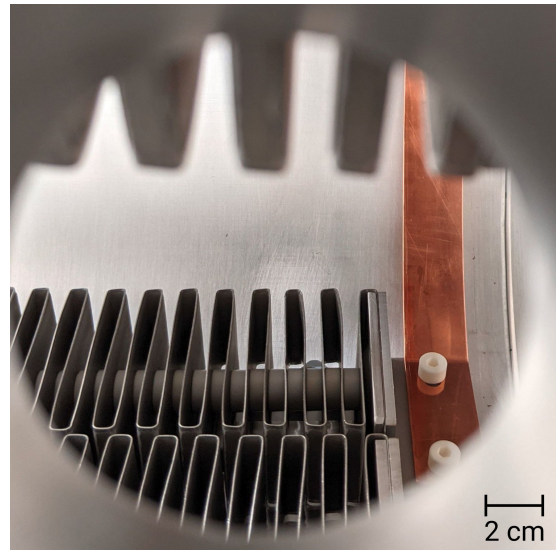


Figure 5.8: View onto the lower part of the NEG panels with copper band connection and ceramic screws.

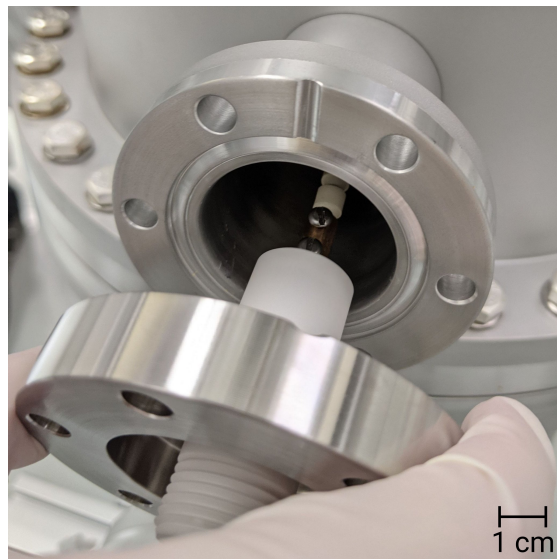


Figure 5.9: h.v. cable with ceramic beads attached to the h.v. feedthrough.

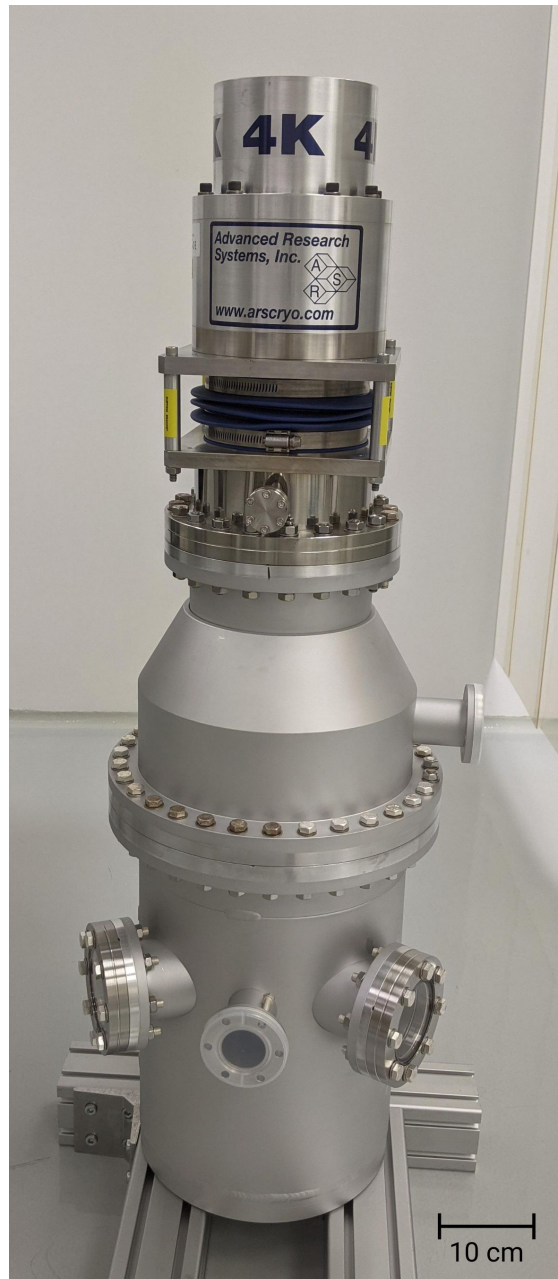


Figure 5.10: Completely assembled cryo gun chamber. At the top the tip of the cryocooler can be seen.

5.2 Transport Chamber Evaluation

As the transport chamber had never been tested for activated cathodes before, a measurement series was conducted to determine the level of NEA layer decay during transport from Photo-CATCH to the cryo test stand. Beforehand, the transport chamber was baked out at 200 °C for one week⁵ and mounted to the load-lock chamber of Photo-CATCH. A cathode was cleaned and activated as described in Section 2.3.3 with caesium and oxygen using the co-deposition activation scheme. A white LED was used to measure the photocurrent during activation to ensure that the cathode is illuminated even when the positioning of the carousel is slightly off. After the procedure was finished, the photocurrent with the white LED was noted and in addition the current was measured using a blue LED to better represent the blue laser used at the cryo source. The quantum efficiency cannot be calculated with the LEDs as the power impinging on the cathodes surface is unknown. Therefore, the QE was determined using the red laser (780 nm) of the activation chamber and with the blue (450 nm) laser used at the cryo source. To guide the blue laser beam to the activation chamber, the fiber was mounted to the decoupling and mirror array usually used for the red laser. As the optics were not designed for this wavelength the active power measurement included in the array could not be used. Hence, the power had to be determined using a hand-held power meter⁶ right before the window. Losses due to reflections on the window were neglected as only the QE ratios are of interest.

The activated cathode was transferred through the AHCC and the LLC to the transport chamber. The transfer usually took between 9 and 15 minutes, where the transfer into the transport chamber was usually faster than the way back as the placement of the puck in the carousel of the transport chamber is easier than the pick up with a manipulator. The pressure in the AHCC and LLC was in the mid 10^{-10} mbar and lower 10^{-8} mbar to high 10^{-9} mbar regime, respectively. The transport chamber was not detached from the LLC for this measurement series. To simulate a transport to the cryo test stand the cathode was stored in the transport chamber for some time and then transferred back to the activation chamber to measure QE and photocurrent again with all four light sources. Six measurements have been conducted, where in the first two the transfer through the LLC took longer as the puck got stuck. This directly translates to a reduced QE afterwards as shown in Table 5.2. As the pressure in the LLC is higher than in the other chambers the transfer through the LLC is the critical moment to sustain a high QE and should be done as fast as possible. For the third activation the transfer could be conducted quicker and

⁵The temperature of the gate valve was set to 180°C.

⁶Thorlabs[®] PM100D with S121C power sensor

over 50% red laser QE could be sustained after a storing time of 60 min. The QE using the blue laser increased after the transport, which can be explained by either a better placement of the puck carousel or a rotation of the puck during transfer. The NEA layer is not applied uniformly in the activation process and the QE varies over the surface. When the puck is rotated during the transfer the laser may hit a spot with a higher QE, which can result in a QE ratio above 100 %.

When closed, the transport chamber can sustain a pressure in the mid 10^{-11} mbar regime, but when exposed to the vacuum in the LLC the pressure rises significantly. After closing it again it takes some time to drop to the former level. Figure 5.11 shows the development of the pressure inside the transport chamber during and after the transfer process of measurement 2. To reduce the pressure rise the LLC was baked at 95°C for 20 h before the last three measurements, but no significant pressure reduction in the LLC could be achieved. The bake-out temperature was limited by the fact that the attached transport chamber would be baked too. This could lead to a reduced pumping speed of the NEG and would require a complete reactivation of the pump. The following measurement however, showed an increase of the red laser QE ratio to over 98 % while the blue laser QE ratio is again over 100 %. This could also originate from a faster transfer. Nevertheless, the bake-out was maintained for the following measurements and have been conducted before all transports to the cryo test stand.

For the last two measurements the storing time was increased to 20 h. The actual detaching, carrying and mounting to the cryo test stand can be done in a matter of minutes, but it takes around 5 h for the LLC at the cryo stand to reach a pressure in the 10^{-8} mbar regime, which is essential before opening the transport chamber. As the cleaning, cool down and activation takes a few hours, too, the total transfer may require two work days and the cathode has to be stored in the transport chamber over night. This was simulated with a storing time of 20 h. The results show that over 67 % of the red laser and over 71 % of the blue laser QE could be sustained. Thus, a storage over night is possible without losing too much QE for a lifetime measurement.

Summarized, the results demonstrate that the transport chamber is well suited for a transfer of activated cathode from Photo-CATCH to the cryo test stand. The transport chamber may also be an option for polarized guns at accelerators. For a red laser, some decay of the NEA layer has to be expected. But as an advantage, the activation can be performed outside the accelerator hall during operation and then transferred into the gun faster than cleaning and reactivation of the old cathode. By doing so, down times of the accelerator operation could be reduced, provided the pumpe-down time of the load-lock chamber is fast enough. This may also be an option at accelerators where space is limited.

Table 5.2: Photocurrents of the cathode measured with a white ($I_{n,w}$) and a blue LED ($I_{n,b}$), as well as the quantum efficiency with a 780 nm red ($\eta_{n,780}$) and a 450 nm blue laser ($\eta_{n,450}$) before ($n=0$) and after ($n=1$) the transfer of the cathode into the transport chamber, storing for some time and transfer back. Between measurement 3 and 4 the LLC was baked out at 95 °C for 20 h. All values were measured using an anode bias voltage of 100 V.

Activation Storing Time (h)	before bake-out			after bake-out		
	1	2	3	4	5	6
1	1	1	1	1	20	20
$I_{0,w}$ (nA)	629(5)	375(5)	424(5)	433(5)	479(5)	498(5)
$I_{1,w}$ (nA)	153(5)	204(5)	298(5)	339(5)	302(5)	197(5)
$I_{1,w}/I_{0,w}$ (%)	24(1)	54(2)	70(2)	78(2)	63(2)	39(1)
$I_{0,b}$ (nA)	199(5)	105(5)	121(5)	126(5)	141(5)	139(5)
$I_{1,b}$ (nA)	74(5)	90(5)	119(5)	126(5)	115(5)	74(5)
$I_{1,b}/I_{0,b}$ (%)	37(7)	86(7)	99(6)	100(6)	82(6)	82(6)
$\eta_{0,780}$ (%)	7.2(2)	4.9(2)	4.6(2)	4.2(2)	4.8(2)	5.9(2)
$\eta_{1,780}$ (%)	0.2(2)	0.2(2)	2.4(2)	4.1(2)	3.2(2)	4.1(2)
$\eta_{1,780}/\eta_{0,780}$ (%)	4(3)	5(4)	52(5)	98(6)	67.2(5)	69(5)
$\eta_{0,450}$ (%)	8.1(2)	5.5(2)	5.5(2)	5.3(2)	6.1(2)	7.7(2)
$\eta_{1,450}$ (%)	3.5(2)	3.9(2)	5.9(2)	6.0(2)	6.12(2)	5.5(2)
$\eta_{1,450}/\eta_{0,450}$ (%)	44(3)	71(4)	108(5)	113(6)	99(5)	71(4)

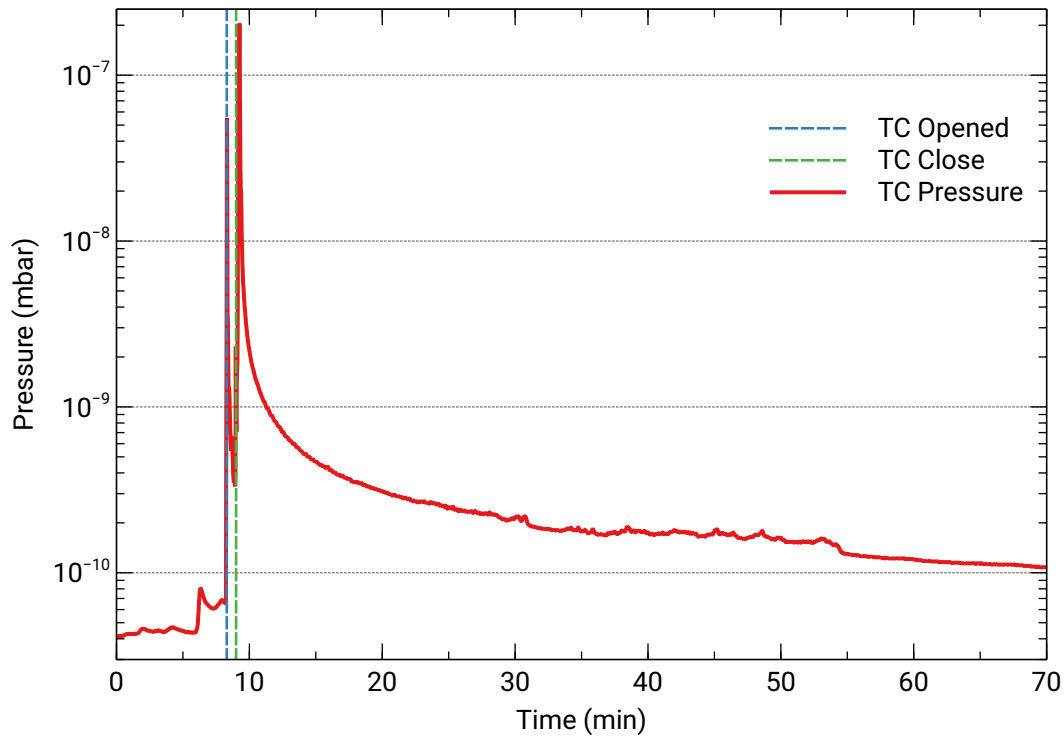


Figure 5.11: Pressure development inside the transport chamber during and after transfer of the cathode into the chamber. The moments the chamber was opened/closed are marked in blue/green. The pressure spikes seen at the time the valve was opened and closed are created by the high sensitivity of the gauge to vibrations. This also results in a slight pressure increase before the opening due to the vibrations generated by the transfer through the AHCC and LLC.

5.3 Commissioning

5.3.1 Bake-Out and NEG Activation

The complex and nested structure of the CGC results in an increased pump-down and bake-out time. After one week of pumping a pressure of around $7 \cdot 10^{-6}$ mbar was reached and the bake-out process started. To prevent a rapid pressure rise, the temperature was increased slowly over a period of two weeks until 120 °C for all aluminum and other sensitive parts and 140 °C for the remaining components were reached. Two weeks later the falling pressure curve reached a stable state and the temperature was lowered again. At 70 °C the NEG was activated with 22 A current for roughly 3 h, which results in a temperature of nearly 280 °C, according to the manufacturer. The temperature rise of the heat shield and the vacuum chamber was lower than anticipated and a pulsed activation procedure was not required (see Section 4.5). Using the data from Figure 4.18 an activation efficiency of 50 - 70 % can be anticipated. After room temperature was reached a final pressure of $4 - 5 \cdot 10^{-11}$ was measured, which is comparable with the pressure inside the Photo-CATCH gun chamber. Based on this observation as well as the calculations and simulations done for the pressure ratio between sub-volume and outer chamber, a vacuum around the cathode of up to two magnitudes better than at Photo-CATCH is expected, resulting in a lifetime increase of up to two orders of magnitude.

5.3.2 Laser Commissioning and Properties

Alignment

For the emission of electrons the laser described in Section 4.7 needs to be aligned onto the cathode surface. The main challenge here is the limited view due to the closed sub-volume and shield. This is an inherent problem in the design, that cannot be changed as the closed volume is a key feature of the source to enhance the cathodes lifetime. To solve this problem the alignment was done before closing the system. A pre-alignment was done before attaching the load-lock chamber by adjusting the mirrors of the decoupling array (see Figure 4.23 for the array) until the beam was visible with the unaided eye in the inside of the sub-volume through the flange where the load-lock chamber will be connected. Figure 5.12 shows the view into the chamber including the visible laser spot on the ceiling. For a more precise alignment a photo diode was mounted centered into a puck using an adapter ring and inserted into the sub-volume via a transport fork attached to a rod. Then the mirrors were readjusted until the maximum diode current was found. To determine the fraction of the laser power reaching the cathode, the laser was also focused onto the diode outside the chamber. By comparing both diode currents the total

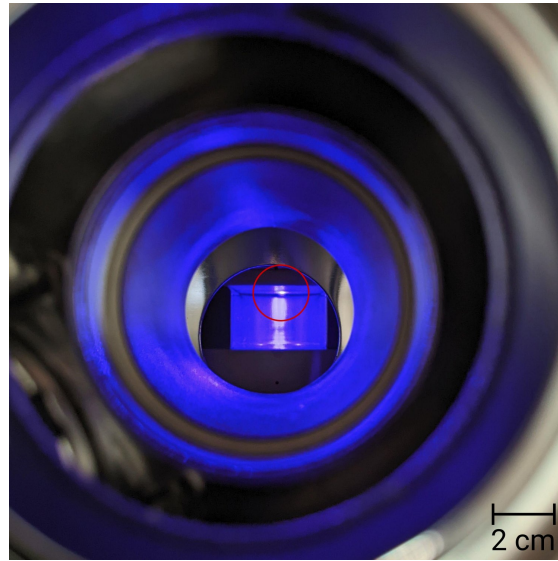


Figure 5.12: View into the cryo gun chamber and the sub-volume, seen from the location of the LLC. The laser spot is visible at the ceiling of the sub-volume and marked in red.

power loss could be calculated to 43.2(1) % of which 12(1) % originate from reflections on the window, which was measured before installation. The remaining loss may result from the adapter ring in which the diode was placed. As the surface of the diode was set back a few millimeters from the rings and the pucks surface, a not perfectly straight beam may hit the inner side of the ring. Another cause may be a slight tilting of the diode produced during mounting into the ring.

For the bake-out procedure the mirror array needs to be removed. In order to assess the reproducibility of the alignment after bake-out the array was removed and reattached. Only a minimal misalignment afterwards was observed, hence, a reproducible alignment was expected. However, this method is very sensitive against unintentional adjustment of the mirrors, which would require an opening of the system and a complete repetition of the time consuming bake-out procedure. Therefore, great caution is advised when handling the mirror array.

Unfortunately, the bake-out process had a greater effect on the alignment than anticipated and the beam did not hit the cathode afterwards. To readjust the laser without the need to open the CGC, it was sealed off of the load-lock chamber and the manipulator was replaced with a window. After pump-down of the LLC the valve was opened presenting a view into

Table 5.3: Beam waist radius of the laser spot at the distance of the cathodes surface (80 cm) as well as 2 cm before and after. The waist is shown for the two axis u and v and the mean of both.

Distance z (cm)	$\omega_u(z)$ (μm)	$\omega_v(z)$ (μm)	$\omega_{mean}(z)$ (μm)
78	399(1)	394(1)	397(1)
80	403(1)	335(1)	369(1)
82	402(1)	341(1)	371(1)

the sub-volume, allowing the pre-alignment procedure to be redone. A realignment with a photo diode was not possible, as it would require the CGC to be opened up again. A not perfectly centered beam was taken into consideration in the simulations and should not prevent a successful lifetime measurement.

Beam Profile

The profile of the laser beam cannot be directly observed at the location of the cathode as the sensor does not fit into the sub-volume. Therefore, the beam was coupled out of the fiber on the laser table and focused on the distances at which the cathodes surface will be in the CGC. The profile was measured using a scanning-slit beam profiler⁷ at the cathodes location as well as 2 cm before and after to take a slight measurement error of the distance between cathode and fiber coupling into account. The profiles are shown in Figure 5.13 while the beam waists are summarized in Table 5.3. The measured waists are in good accordance with the cutoff radius of 0.5 mm used in the CST beam simulations. The profiles do not follow a perfect Gauss curve and multiple modes are visible, originating from the use of a multi-mode fiber. This is not a requirement for a lifetime comparison, but for the use at an accelerator, where beam quality matters, an upgraded laser setup using a single mode fiber is advised.

Stability

As the laser system did not feature an active power stabilization, the power fluctuations over 112 h were measured to assess the effect on the precision of the lifetime measurement. The temperature stabilization was set to 21 °C and the diode current to 84 mA, which is the manufacture recommended operation point and well above the laser threshold.

⁷Dataray® BeamMap2 – XYZ $\Theta\Phi$ Scanning Slit Beam Profiler

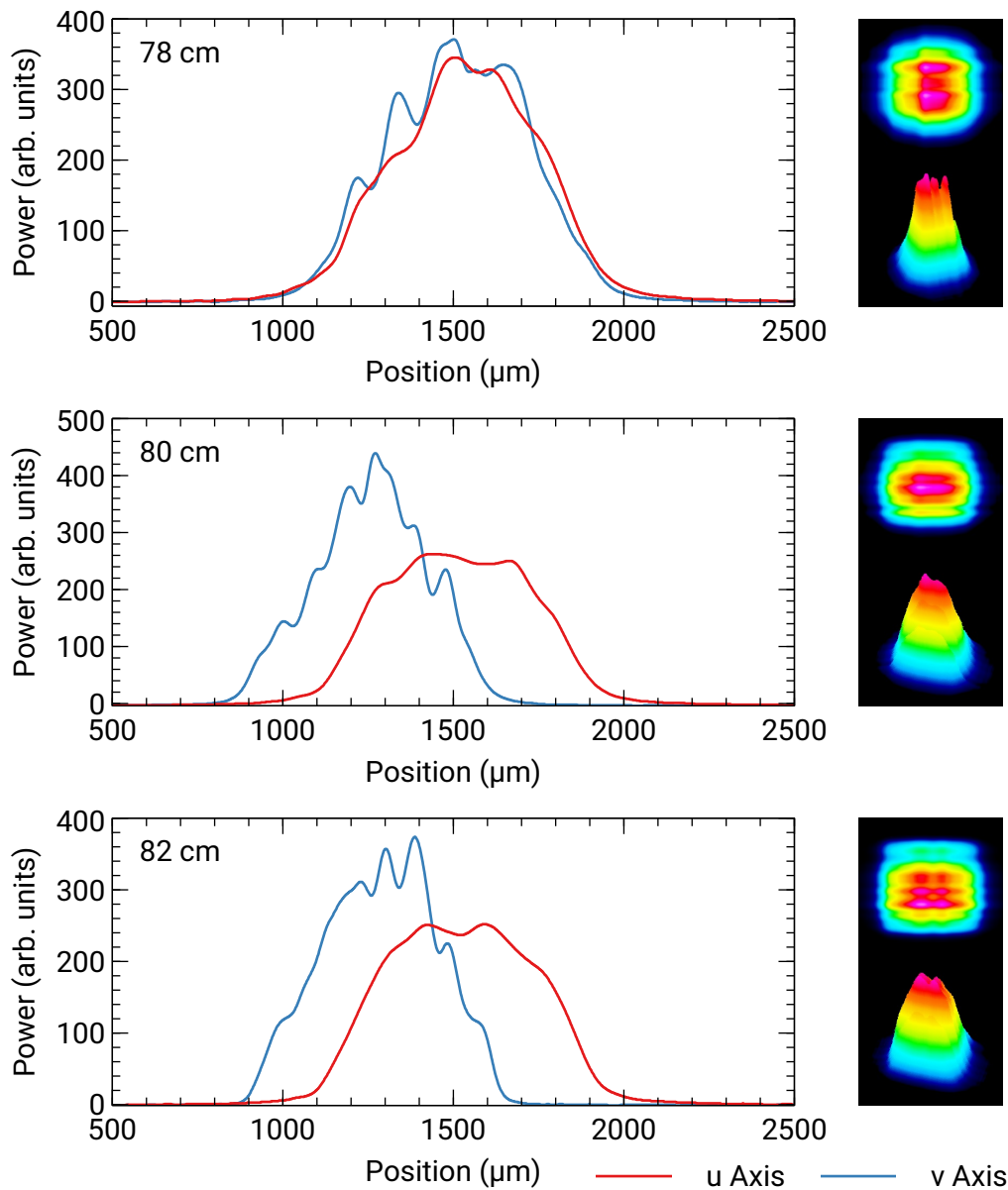


Figure 5.13: Laser beam profiles at the distances of the cathodes surface (80 cm) as well as 2 cm before and after. As only the shape of the beam is assessed here, the power distribution on the left is shown in arb. units. The shift between u and y axis profile for the measurement at 80 cm and 82 cm originate from a not centered beam on the sensor. The right side shows the power distribution in a color representation in 2D and 3D.

Table 5.4: Absolute and relative stability of the laser power over 112 h.

mean laser power	2.016 mW
min. power	2.002 mW
max. power	2.030 mW
error	$\pm 14 \mu\text{W}$
percentage error	0.694%

The power was measured after the fiber using a Thorlabs[®] PM100D with a S121C power sensor. Beforehand, the laser was warmed up for roughly 1 h and the power reduced to 2 mW via the neutral density filter. The result is shown in Figure 5.14. Two fluctuations can be observed, one fast oscillation with small amplitude and a slower drift with higher amplitude. The fast oscillation has a fluctuation in the range of minutes and an amplitude in the range of single-digit μW . While the drift happens on a scale of hours with an amplitude of double-digit μW . For a lifetime measurement over multiple hours or days the slower drift presents the dominating effect, due to its higher amplitude. Therefore, the fast oscillation will not be considered separately and only the spread of the total drift will be used for the calculation of an absolute and percentage error of $\pm 14 \mu\text{W}$ and 0.694%, respectively. The results are summarized in Table 5.4. An additional oscillation, visible in the first few hours, indicates that a longer warm-up phase is needed.

5.3.3 Cryocooler Commissioning

The temperature of the sub-volume with active cooling was assessed with measurements in two setups. A first evaluation was done in a simple DN160 CF vacuum chamber attached to the pumping cart providing a pressure in the lower 10^{-8} mbar regime. The cryocooler features three sensors, of which one is integrated into the tip and two are freely placeable. The temperature controller used however, only features two inputs, so the temperature curve cannot be recorded simultaneously for all three sensors. As the exit-pipe was not ready at that time one of the sensors was attached to the bottom of the ceramic chamber walls in order to assess the temperature of the sub-volume. This setup allowed the other sensor to be attached to a puck, which was inserted into the sub-volume to evaluate the thermal conductivity between the electrode and a puck loosely placed into the opening. Figure 5.15 shows the temperature curve for the internal sensor and the sub-volume bottom. After the minimal temperature was reached (after 5 h to 6 h), the inputs were switched to the pucks sensor. The cryocooler tip reached a minimal temperature of

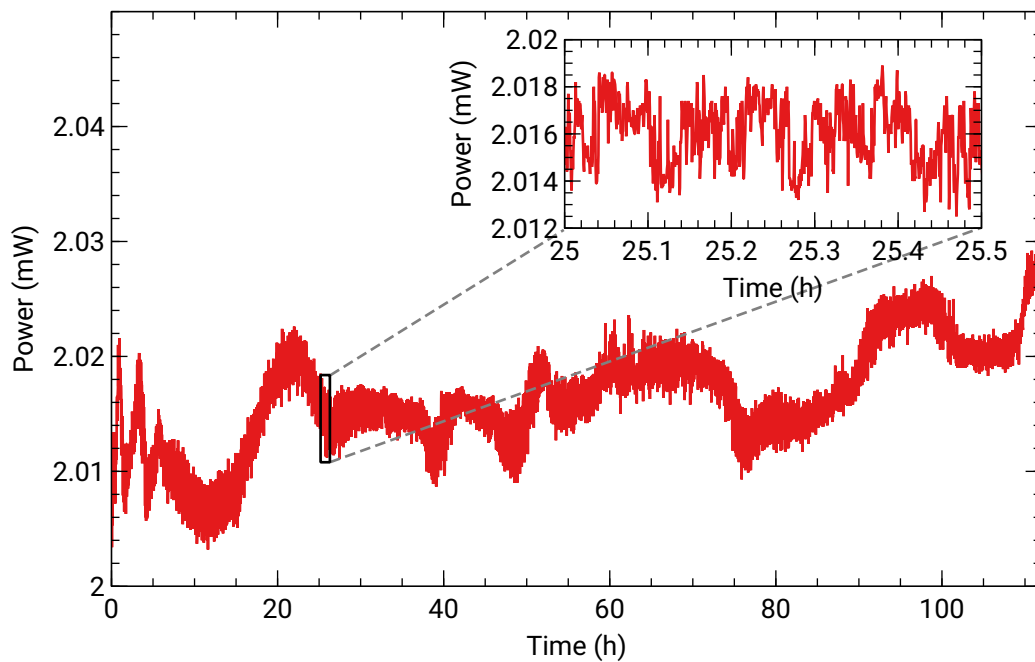


Figure 5.14: Fluctuations of the laser power over a time period of 112 h. A slow drift and a high-frequency oscillation with lower amplitude is observable. For the measurement of a lifetime over multiple hours or days, the slow drift presents the dominating effect due to its higher amplitude. The laser was warmed up for roughly 1 h before the measurement was started. The additional oscillation in the first hours indicate that a longer warm-up phase is needed.

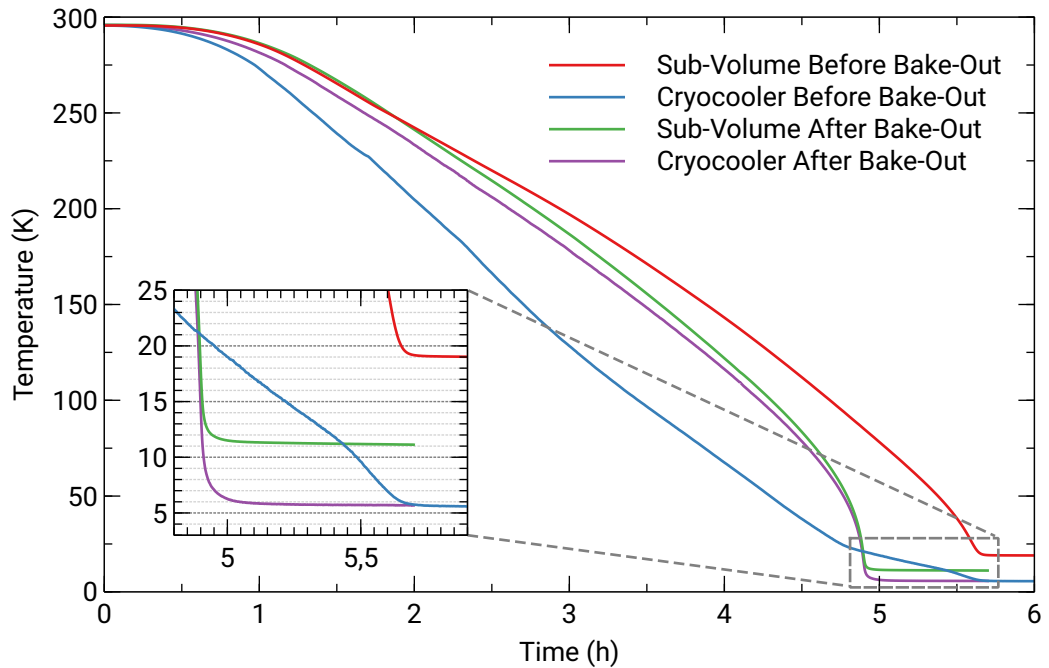


Figure 5.15: Temperature curves of the sub-volume and the cryocooler in a DN160 CF vacuum chamber before and after bake-out at 120 °C for 30 h. The final achieved temperatures before bake-out are 5.9(1) K for the cryocooler, 19.0(1) K for the sub-volume and 19.0(1) K for the puck. With baking of the complete system the temperature could be reduced to 5.7(1) K at the cryocooler and 11.1(1) K at the sub-volume bottom.

5.9(1) K, the sub-volume of 19.0(1) K and the puck of 19.0(1) K. As the laser setup was not finished at the time the influence of the heat introduced to the puck by the laser could not be measured. However, the fact that the puck reaches the same temperature as the sub-volume indicate a sufficient thermal conductivity between puck and electrode to effectively compensate this heat load. The emissivity of the involved surfaces present a significant factor for the cooling process. For the materials involved the emissivity ranges from 0.06 for mechanical polished aluminum to 0.4 for aluminum oxide (see Table 4.8), whereas the emissivity of 0.96 for water is significant higher [172]. Therefore, the removal of water films on the components is of utmost importance to optimize the temperature. The measurement was repeated after a 30 h bake-out at 120 °C. This reduced the minimal

temperature of the cryocooler to 5.7(1) K and of the chamber bottom to 11.1(1) K. The temperature curves are shown in Figure 5.15. It can be noticed that the temperature difference between cooler and sub-volume during cooldown was reduced after bake-out. This indicates an improved thermal conductivity between the components, which may originate from a softening of the indium foil during bake-out⁸. The foil now better fills the gaps between the individual parts resulting in an increased contact area.

The temperature curves were measured again with the final setup at the cryogenic test stand after the bake-out procedure described in Section 5.3.1. The results are shown in Figure 5.16. This time the free sensor was placed at the bottom of the exit-pipe as described in Section 5.1. It reached a temperature of 21.3(1) K. The required duration increased by roughly 1 hour, due to the additional mass of the anode. The temperature of the activated charcoal could not be measured directly, but a temperature well below 21.3 K can be anticipated, which is sufficient for an effective pumping of hydrogen. During the test stand setup the helium hoses were removed and reattached a few times, which introduces a small amount of air into the cooling cycle each time. A slightly lower temperature may be achievable by refilling the system with new helium. Furthermore, a fairly significant dependency of the reached temperature from the room temperature was observed in later cooling processes. By lowering the settings of the air conditioning system present in the laboratory even lower sub-volume temperature may be achievable.

This setup allowed the evaluation of the lasers influence onto the temperature of the complete system. Figure 5.17 shows the temperature curve before and after switching on the laser at 12.1(1) mW⁹. No laser-induced temperature rise was observed. This matches the expected behavior, as the laser of 12 mW only plays a minor part in the total heat load.

Residual-Gas Analysis

The effect of a cooled sub-volume on pressure and residual-gas composition was measured using a residual-gas analyzer¹⁰. The spectrum was recorded with and without cooling and is shown in Figure 5.18. As the internal photomultiplier was used to enhance the signal no statement on the absolute pressures can be made. The spectrum shows a reduction of the heavier gases to some degree, but a slight increase for hydrogen. The RGA is mounted outside the heat shield. Therefore, the spectrum does not give an insight into the behavior inside the sub-volume, where a much larger effect is expected especially for hydrogen, as

⁸The melting point of indium with 156.6 °C is above the bake-out temperature.

⁹The power was measured before the window.

¹⁰Exorr inc. XT100(M)

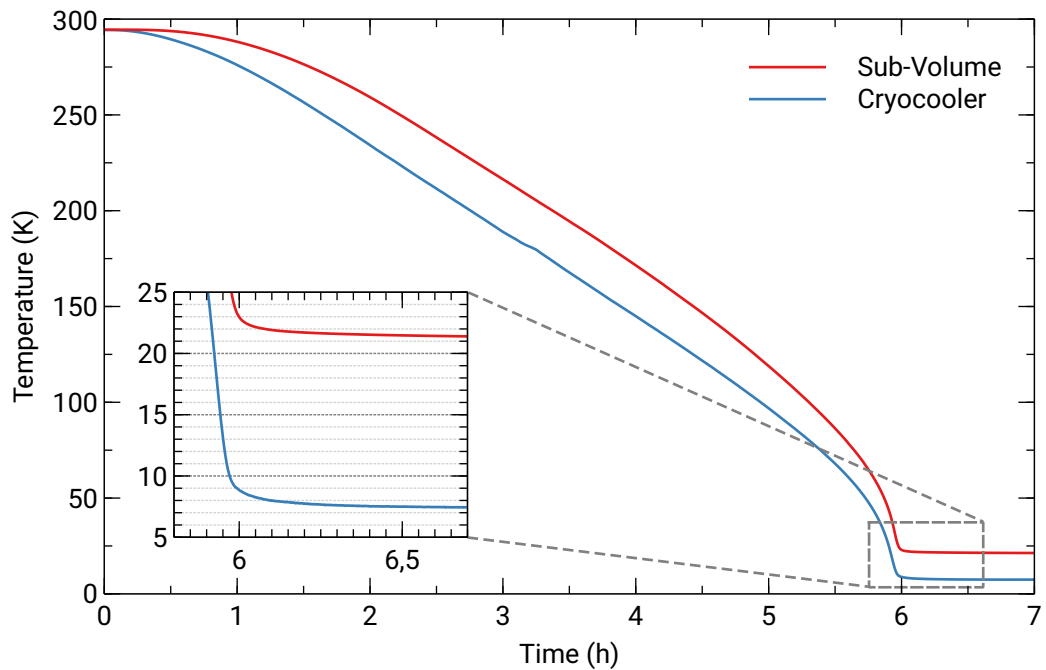


Figure 5.16: Temperature curve of the cryocooler and the sub-volume for the final setup at the cryo test stand. The sensor for the sub-volume was placed at the bottom of the exit-pipe component as described in Section 5.1. A minimal temperatures of 8.0(1) K and 21.3(1) K could be achieved for the cryocooler and the sub-volume, respectively.

it is only captured by the charcoal. When in operation the analyzer creates some heat, that raises the temperature of its surroundings including the heat shield, which may falsify the measurement. As the data were recorded after the high-voltage conditioning (see Section 5.3.4) an unusual high amount of helium, still remaining in the system, can be noticed. As helium cannot be captured by the cryo pump, krypton should be evaluated as an alternative in future conditionings.

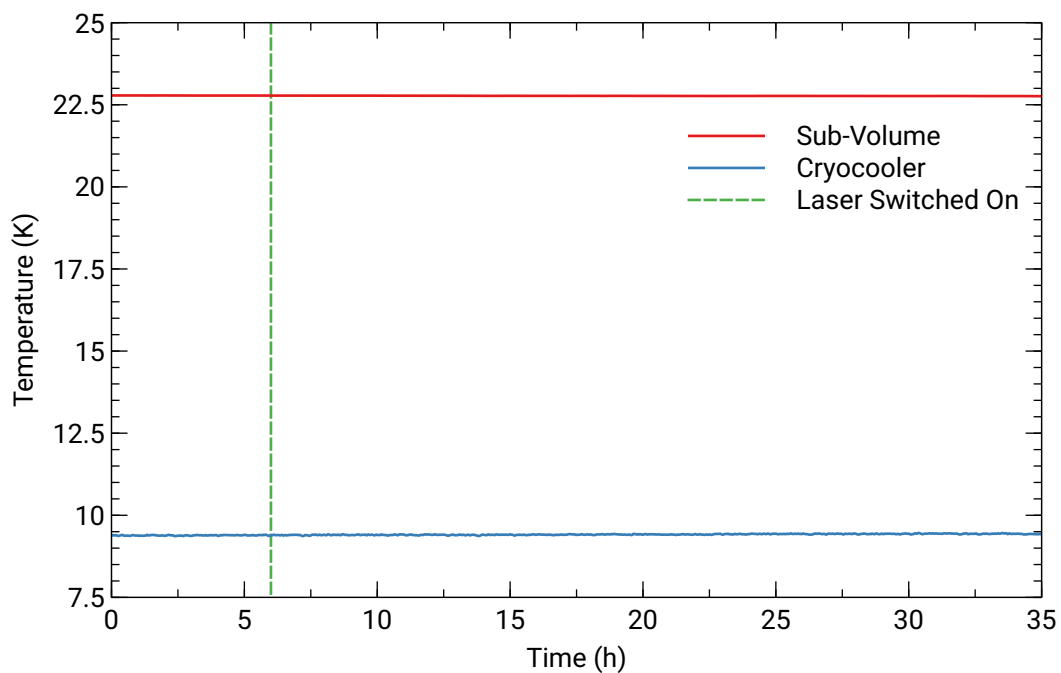


Figure 5.17: Temperature curve of the cryocooler and the sub-volume before and after switching on the laser at 12.1(1) mW (measured before the window). The time the laser was switched on is marked in green. The higher base temperature compared to the measurements above originates from a higher room temperature in the laboratory at the day of the measurement.

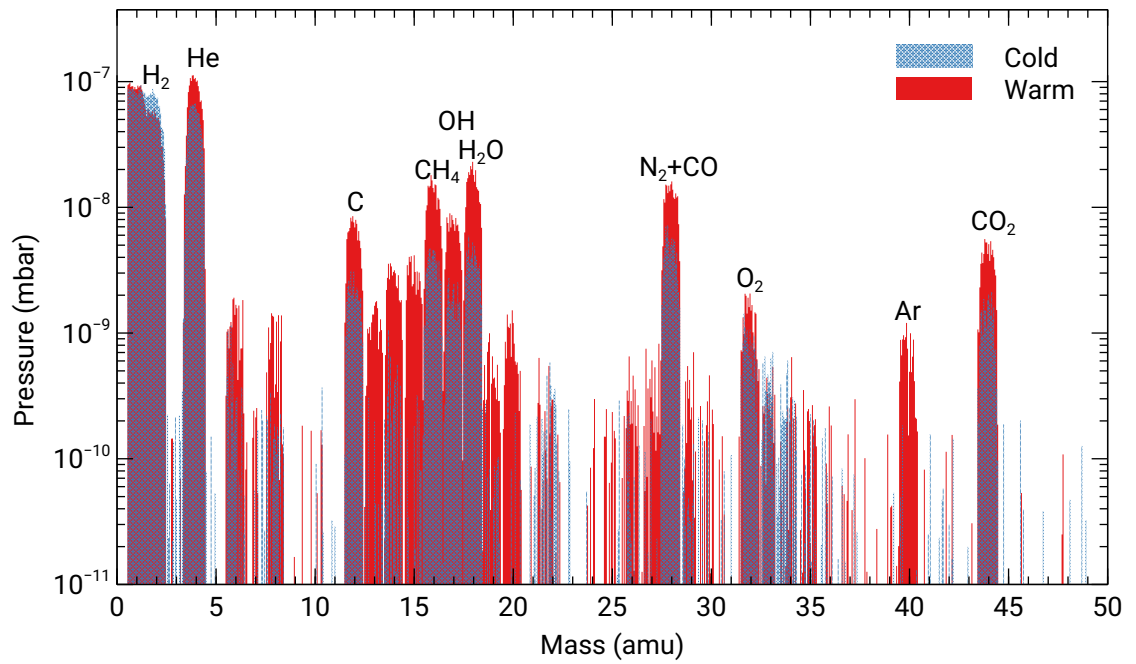


Figure 5.18: Spectrum of the residual gas before and after cooldown. Only a small reduction in pressure of the lifetime relevant gases can be seen. As the RGA is mounted outside the heatshield, where a much lower cryopumping effect is expected this spectrum does not show the behavior inside the sub-volume.

5.3.4 Lifetime Measurement

High-Voltage Conditioning

To achieve the highest possible electrode potential a conditioning had to be conducted as described in Section 4.3.2. This was first done without any additional gas for several days. The potential was increased slowly until a field emission excess current was measured by the high-voltage supply¹¹. The increase was paused until field emission extinguishes and the voltage was increased further. This procedure was repeated until no more decrease in current was observed. After finishing the conditioning a stable operation at -8 kV to -9 kV could be reached. To further increase the potential a conditioning with helium was conducted. For this purpose, the IGPs were turned off and the helium was introduced into the system through a needle valve to a pressure in the 10^{-5} mbar regime. Then the potential was further increased slowly in the same way as before. This led to a maximum stable voltage of -12 kV at room temperature. With cooling the potential could be increased to -14 kV. Thus, a positive effect of cooling on the field emission behavior of aluminum could be demonstrated, but not as high as for copper, where an increase of up to 50 % at 30 K was observed (see Section 4.3.2). However, according to the CST simulations, an operation at -12 kV should be possible.

Cathode Preparation

For the the lifetime measurement the cathode was activated in the same way as for the test of the transport chamber. The LLC at Photo-CATCH was baked out at 95 °C for around 20 h and the cathode heat cleaned for 30 - 40 min. A 2 - 3 h cooldown phase followed until the cathode reached room temperature again. After the co-Deposition activation procedure, the quantum efficiency was measured and the cathode directly transferred into the transport chamber. The LLC was vented and the transport chamber detached from Photo-CATCH and mounted to the LLC of the cryo test stand. A mobile pumping cart was used to pump down the LLC, while it was baked out at 95 °C for around 14 h. Afterwards it took 3 - 4 h until the LLC reached room temperature and a pressure in the mid 10^{-8} mbar regime. The transfer of the puck into the sub-volume could be conducted reliably and reproducibly after some trial transfers with an unactivated cathode.

¹¹Heinzinger electronic GmbH PNC 60000-3 neg

Lifetime Measurement

After the cathode was activated and placed inside the sub-volume, the electrode potential was ramped up to -12 kV and the laser shutter opened. As the magnets were not adjusted yet their currents were ramped-up slowly while the fluorescent screen was monitored. In multiple activation runs and many magnet current combinations no beam could be observed on the screen. However, when increasing the laser power to $\sim 200 \mu\text{W}$ and above, a significant pressure increase (up to the 10^{-9} mbar regime) could be observed. The increase only occurs with an activated cathode in place and a high voltage applied. From this one can conclude a proper laser adjustment and a cathode emitting electrons. As the strength of the pressure increase was independent from the magnets configuration the origin of the beam loss could not be determined. It may be possible that, in contradiction to what was predicted by the simulations, the beam is not able to leave the sub-volume. If the beam exits the sub-volume, there are four steerer magnets with two axis each, three quadrupole magnets and an alpha magnet before the beam can be observed at the fluorescence screen or the Faraday cup. This creates many degrees of freedom especially as the magnets can be tuned continuously with positive or negative currents, making an alignment of the beam complex and time consuming.

Therefore, the chamber was opened up again and a second BeO fluorescent screen right before the alpha magnet was introduced. It features a hole in the middle, wide enough to let the laser beam pass. This way a reduction of the degrees of freedom could be achieved. In addition the anode (exit-pipe) was connected to a feedthrough to monitor whether the beam gets lost inside the sub-volume. The same cable type as for the high voltage was used including the same ceramic beads. The procedures for pump down and bake-out were repeated in the same manner as before. As the target increases the distance between laser out coupling and cathode, it was focused on the new distance. After the second bake-out a lower pressure than the first time could be reached, which was below the sensor's measurement range of down to $1 \cdot 10^{-11}$ mbar. A reconditioning of the electrode with helium was required resulting in the same voltages for stable operation as before.

In the following measurements only the current of the first and second steerer magnets were scanned while the newly installed screen was monitored. But again no beam could be observed. To evaluate if the beam gets lost inside the sub-volume the anode was connected to the readout electronics and the measurement repeated. With a high laser power in the mW regime a current of 1 - 1.5 nA could be measured when opening the shutter. However, this is magnitudes below what is expected with the set laser power. Assuming a quantum efficiency of 1% survived the transport and a laser power of 1 mW reaching the cathode a photocurrent in the μA regime is expected. The measured current did not increase when raising the laser power further, also the results could not be reproduced in the following

runs, where no current could be measured. This results indicate, that the beam is able to leave the sub-volume and only a fraction of the electrons could be measured at the anode in the first run. Hence, the beam must be lost somewhere between the heat shield and the fluorescent screen. A loss inside the shield is geometrically almost impossible. If the beam is straight enough to exit the sub-volume it should also be able to pass the larger opening of the shield.

To exclude the possibility of an external magnetic field created by pumps, wires or other electronics, which could disrupt the beam, the magnetic field strength around the chamber was measured using a magnetometer¹². But no field strength above the earth's magnetic field of roughly $20 \mu\text{T}$ for the horizontal component could be observed. According to the CST simulations the earth's magnetic field results in a beam shift of $1.9(1) \text{ mm}$ at the first steerer. To exclude the shift as the cause of the beam loss, the chamber was wrapped in Mu-metal. This nickel-iron soft ferromagnetic alloy exhibits an exceptionally high permeability providing a low reluctance path for magnetic flux. It can be used to shield against static or slowly varying magnetic fields like the earth's magnetic field. The measurements were repeated but delivered the same results.

Another conducted approach to determine the origin of the beam loss was to reproduce the method the QE is measured in the Photo-CATCH activation chamber. A bias voltage from 100 V to 500 V was applied to the anode instead of the high voltage to the electrode. With an field gradient this low the electrons should not gain enough energy to exit the sub-volume but be drawn towards the anode. However, no current could be measured, also no pressure increase could be observed without the high voltage ,even with a laser power of several mW. This hints at the fact, that the pressure increase is created by the accelerated electron beam hitting a chamber wall and not by the release of electrons alone. However, if electrons are emitted a current should be measurable at the anode in this setup.

As a last attempt an estimation of the lifetime increase due to the cooling of the sub-volume was intended by comparing the time the pressure increase is measurable at room and cryogenic temperature. The laser was set to a power of roughly $720 \mu\text{W}$ (measured before the window) resulting in a pressure increase to the 10^{-10} mbar regime, at room temperature. After several hours the pressure fell to a level, where it could not be distinguished from the base pressure any more. At cryogenic temperature only a minimal pressure rise in the lower 10^{-11} mbar regime could be observed, which fell in a matter of minutes to an indistinguishable level. This demonstrates the high pumping speed of the cryopump but prevents a useful lifetime comparison based on the pressure rise. Even with the highest possible laser power of 12 mW (before the window) no significant higher

¹²Projekt Elektronik Mess- und Regelungstechnik GmbH FM210 Teslameter

pressure raise could be achieved. This suggests that the electron beam does not leave the sub-volume and the pressure rise created by ESD, get pumped inside the sub-volume before reaching the outside and the vacuum gauge. This result is contrary to the previous observation which suggested the opposite. Therefore, no reliable statement about where the beam loss happens can be made, yet.

It can be concluded that electrons are emitted as the pressure increase is only observable with an activated cathode and a negative high-voltage electrode potential, but the origin of the loss remains to be determined. Due to the time consuming preparation process after opening the chamber no further modification for additional investigations could be conducted in the time scope of this work.

6 Summary and Outlook

A new approach in increasing the operational lifetime of GaAs photocathodes has been developed and first test experiments have been carried out within this work. In particular, the concept of a cryogenic sub-volume to enhance the vacuum conditions locally around the cathode has matured. The multiple challenges that come with such a closed volume have been worked out and a design was found which is compatible with the cathode activation system that is already in place at Photo-CATCH. Suitable materials were chosen, that meet all given requirements on thermal conduction, XHV compatibility and electrical insulation.

The electric field of the gun was simulated using CST studio for potentials ranging from -5 kV to -30 kV to assess the risk of field emission that come with the small sub-volume. A maximal field gradient of 11.1(1) MV/m was calculated for -30 kV. The resulting electron beam has been simulated for beam currents from 10 μ A to 1 mA and electrode potentials from -12 kV to -30 kV. The results showed that an operation with all tested potential is possible. Occurring beam shifts can be corrected by steerer magnets and the electron spread focused by quadrupole magnets along the beamline. The effect of a not perfectly centered laser spot and the influence of the earth's magnetic field on the beam have been studied. Both presented no beam shift that cannot be compensated by steerer magnets.

The heat load onto the sub-volume has been estimated for different heat sources and summarized to a total heat load below 0.5 W. The chosen cryocooler exhibits a cooling power of around 1 W and is thus sufficient to reach the temperatures required for a cryopumping effect. The results have been verified by measurements demonstrating a temperature at the rear end of the sub-volume of 21.3(1) K, which meet the criteria for an effective capturing of hydrogen.

A vacuum chamber to house the cryo source has been designed, featuring a split geometry to ensure an easy mounting and setup process. The expected pressure reduction due to cryopumping has been calculated as well as simulated, resulting in a pressure inside the sub-volume of up to two magnitudes lower compared to the outside chamber. To provide the necessary pre-vacuum a simulation was run confirming the sufficient pumping speed of the foreseen NEG and IGP pumps.

To conduct first lifetime comparison measurements a dedicated test stand was developed, featuring a Faraday cup, several magnets for beam transport, a load-lock chamber to transfer activated cathodes into the cryo gun and a residual-gas analyzer. Preparations for a future integration into the test stand Photo-CATCH, which features additional diagnostic instruments have been made including the design and manufacturing of a transfer chamber allowing the operation of both, the present conventional and the new cryo gun. As the cryo gun is foreseen to be located in front of the conventional along the beamline, simulations have been conducted evaluating necessary modifications. The results demonstrate that an operation of both sources is possible with the current beamline, solely a shift to give way for the connection of the cryo source is needed.

The complete test stand has been assembled including a simple laser setup using a 450 nm diode laser, which can provide a laser power of up to 12 mW. Due to the complex nested structure of the gun the bake-out process took over one month but resulted in a final pressure in the 10^{-12} mbar regime, which outperforms the simulation predictions.

A transport chamber, original designed to transfer hydrogen cleaned cathodes to the spin-polarized electron source (SPIn) at the S-DALINAC, has been tested for the transfer of activated cathodes from Photo-CATCH to the cryo test stand. The decay of the NEA layer when stored inside the chamber for some time have been evaluated in 6 measurements. The results showed that for 20 h of storing up to 100 % for a blue laser (450 nm) and 98 % for a red (780 nm) laser of the former QE could be preserved, demonstrating the suitability of the chamber for activated cathodes.

The properties of the laser have been determined by measuring the power stability over time and the beam profile at the distance of the cathode. A beam waist radius between $335(1) \mu\text{m}$ and $403(1) \mu\text{m}$ were measured in good accordance with the cutoff length of $500 \mu\text{m}$ used for the electron beam simulations. For the calculation of the cathodes lifetime an error of $\pm 14 \mu\text{W}$ caused by laser power fluctuations has to be taken into account.

The process of cathode activation, transfer to the cryo test stand and placing the puck inside the gun could be conducted reliably and reproducibly, both at room and cryogenic temperature. After a conditioning with helium a stable electrode potential of -12 kV could be achieved at room temperature, which can be raised to -14 kV by cooling the electrode. This presents an increase of the field emission limit by 16.6 % due to cryogenic cooling of aluminum. The achieved potentials are at variance with the expectations from simulations.

Multiple runs have been conducted, trying to measure the lifetime of the cathode. It was demonstrated, that electrons are emitted but no beam could be observed and no statement about the lifetime could be made. Despite multiple approaches including an upgrade

of the test stand the origin for the electron loss could not be determined. Experimental findings are contradictory, and the necessarily closed and nested design of the gun makes diagnosing the problem complex. Despite no experimental result was achieved so far, verifying a lifetime increasing effect, significant steps towards a cryogenic electron gun have been made in this work. For multiple relevant factors like pressure, the temperature, the transport of activated cathodes and the laser alignment the suitability for a cryogenic source were demonstrated. The built preliminary test stand as well as the cryogenic source's integration into Photo-CATCH present a solid base for further investigations.

To carry on this approach in the future, first the origin of the beam loss has to be isolated and eliminated. A step-by-step set up of the gun is advisable. Meaning to test the gun with a reduced design, starting with only the electrode without sub-volume and heat shield. This gives an inside if the problem occurs in the sub-volume or along the beamline. If a beam can be extracted this way the following steps would be to add the inner chamber walls without activated charcoal, continuing until the component responsible for the loss is identified. This undertaking presents a time-consuming process, since the chamber needs to be opened up and closed multiple times, which requires a bake-out each time. Two options are available to reduce this time, either a modification of the current test stand or an integration into Photo-Catch. In the first case an additional pump at the end of the beamline would reduce the pump-down time as well as the bake-out duration. Even more time may be saved by introducing a gate valve at the gun chambers exit. This way only the chamber needs to be baked. To simplify the alignment of the laser, a retractable 45° mirror, similar to the fluorescence screen could be installed between gun and load-lock chamber, allowing an alignment without the removal of the LLC or the manipulator.

When integrated into Photo-Catch the gun chamber would be sealed off from the beamline with a valve, also resulting in a faster bake-out. An additional time-saving advantage of this option is the elimination of the over night transfer of the cathode to the cryo test stand, allowing more frequent measurement runs. At Photo-CATCH the laser-alignment problem increases as the foreseen transfer chamber to which the GC will be attached is not as easily removable as the LLC at the cryo test stand. Therefore, a retractable mirror would be even more beneficial. In both scenarios some further automations can be implemented to speed up the measuring process like the high-voltage ramping or the scanning of the magnet currents. Installing a ceiling mounted lifting support like a crane would benefit both options and ease the opening of the chamber.

Looking further ahead, the properties of different sorbent materials can be compared to find the most suitable one. Due to the closed design, other aspects than those for conventional cryopumps may play a role. Thus, additional research may be required.

Furthermore, alternative electrode designs can be examined to increase the achievable potential. With an upgraded laser system, allowing a scanning of the frequency, the wavelength dependent QE and polarization measurement of Figure 4.21 can be conducted at cryogenic temperatures. This allows a comparison of theory and experiment. For the active operation at the S-SALINAC or future new accelerators requiring high beam currents a larger version of the gun is required to provide electrons with higher energy.

A Appendix

A.1 Technical Drawings

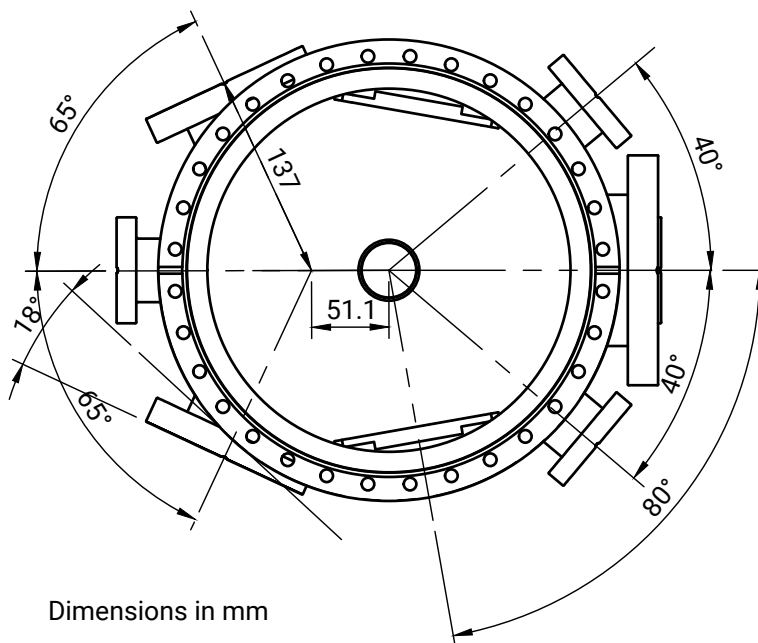


Figure A.1: Technical drawing of the lower part of the aluminum vacuum chamber in top view.

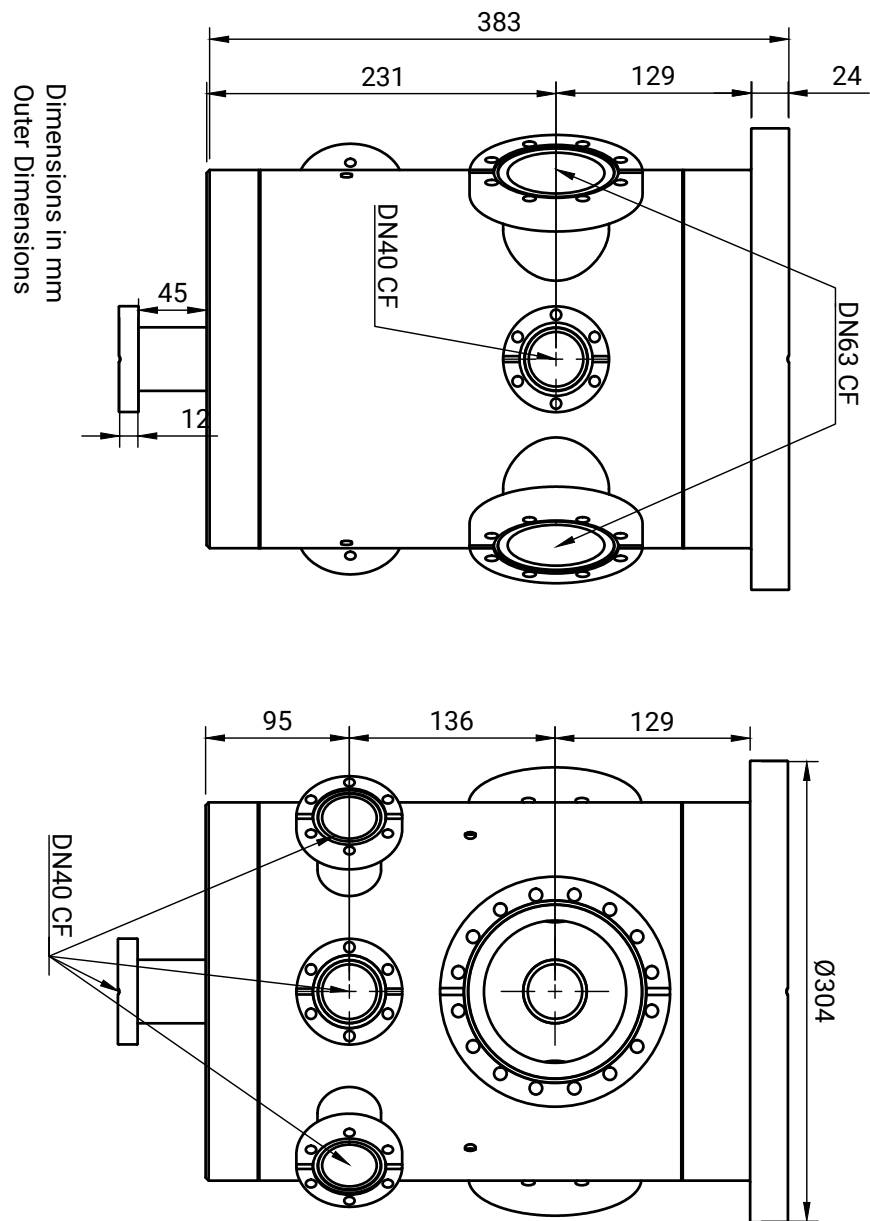


Figure A.2: Technical drawing of the lower part of the aluminum vacuum chamber in side view.

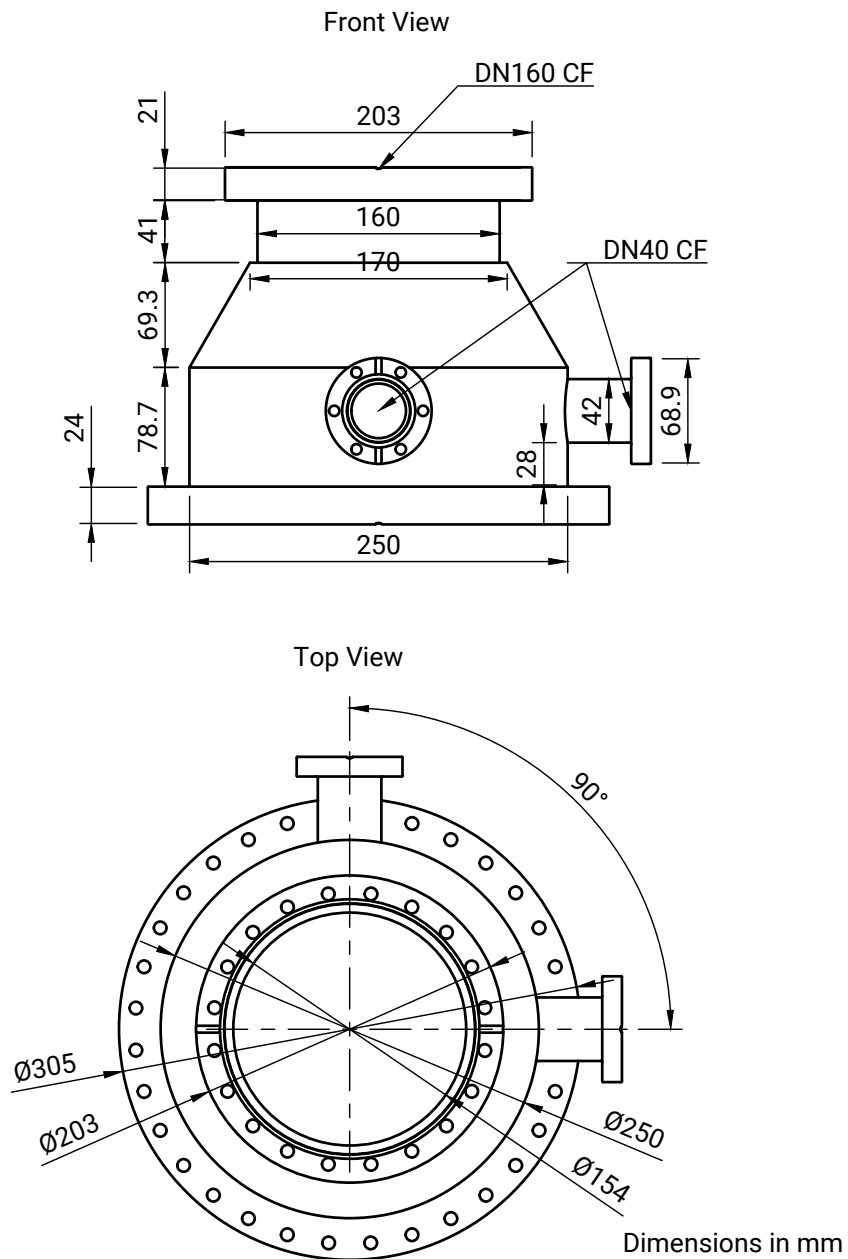
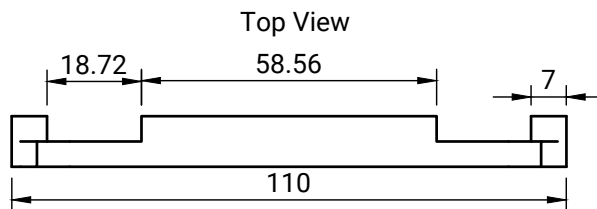
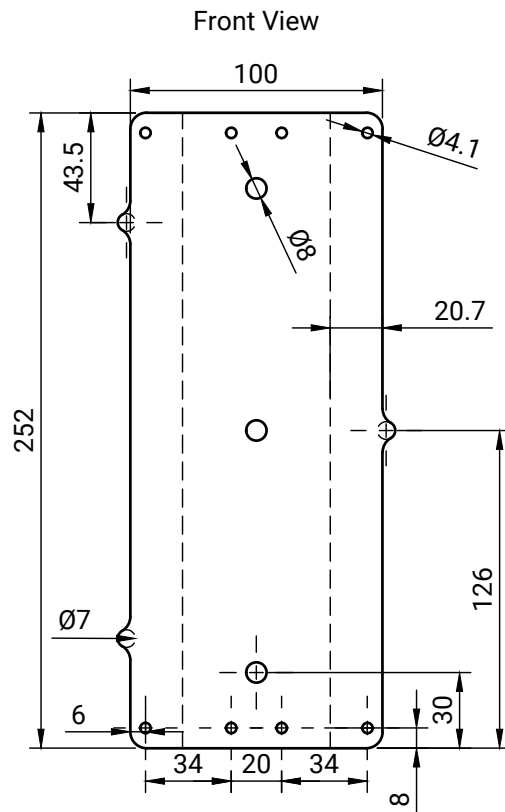
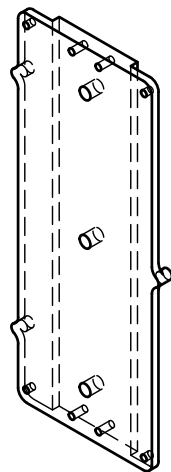


Figure A.3: Technical drawing of the upper part of the aluminum vacuum chamber in side and top view.



Dimensions in mm

Figure A.4: Technical drawing of the NEG mounting plate inside the aluminum vacuum chamber.

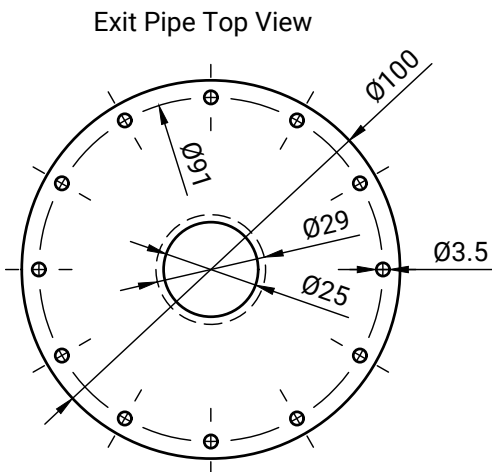
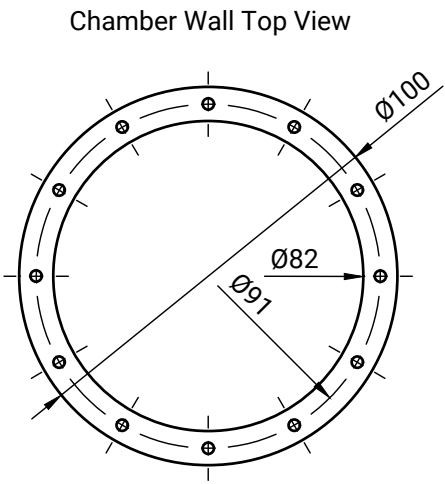
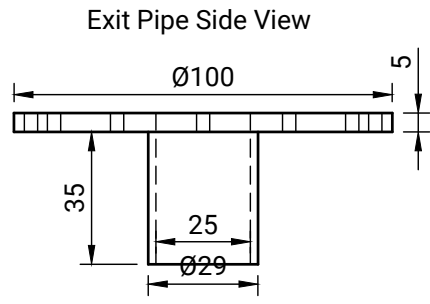
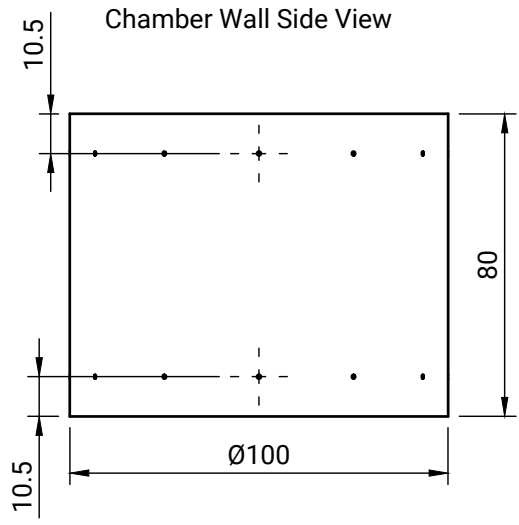
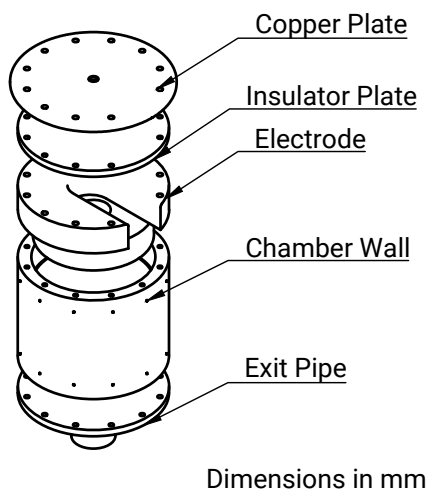


Figure A.5: Technical drawing of the cryogenic sub volume.

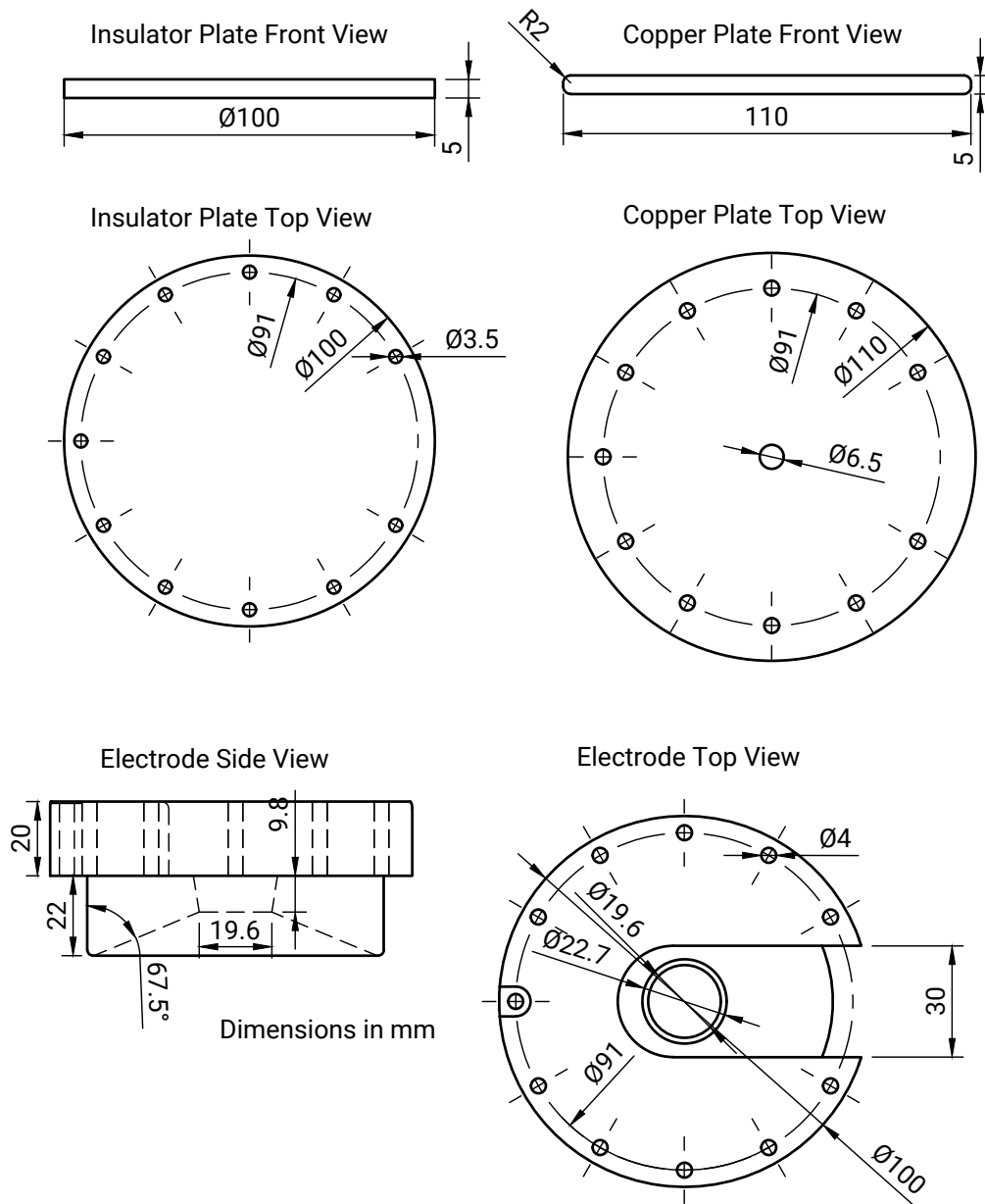


Figure A.6: Technical drawing of the cryogenic sub volume.

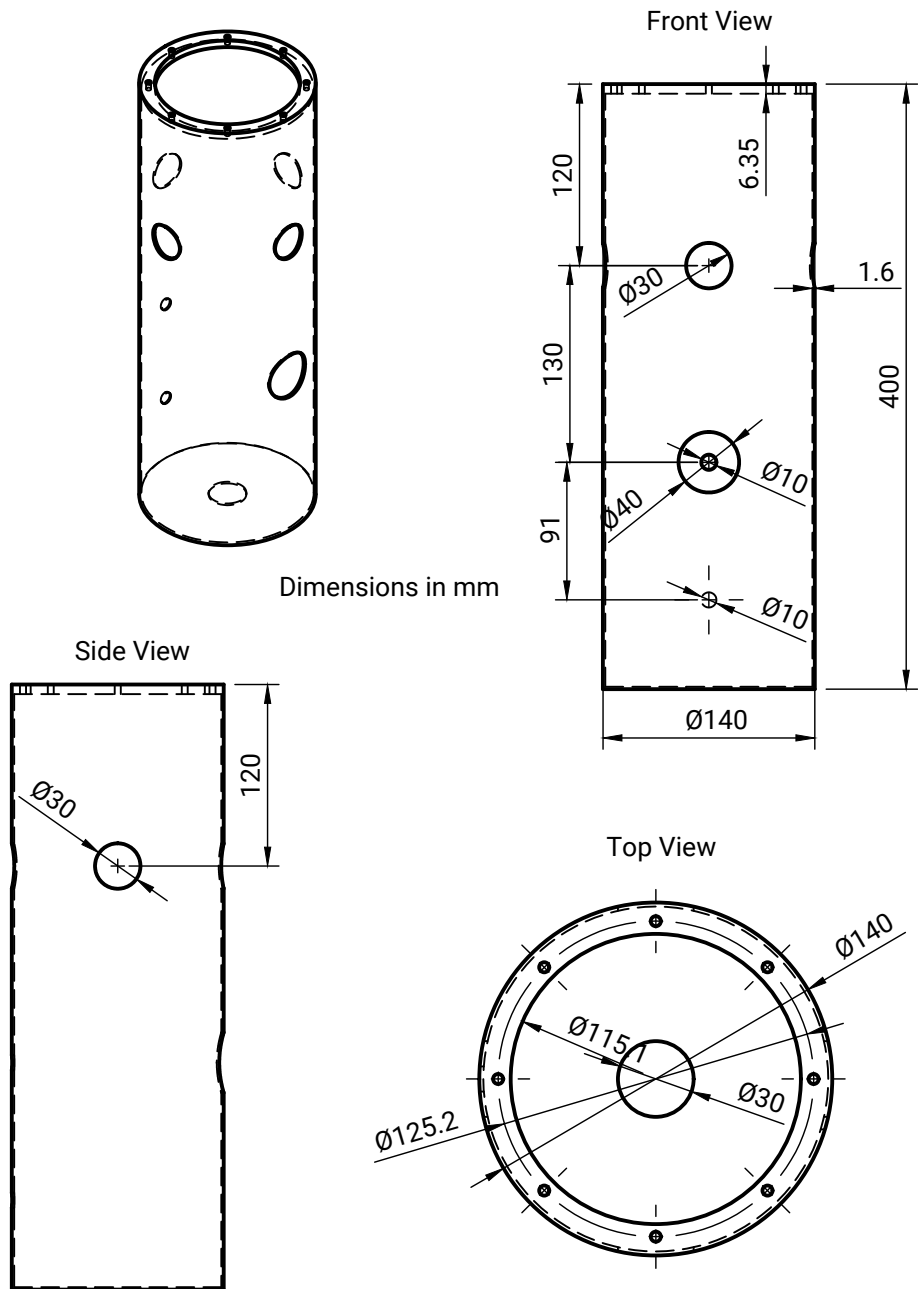


Figure A.7: Technical drawing of the heat shield.

Bibliography

- [1] M. R. Cleland. “Industrial applications of electron accelerators”. In: *CAS - CERN Accelerator School : small accelerators* (2006), pp. 383–416. DOI: 10.5170/CERN-2006-012.383.
- [2] F. R. Elder et al. “Radiation from Electrons in a Synchrotron”. In: *Physical Review* 71.11 (1947), pp. 829–830. DOI: 10.1103/PhysRev.71.829.5.
- [3] R. Neutze et al. “Potential for biomolecular imaging with femtosecond X-ray pulses”. In: *Nature* 406.6797 (2000), pp. 752–757. DOI: 10.1038/35021099.
- [4] R. Hofstadter. “Electron Scattering and Nuclear Structure”. In: *Reviews of Modern Physics* 28.3 (1956), pp. 214–254. DOI: 10.1103/RevModPhys.28.214.
- [5] H. Hertz. “Ueber einen Einfluss des ultravioletten Lichtes auf die electriche Entladung”. In: *Annalen der Physik und Chemie* 267.8 (1887), pp. 983–1000. DOI: 10.1002/andp.18872670827.
- [6] A. Einstein. “Über einen die Erzeugung und Verwandlung des Lichtes betreffenden heuristischen Gesichtspunkt”. In: *Annalen der Physik* 322.6 (1905), pp. 132–148. DOI: 10.1002/andp.19053220607.
- [7] J. Fraser, R. Sheffield, and E. Gray. “A new high-brightness electron injector for free electron lasers driven by RF linacs”. In: *Nuclear Instruments and Methods in Physics Research Section A: Accelerators, Spectrometers, Detectors and Associated Equipment* 250.1 (1986), pp. 71–76. DOI: 10.1016/0168-9002(86)90862-4.
- [8] J. G. Power, S. H. Gold, and G. S. Nusinovich. “Overview of Photoinjectors”. In: *Advanced Accelerator Concepts: 14th Advanced Accelerator Concepts Workshop*. Annapolis, Maryland, 2010, pp. 20–28. DOI: 10.1063/1.3520316.
- [9] A. Todd. “State-of-the-art electron guns and injector designs for energy recovery linacs (ERL)”. In: *Nuclear Instruments and Methods in Physics Research Section A: Accelerators, Spectrometers, Detectors and Associated Equipment* 557.1 (2006), pp. 36–44. DOI: 10.1016/j.nima.2005.10.087.

-
-
- [10] A. Arnold and J. Teichert. “Overview on superconducting photoinjectors”. In: *Physical Review Special Topics - Accelerators and Beams* 14.2 (2011), p. 024801. DOI: 10.1103/PhysRevSTAB.14.024801.
- [11] J. Teichert et al. “Successful user operation of a superconducting radio-frequency photoelectron gun with Mg cathodes”. In: *Physical Review Accelerators and Beams* 24.3 (2021), p. 033401. DOI: 10.1103/PhysRevAccelBeams.24.033401.
- [12] W. Liu et al. “Record-level quantum efficiency from a high polarization strained GaAs/GaAsP superlattice photocathode with distributed Bragg reflector”. In: *Applied Physics Letters* 109.25 (2016), p. 252104. DOI: 10.1063/1.4972180.
- [13] R. Prepost and T. Maruyama. “Advances in Polarized Electron Sources”. In: *Annual Review of Nuclear and Particle Science* 45.1 (1995), pp. 41–88. DOI: 10.1146/annurev.ns.45.120195.000353.
- [14] J. Kessler. “Polarized Electrons”. Berlin, Heidelberg: Springer Berlin Heidelberg, 1985. DOI: 10.1007/978-3-662-02434-8.
- [15] A. A. Turnbull and G. B. Evans. “Photoemission from GaAs-Cs-O”. In: *Journal of Physics D: Applied Physics* 1.2 (1968), pp. 155–160. DOI: 10.1088/0022-3727/1/2/303.
- [16] F. Ciccacci and G. Chiaia. “Comparative study of the preparation of negative electron affinity GaA photocathodes with O₂, and with NF₃”. In: *Journal of Vacuum Science & Technology A: Vacuum, Surfaces, and Films* 9.6 (1991), pp. 2991–2995. DOI: 10.1116/1.577161.
- [17] S. Garbe. “CsF, Cs as a low work function layer on the GaAs photocathode”. In: *Physica Status Solidi (a)* 2.3 (1970), pp. 497–501. DOI: 10.1002/pssa.19700020311.
- [18] B. Dunham et al. “Record high-average current from a high-brightness photoinjector”. In: *Applied Physics Letters* 102.3 (2013), p. 034105. DOI: 10.1063/1.4789395.
- [19] I. Ben-Zvi. “Superconducting energy recovery linacs”. In: *Superconductor Science and Technology* 29.10 (2016), p. 103002. DOI: 10.1088/0953-2048/29/10/103002.
- [20] C. K. Sinclair. “DC photoemission electron guns as ERL sources”. In: *Nuclear Instruments and Methods in Physics Research Section A: Accelerators, Spectrometers, Detectors and Associated Equipment* 557.1 (2006), pp. 69–74. DOI: 10.1016/j.nima.2005.10.053.

-
-
- [21] K. Smolenski et al. “Design and Performance of the Cornell ERL DC Photoemission Gun”. In: *AIP Conference Proceedings*. Spin Physics: 18th International Spin Physics Symposium. Charlottesville, Virginia: AIP, 2009, pp. 1077–1083. DOI: 10.1063/1.3215596.
- [22] T. Rao et al. “Photocathodes for the energy recovery linacs”. In: *Nuclear Instruments and Methods in Physics Research Section A: Accelerators, Spectrometers, Detectors and Associated Equipment* 557.1 (2006), pp. 124–130. DOI: 10.1016/j.nima.2005.10.112.
- [23] T. Siggins et al. “Performance of a DC GaAs photocathode gun for the Jefferson lab FEL”. In: *Nuclear Instruments and Methods in Physics Research Section A: Accelerators, Spectrometers, Detectors and Associated Equipment* 475.1 (2001), pp. 549–553. DOI: 10.1016/S0168-9002(01)01596-0.
- [24] H. Wang et al. “A GaAs Photoemission DC Gun for CAEP High-average-power THz FEL”. In: *Proceeding of FEL 2014*. 2014, pp. 318–321.
- [25] O. Gayou et al. “Measurements of the elastic electromagnetic form factor ratio $\mu p G_E^p / G_M^p$ via polarization transfer”. In: *Physical Review C* 64.3 (2001), p. 038202. DOI: 10.1103/PhysRevC.64.038202.
- [26] D. Adhikari et al. “Accurate Determination of the Neutron Skin Thickness of Pb 208 through Parity-Violation in Electron Scattering”. In: *Physical Review Letters* 126.17 (2021), p. 172502. DOI: 10.1103/PhysRevLett.126.172502.
- [27] D. Becker et al. “The P2 experiment: A future high-precision measurement of the weak mixing angle at low momentum transfer”. In: *The European Physical Journal A* 54.11 (2018), p. 208. DOI: 10.1140/epja/i2018-12611-6.
- [28] D. Abbott et al. “Production of Highly Polarized Positrons Using Polarized Electrons at MeV Energies”. In: *Physical Review Letters* 116.21 (2016), p. 214801. DOI: 10.1103/PhysRevLett.116.214801.
- [29] D. A. Orlov et al. “Ultra Cold Photoelectron Beams for Ion Storage Rings”. In: *AIP Conference Proceedings*. Spin Physics: 18th International Spin Physics Symposium. Charlottesville, Virginia, 2009, pp. 1007–1016. DOI: 10.1063/1.3215583.
- [30] J. Skaritka et al. “Conceptual design of a Polarized Electron Ion Collider at Brookhaven National Laboratory”. In: *Proceedings of 17th International Workshop on Polarized Sources, Targets & Polarimetry — PoS(PSTP2017)*. Kaist, South Korea: Sissa Medialab, 2018, p. 015. DOI: 10.22323/1.324.0015.

-
-
- [31] G. Moortgat-Pick et al. “Polarized positrons and electrons at the linear collider”. In: *Physics Reports* 460.4 (2008), pp. 131–243. DOI: 10.1016/j.physrep.2007.12.003.
- [32] A. Brachmann et al. “The Polarized Electron Source for the International Collider (ILC) Project”. In: *AIP Conference Proceedings*. Spin Physics: 17th International Spin Physics Symposium. Vol. 915. Kyoto, Japan: AIP, 2007, pp. 1091–1094. DOI: 10.1063/1.2750959.
- [33] N. Pietralla. “The Institute of Nuclear Physics at the TU Darmstadt”. In: *Nuclear Physics News* 28.2 (2018), pp. 4–11. DOI: 10.1080/10619127.2018.1463013.
- [34] M. Arnold et al. “First operation of the superconducting Darmstadt linear electron accelerator as an energy recovery linac”. In: *Physical Review Accelerators and Beams* 23.2 (2020), p. 020101. DOI: 10.1103/PhysRevAccelBeams.23.020101.
- [35] F. Schliessmann et al. “Realization of a multi-turn energy recovery accelerator”. In: *Nat. Physics* (2023). DOI: 10.1038/s41567-022-01856-w.
- [36] Y. Poltoratska et al. “Status and recent developments at the polarized-electron injector of the superconducting Darmstadt electron linear accelerator S-DALINAC”. In: *Journal of Physics: Conference Series* 298 (2011), p. 012002. DOI: 10.1088/1742-6596/298/1/012002.
- [37] J. Enders. “Ideas for fundamental electron scattering at the S-DALINAC”. In: *AIP Conference Proceedings* 1563.1 (2013), pp. 223–226. DOI: 10.1063/1.4829415.
- [38] J. Enders et al. “Reactions with polarized electrons and photons at low momentum transfers at the superconducting Darmstadt electron linear accelerator S-DALINAC”. In: *Journal of Physics: Conference Series* 295 (2011), p. 012152. DOI: 10.1088/1742-6596/295/1/012152.
- [39] C. Eckardt et al. “Polarized Electrons for Experiments at Low Momentum Transfer SPIN @ S-DALINAC”. In: *AIP Conference Proceedings*. Spin Physics: 18th International Spin Physics Symposium. Charlottesville, Virginia: AIP, 2009, pp. 919–922. DOI: 10.1063/1.3215793.
- [40] E. Yee and D. Jackson. “Photoyield decay characteristics of a cesiated GaAs photocathode”. In: *Solid-State Electronics* 15.2 (1972), pp. 245–247. DOI: 10.1016/0038-1101(72)90058-5.

-
-
- [41] C. K. Sinclair et al. “Development of a high average current polarized electron source with long cathode operational lifetime”. In: *Physical Review Special Topics - Accelerators and Beams* 10.2 (2007), p. 023501. DOI: 10.1103/PhysRevSTAB.10.023501.
- [42] M. Espig. “Entwicklung, Aufbau und Charakterisierung einer variabel repetierenden, spinpolarisierten Elektronenkanone mit invertierter Isolatorgeometrie”. Doctoral Dissertation. Darmstadt: Technische Universität Darmstadt, 2016.
- [43] N. Kurichiyani. “Design and construction of a test stand for photocathode research and experiments”. PhD thesis. Darmstadt: Technische Universität Darmstadt, 2017.
- [44] N. Kurichiyani et al. “A test system for optimizing quantum efficiency and dark lifetime of GaAs photocathodes”. In: *Journal of Instrumentation* 14.8 (2019), P08025–P08025. DOI: 10.1088/1748-0221/14/08/P08025.
- [45] M. Herbert et al. “Inverted Geometry Photo-Electron Gun Research and Development at TU Darmstadt”. In: *Proceedings of the 9th International Particle Accelerator Conference (IPAC’18)*. Vancouver, BC, Canada: JACoW Publishing, Geneva, Switzerland, 2018, pp. 4545–4547. DOI: 10.18429/JACOW-IPAC2018-THPMK101.
- [46] G. A. Mulhollan and J. C. Bierman. “Enhanced chemical immunity for negative electron affinity GaAs photoemitters”. In: *Journal of Vacuum Science & Technology A: Vacuum, Surfaces, and Films* 26.5 (2008), pp. 1195–1197. DOI: 10.1116/1.2965816.
- [47] J. K. Bae et al. “Improved lifetime of a high spin polarization superlattice photocathode”. In: *Journal of Applied Physics* 127.12 (2020), p. 124901. DOI: 10.1063/1.5139674.
- [48] J. Biswas et al. “High quantum efficiency GaAs photocathodes activated with Cs, O₂, and Te”. In: *AIP Advances* 11.2 (2021), p. 025321. DOI: 10.1063/5.0026839.
- [49] M. Herbert. “Electron emission from GaAs photocathodes using conventional and Li-enhanced activation procedures”. Doctoral Dissertation. Darmstadt: Technische Universität Darmstadt, 2022.
- [50] D. T. Pierce and F. Meier. “Photoemission of spin-polarized electrons from GaAs”. In: *Physical Review B* 13.12 (1976), pp. 5484–5500. DOI: 10.1103/PhysRevB.13.5484.
- [51] W. Hallwachs. “Ueber den Einfluss des Lichtes auf electrostatisch geladene Körper”. In: *Annalen der Physik und Chemie* 269.2 (1888), pp. 301–312. DOI: 10.1002/andp.18882690206.

-
-
- [52] P. Lenard. "Ueber die lichtelektrische Wirkung". In: *Annalen der Physik* 313.5 (1902), pp. 149–198. DOI: 10.1002/andp.19023130510.
- [53] W. E. Spicer. "Photoemissive, Photoconductive, and Optical Absorption Studies of Alkali-Antimony Compounds". In: *Physical Review* 112.1 (1958), pp. 114–122. DOI: 10.1103/PhysRev.112.114.
- [54] W. E. Spicer. "Photoemission and Related Properties of the Alkali-Antimonides". In: *Journal of Applied Physics* 31.12 (1960), pp. 2077–2084. DOI: 10.1063/1.1735505.
- [55] C. N. Berglund and W. E. Spicer. "Photoemission Studies of Copper and Silver: Theory". In: *Physical Review* 136.4 (1964), A1030–A1044. DOI: 10.1103/PhysRev.136.A1030.
- [56] C. N. Berglund and W. E. Spicer. "Photoemission Studies of Copper and Silver: Experiment". In: *Physical Review* 136.4 (1964), A1044–A1064. DOI: 10.1103/PhysRev.136.A1044.
- [57] W. E. Spicer and A. Herrera-Gomez. "Modern theory and applications of photocathodes". In: SPIE's 1993 International Symposium on Optics, Imaging, and Instrumentation. San Diego, CA, 1993, p. 18. DOI: 10.1117/12.158575.
- [58] K. H. Herrmann. "Der Photoeffekt Grundlagen der Strahlungsmessung". Braunschweig / Wiesbaden: Vieweg+Teubner Verlag, 1994.
- [59] N. A. Soboleva. "A new class of electron emitters". In: *Soviet Physics Uspekhi* 16.5 (1974), pp. 726–738. DOI: 10.1070/pu1974v016n05abeh004152.
- [60] S. Hüfner. "Photoelectron Spectroscopy". Advanced Texts in Physics. Berlin, Heidelberg: Springer Berlin Heidelberg, 2003. DOI: 10.1007/978-3-662-09280-4.
- [61] G. D. Mahan. "Theory of Photoemission in Simple Metals". In: *Physical Review B* 2.11 (1970), pp. 4334–4350. DOI: 10.1103/PhysRevB.2.4334.
- [62] C. D. Thurmond. "The Standard Thermodynamic Functions for the Formation of Electrons and Holes in Ge, Si, GaAs, and GaP". In: *Journal of The Electrochemical Society* 122.8 (1975), pp. 1133–1141. DOI: 10.1149/1.2134410.
- [63] K. L. Jensen et al. "A photoemission model for low work function coated metal surfaces and its experimental validation". In: *Journal of Applied Physics* 99.12 (2006), p. 124905. DOI: 10.1063/1.2203720.
- [64] J. Scheer and J. van Laar. "GaAs-Cs: A new type of photoemitter". In: *Solid State Communications* 3.8 (1965), pp. 189–193. DOI: 10.1016/0038-1098(65)90289-9.

-
-
- [65] G. Lampel and C. Weisbuch. “Proposal for an efficient source of polarized photoelectrons from semiconductors”. In: *Solid State Communications* 16.7 (1975), pp. 877–880. DOI: 10.1016/0038-1098(75)90884-4.
- [66] D. T. Pierce, F. Meier, and P. Zürcher. “Negative electron affinity GaAs: A new source of spin-polarized electrons”. In: *Applied Physics Letters* 26.12 (1975), pp. 670–672. DOI: 10.1063/1.88030.
- [67] J. S. Blakemore. “Semiconducting and other major properties of gallium arsenide”. In: *Journal of Applied Physics* 53.10 (1982), R123–R181. DOI: 10.1063/1.331665.
- [68] Y. Varshni. “Temperature dependence of the energy gap in semiconductors”. In: *Physica* 34.1 (1967), pp. 149–154. DOI: 10.1016/0031-8914(67)90062-6.
- [69] H. Ehrenreich. “Band Structure and Electron Transport of GaAs”. In: *Physical Review* 120.6 (1960), pp. 1951–1963. DOI: 10.1103/PhysRev.120.1951.
- [70] J. R. Chelikowsky and M. L. Cohen. “Electronic Structure of GaAs”. In: *Physical Review Letters* 32.12 (1974), pp. 674–677. DOI: 10.1103/PhysRevLett.32.674.
- [71] S. Kayali. “GaAs Material Properties”. In: *JPL Publication* 96 (2006), pp. 25–33.
- [72] V. Guidi. “Polarized electron sources”. In: *Hyperfine Interactions* 127.1 (2000), pp. 455–462. DOI: 10.1023/A:1012626019500.
- [73] P. Zorabedian. “Optical Pumping and Photoluminescence Detection of Spin-Polarized Electrons in Uniaxially Stressed Gallium”. PhD thesis. Stanford: Stanford University, 1982.
- [74] F. Ciccacci, E. Molinari, and N. Christensen. “GaAs/AlAs monolayer superlattices: A new candidate for a highly spin-polarized electron source”. In: *Solid State Communications* 62.1 (1987), pp. 1–3. DOI: 10.1016/0038-1098(87)90071-8.
- [75] T. Maruyama et al. “Electron-spin polarization in photoemission from strained GaAs grown on GaAs_{1-x}P_x”. In: *Physical Review B* 46.7 (1992), pp. 4261–4264. DOI: 10.1103/PhysRevB.46.4261.
- [76] T. Maruyama et al. “Observation of strain-enhanced electron-spin polarization in photoemission from InGaAs”. In: *Physical Review Letters* 66.18 (1991), pp. 2376–2379. DOI: 10.1103/PhysRevLett.66.2376.

-
- [77] F. Meier et al. “Spin-polarized electrons from $\text{In}_x\text{Ga}_{1-x}\text{As}$ thin films”. In: *Physica Scripta* T49B (1993), pp. 574–578. DOI: 10.1088/0031-8949/1993/T49B/034.
- [78] E. Pelucchi, S. De Rossi, and F. Ciccacci. “Spin polarized photoemission from thin GaAs photocathodes”. In: *Journal of Electron Spectroscopy and Related Phenomena* 76 (1995), pp. 505–509. DOI: 10.1016/0368-2048(95)02510-3.
- [79] T. Omori et al. “Large enhancement of polarization observed by extracted electrons from the AlGaAs-GaAs superlattice”. In: *Physical Review Letters* 67.23 (1991), pp. 3294–3297. DOI: 10.1103/PhysRevLett.67.3294.
- [80] N. Yamamoto et al. “High brightness and high polarization electron source using transmission photocathode with GaAs-GaAsP superlattice layers”. In: *Journal of Applied Physics* 103.6 (2008), p. 064905. DOI: 10.1063/1.2887930.
- [81] Y. A. Mamaev et al. “Optimized photocathode for spin-polarized electron sources”. In: *Applied Physics Letters* 93.8 (2008), p. 081114. DOI: 10.1063/1.2976437.
- [82] R. Alley et al. “The Stanford linear accelerator polarized electron source”. In: *Nuclear Instruments and Methods in Physics Research Section A: Accelerators, Spectrometers, Detectors and Associated Equipment* 365.1 (1995), pp. 1–27. DOI: 10.1016/0168-9002(95)00450-5.
- [83] K. Aulenbacher. “Polarized beams for electron accelerators”. In: *The European Physical Journal Special Topics* 198.1 (2011), pp. 361–380. DOI: 10.1140/epjst/e2011-01499-6.
- [84] G. Fishman and G. Lampel. “Spin relaxation of photoelectrons in p-type gallium arsenide”. In: *Physical Review B* 16.2 (1977), pp. 820–831. DOI: 10.1103/PhysRevB.16.820.
- [85] M. Zolotarev. “Effect of radiation trapping on polarization of photoelectrons from semiconductors”. SLAC National Accelerator Lab., Menlo Park, CA (United States), 1994.
- [86] W. E. Spicer and R. L. Bell. “The III-V Photocathode: A Major Detector Development”. In: *Publications of the Astronomical Society of the Pacific* 84 (1972), p. 110. DOI: 10.1086/129256.
- [87] W. E. Spicer. “Negative affinity 3–5 photocathodes: Their physics and technology”. In: *Applied Physics* 12.2 (1977), pp. 115–130. DOI: 10.1007/BF00896137.
- [88] T. Nishitani et al. “High-Brightness Spin-Polarized Electron Source Using Semiconductor Photocathodes”. In: *Japanese Journal of Applied Physics* 48.6 (2009), 06FF02. DOI: 10.1143/JJAP.48.06FF02.

-
-
- [89] G. Vergara et al. “Influence of the dopant concentration on the photoemission in NEA GaAs photocathodes”. In: *Vacuum* 48.2 (1997), pp. 155–160. DOI: 10.1016/S0042-207X(96)00234-5.
- [90] K. Aulenbacher. “Erzeugung intensiver hochpolarisierter Elektronenstrahlen mit hoher Symmetrie unter Helizitätswechs”. Habilitationsschrift. Mainz: Johannes Gutenberg-Universität Mainz, 2007.
- [91] J. Van Laar and J. Scheer. “Influence of volume dope on Fermi level position at gallium arsenide surfaces”. In: *Surface Science* 8.3 (1967), pp. 342–356. DOI: 10.1016/0039-6028(67)90116-1.
- [92] J. Scheer and J. van Laar. “Fermi level stabilization at cesiated semiconductor surfaces”. In: *Solid State Communications* 5.4 (1967), pp. 303–306. DOI: 10.1016/0038-1098(67)90278-5.
- [93] J. Kirschner, H. P. Oepen, and H. Ibach. “Energy- and spin-analysis of polarized photoelectrons from NEA GaAsP”. In: *Applied Physics A Solids and Surfaces* 30.3 (1983), pp. 177–183. DOI: 10.1007/BF00620537.
- [94] Y.-Z. Liu, J. L. Moll, and W. E. Spicer. “Effects of Heat Cleaning on the Photoemission Properties of GaAs Surfaces”. In: *Applied Physics Letters* 14.9 (1969), pp. 275–277. DOI: 10.1063/1.1652812.
- [95] T. Maruyama et al. “Atomic hydrogen cleaning of polarized GaAs photocathodes”. In: *Applied Physics Letters* 82.23 (2003), pp. 4184–4186. DOI: 10.1063/1.1581981.
- [96] S. Sugata. “GaAs cleaning with a hydrogen radical beam gun in an ultrahigh-vacuum system”. In: *Journal of Vacuum Science & Technology B: Microelectronics and Nanometer Structures* 6.4 (1988), p. 1087. DOI: 10.1116/1.584302.
- [97] X. Jin et al. “Recovery of quantum efficiency in spin-polarized photocathodes by atomic hydrogen cleaning”. In: *Ultramicroscopy* 183 (2017), pp. 89–93. DOI: 10.1016/j.ultramic.2017.03.033.
- [98] J. K. Bae et al. “Enhanced Robustness of GaAs-Based Photocathodes Activation by Cs, Sb, and O₂”. In: *Proceedings of the North American Particle Accelerator Conference (NAPAC2019)*. JACoW Publishing, Geneva, Switzerland, 2019. DOI: 10.18429/JACOW-NAPAC2019-MOPLH17.
- [99] C. Shonaka et al. “A Study of Lifetime of GaAs Photocathode for High Brightness Electron Source”. In: *Proceedings of the 23rd Particle Accelerator Conference (PAC’09)*. 2010, pp. 527–529.

-
-
- [100] J. J. Uebbing. "Use of Auger Electron Spectroscopy in Determining the Effect of Carbon and Other Surface Contaminants on GaAs-Cs-O Photocathodes". In: *Journal of Applied Physics* 41.2 (1970), pp. 802–804. DOI: 10.1063/1.1658753.
- [101] N. Chanlek et al. "The degradation of quantum efficiency in negative electron affinity GaAs photocathodes under gas exposure". In: *Journal of Physics D: Applied Physics* 47.5 (2014), p. 055110. DOI: 10.1088/0022-3727/47/5/055110.
- [102] D. Durek et al. "Degradation of a gallium-arsenide photoemitting NEA surface by water vapour". In: *Applied Surface Science* 143.1 (1999), pp. 319–322. DOI: 10.1016/S0169-4332(99)00085-9.
- [103] T. Wada et al. "Influence of Exposure to CO, CO₂ and H₂O on the Stability of GaAs Photocathodes". In: *Japanese Journal of Applied Physics* 29 (Part 1, No. 10 1990), pp. 2087–2091. DOI: 10.1143/JJAP.29.2087.
- [104] H. Fischer, P. Drescher, and E. Reichert. "Thermal Stability of Cs on NEA III-V-Cathodes and its Effect on Quantum Efficiency". In: *on Photocathodes for Polarized Electron Sources for Accelerators* (1994), p. 248.
- [105] M. Kuriki et al. "Dark-lifetime degradation of GaAs photo-cathode at higher temperature". In: *Nuclear Instruments and Methods in Physics Research Section A: Accelerators, Spectrometers, Detectors and Associated Equipment* 637.1 (2011), S87–S90. DOI: 10.1016/j.nima.2010.02.029.
- [106] B. Goldstein and D. Szostak. "Different bonding states of Cs and O on highly photoemissive GaAs by flash-desorption experiments". In: *Applied Physics Letters* 26.3 (1975), pp. 111–113. DOI: 10.1063/1.88083.
- [107] M. Lax. "Temperature rise induced by a laser beam". In: *Journal of Applied Physics* 48.9 (1977), pp. 3919–3924. DOI: 10.1063/1.324265.
- [108] J. O. Akinlami and A. O. Ashamu. "Optical properties of GaAs". In: *Journal of Semiconductors* 34.3 (2013), p. 032002. DOI: 10.1088/1674-4926/34/3/032002.
- [109] R. Suleiman et al. "High current polarized electron source". In: *AIP Conference Proceedings*. Newport News, VA, USA, 2018, p. 050007. DOI: 10.1063/1.5040226.
- [110] S. Zhang, S. Benson, and C. H-Garcia. "Observation and measurement of temperature rise and distribution on GaAs photo-cathode wafer with a 532nm drive laser and a thermal imaging camera". In: *Nuclear Instruments and Methods in Physics Research Section A: Accelerators, Spectrometers, Detectors and Associated Equipment* 631.1 (2011), pp. 22–25. DOI: 10.1016/j.nima.2010.12.132.

-
-
- [111] K. Aulenbacher. “Status of the polarized source at MAMI”. In: *AIP Conference Proceedings*. Spin Physics: 15th International Spin Physics Symposium and Workshop on Polarized Electron Sources and Polarimeters. Vol. 675. Upton, New York, USA: AIP, 2003, pp. 1088–1092. DOI: 10.1063/1.1607302.
- [112] L. J. Kieffer and G. H. Dunn. “Electron Impact Ionization Cross-Section Data for Atoms, Atomic Ions, and Diatomic Molecules: I. Experimental Data”. In: *Reviews of Modern Physics* 38.1 (1966), pp. 1–35. DOI: 10.1103/RevModPhys.38.1.
- [113] H. Schade, H. Nelson, and H. Kressel. “Novel GaAs-(AlGa)As Cold-Cathode Structure and Factors Affecting Extended Operation”. In: *Applied Physics Letters* 20.10 (1972), pp. 385–387. DOI: 10.1063/1.1653986.
- [114] E. Pozdeyev. “Ion trapping and cathode bombardment by trapped ions in dc photoguns”. In: *Physical Review Special Topics - Accelerators and Beams* 10.8 (2007), p. 083501. DOI: 10.1103/PhysRevSTAB.10.083501.
- [115] W. Liu et al. “Effects of ion bombardment on bulk GaAs photocathodes with different surface-cleavage planes”. In: *Physical Review Accelerators and Beams* 19.10 (2016), p. 103402. DOI: 10.1103/PhysRevAccelBeams.19.103402.
- [116] P. Rabinzohn et al. “Cleaning of Si and GaAs Crystal Surfaces by Ion Bombardment in the 50–1500 eV Range: Influence of Bombarding Energy and Sample Temperature on Damage and Incorporation”. In: *Journal of The Electrochemical Society* 131.4 (1984), pp. 905–914. DOI: 10.1149/1.2115726.
- [117] J. Yoskowitz et al. “New Simulations for Ion-Production and Back-Bombardment in GaAs Photo-guns”. In: *Proceedings of the 18th International Workshop on Polarized Sources, Targets, and Polarimetry — PoS(PSTP2019)*. Knoxville, Tennessee: Sissa Medialab, 2020, p. 040. DOI: 10.22323/1.379.0040.
- [118] O. Rahman et al. “Increasing charge lifetime in DC polarized electron guns by offsetting the anode”. In: *Physical Review Accelerators and Beams* 22.8 (2019), p. 083401. DOI: 10.1103/PhysRevAccelBeams.22.083401.
- [119] R. Ramsier and J. Yates. “Electron-stimulated desorption: Principles and applications”. In: *Surface Science Reports* 12.6 (1991), pp. 246–378. DOI: 10.1016/0167-5729(91)90013-N.
- [120] C. Sinclair. “Very high voltage photoemission electron guns”. In: *Proceedings of the 2003 Particle Accelerator Conference*. Portland, OR, USA: IEEE, 2003, pp. 76–80. DOI: 10.1109/PAC.2003.1288845.

-
-
- [121] P. Förster et al. “Freeform shape optimization of a compact dc photoelectron gun using isogeometric analysis”. In: *Physical Review Accelerators and Beams* 25.3 (2022), p. 034601. DOI: 10.1103/PhysRevAccelBeams.25.034601.
- [122] D. W. Umrath et al. “Grundlagen der Vakuumtechnik”. Köln, Germany, 1997.
- [123] B. Halliday. “Cleaning materials and components for vacuum use”. In: *Vacuum* 37.8 (1987), pp. 587–591. DOI: 10.1016/0042-207X(87)90042-X.
- [124] A. Berman. “Water vapor in vacuum systems”. In: *Vacuum* 47.4 (1996), pp. 327–332. DOI: 10.1016/0042-207X(95)00246-4.
- [125] R. Calder and G. Lewin. “Reduction of stainless-steel outgassing in ultra-high vacuum”. In: *British Journal of Applied Physics* 18.10 (1967), pp. 1459–1472. DOI: 10.1088/0508-3443/18/10/313.
- [126] Y. Ishikawa and V. Nemanič. “An overview of methods to suppress hydrogen outgassing rate from austenitic stainless steel with reference to UHV and EXV”. In: *Vacuum* 69.4 (2003), pp. 501–512. DOI: 10.1016/S0042-207X(02)00562-6.
- [127] K. Jousten. “Handbook of Vacuum Technology”. Weinheim: Wiley-VCH Verlag GmbH & Co. KGaA, 2016.
- [128] K. Ichimura, M. Matsuyama, and K. Watanabe. “Alloying effect on the activation processes of Zr-alloy getters”. In: *Journal of Vacuum Science & Technology A: Vacuum, Surfaces, and Films* 5.2 (1987), pp. 220–225. DOI: 10.1116/1.574107.
- [129] M. Sancrotti, G. Trezzi, and P. Manini. “An x-ray photoemission spectroscopy investigation of thermal activation induced changes in surface composition and chemical bonds of two gettering alloys: Zr₂Fe versus Zr₅₇V₃₆Fe₇”. In: *Journal of Vacuum Science & Technology A: Vacuum, Surfaces, and Films* 9.2 (1991), pp. 182–189. DOI: 10.1116/1.577518.
- [130] C. Day. “Basics and applications of cryopumps”. In: *CAS - CERN Accelerator School: Vacuum in Accelerators* (2007), p. 34. DOI: 10.5170/CERN-2007-003.241.
- [131] C. Day. “The use of active carbons as cryosorbent”. In: *Colloids and Surfaces A: Physicochemical and Engineering Aspects* 187-188 (2001), pp. 187–206. DOI: 10.1016/S0927-7757(01)00630-6.
- [132] S. A. Stern et al. “Cryosorption Pumping of Hydrogen and Helium at 20 °K”. In: *Journal of Vacuum Science and Technology* 2.4 (1965), pp. 165–177. DOI: 10.1116/1.1492421.

-
-
- [133] G. E. Grenier and S. A. Stern. “Cryosorption Pumping of Helium at 4.2 °K”. In: *Journal of Vacuum Science and Technology* 3.6 (1966), pp. 334–337. DOI: 10.1116/1.1492498.
- [134] R. A. Haefer. “Cryogenic vacuum techniques”. In: *Journal of Physics E: Scientific Instruments* 14.3 (1981), pp. 273–288. DOI: 10.1088/0022-3735/14/3/002.
- [135] E. Wallén. “Adsorption isotherms of H₂ and mixtures of H₂, CH₄, CO, and CO₂ on copper plated stainless steel at 4.2 K”. In: *Journal of Vacuum Science & Technology A: Vacuum, Surfaces, and Films* 14.5 (1996), pp. 2916–2929. DOI: 10.1116/1.580245.
- [136] D. Perinic, H. Haas, and A. Mack. “Development of Cryosorption Panels for Cryopumps”. In: *Advances in Cryogenic Engineering*. Ed. by P. Kittel. Vol. 39. Boston, MA: Springer US, 1994, pp. 1553–1559. DOI: 10.1007/978-1-4615-2522-6_190.
- [137] D. Perinic, H. Haas, and A. Mack. “Development of cryosorption panels for plasma exhaust cryopumping”. In: *Fusion Engineering and Design* 18 (1991), pp. 79–84. DOI: 10.1016/0920-3796(91)90111-3.
- [138] D. W. Sedgley et al. “Cryopumping for fusion reactors”. In: *Nuclear Engineering and Design. Fusion* 4.2 (1987), pp. 149–163. DOI: 10.1016/0167-899X(87)90002-4.
- [139] D. W. Sedgley et al. “Characterization of charcoals for helium cryopumping in fusion devices”. In: *Journal of Vacuum Science & Technology A: Vacuum, Surfaces, and Films* 5.4 (1987), pp. 2572–2576. DOI: 10.1116/1.574424.
- [140] A. G. Tobin et al. “Evaluation of charcoal sorbents for helium cryopumping in fusion reactors”. In: *Journal of Vacuum Science & Technology A: Vacuum, Surfaces, and Films* 5.1 (1987), pp. 101–105. DOI: 10.1116/1.574141.
- [141] D. W. Sedgley, T. H. Batzer, and W. R. Call. “Helium cryopumping for fusion applications”. In: *Journal of Vacuum Science & Technology A: Vacuum, Surfaces, and Films* 6.3 (1988), pp. 1209–1213. DOI: 10.1116/1.575679.
- [142] M. Xu and Y. Matsui. “Obtaining extremely high vacuum using sintered fine copper powder as a cryosorbent”. In: *Journal of Vacuum Science & Technology A: Vacuum, Surfaces, and Films* 13.1 (1995), pp. 132–135. DOI: 10.1116/1.579426.
- [143] J. Ma et al. “Multilayer Adsorption of H₂ on Uniform MgO Substrates”. In: *Physical Review Letters* 61.20 (1988), pp. 2348–2351. DOI: 10.1103/PhysRevLett.61.2348.

-
-
- [144] S. A. Stern, R. A. Hemstreet, and D. M. Ruttenbur. “Cryosorption Pumping of Hydrogen at 20 °K II. Development and Performance of Cryosorption Panels”. In: *Journal of Vacuum Science and Technology* 3.3 (1966), pp. 99–106. DOI: 10.1116/1.1492461.
- [145] S. Horn and B. Kammerer. German pat. 4041725. 1995.
- [146] C. Day and A. Mack. “Investigation into the pumping characteristics of ITER cryopumps”. In: *Fusion Engineering and Design* 39-40 (1998), pp. 955–962. DOI: 10.1016/S0920-3796(98)00213-0.
- [147] P. Lebrun. “An Introduction to Cryogenics”. Accelerator Technology Department, Departmental Report. Geneva: CERN, 2007.
- [148] R. A. Haefer. “Kryo-Vakuumtechnik”. Berlin, Heidelberg: Springer Berlin Heidelberg, 1981. DOI: 10.1007/978-3-642-49985-2.
- [149] W. E. Gifford and H. O. McMahon. “A New Low-Temperature Gas Expansion Cycle”. In: *Advances in Cryogenic Engineering*. Ed. by K. D. Timmerhaus. Boston, MA: Springer US, 1960, pp. 368–372. DOI: 10.1007/978-1-4757-0537-9_44.
- [150] H. Lee, I. Bazarov, L. Cultrera, et al. “A cryogenically cooled high voltage dc photogun”. In: *Proceedings of the 8th International Particle Accelerator Conference (IPAC'17)*. JACOW, Geneva, Switzerland, 2017, pp. 1618–1621.
- [151] “Experimental Physics and Industrial Control System”. URL: <https://epics-controls.org> (visited on 05/04/2022).
- [152] C. W. Burandt. “Optimierung und Test der digitalen Hochfrequenzregelung und Entwicklungen für das EPICS-basierte Beschleunigerkontrollsystem am S-DALINAC”. Doctoral Dissertation. Darmstadt: Technische Universität Darmstadt, 2016.
- [153] “CSS - Control System Studio”. URL: <https://controlsystemstudio.org/> (visited on 05/04/2022).
- [154] M. Engart. “Automatisierte Aktivierungsverfahren für GaAs-Photokathoden”. Bachelor Thesis (unpublished). Darmstadt: Technische Universität Darmstadt, 2020.
- [155] Lakeshore. “Appendix I: Cryogenic Reference Tables”. URL: https://www.lakeshore.com/docs/default-source/product-downloads/literature/lstc_appendixi_1.pdf?sfvrsn=5f2ab85b_4 (visited on 06/11/2022).
- [156] S. Raghavan. “Thermal properties of zirconia co-doped with trivalent and pentavalent oxides”. In: *Acta Materialia* 49.1 (2001), pp. 169–179. DOI: 10.1016/S1359-6454(00)00295-0.

-
-
- [157] C. Budzylek (Cryoandmore Budzylek GbR). Private Communication. E-mail. 2017.
- [158] J. R. Pierce. “Theory and design of electron beams”. Bell Telephone Laboratories series. Books on Demand, 1954.
- [159] J. M. Lafferty, ed. *Foundations of vacuum science and technology*. New York: Wiley, 1998.
- [160] Dr. Yuliya Fritzsche, Private Communication. 2021.
- [161] “Molflow+”. URL: <https://molflow.web.cern.ch/> (visited on 12/10/2022).
- [162] G. Moraw and R. Dobrozemsky. “Attainment of Outgassing Rates Below 10^{-13} Torr Liters/Sec cm^2 for Aluminium and Stainless Steel After Bakeout at Moderate Temperatures”. In: *Japanese Journal of Applied Physics* 13 (S1 1974), p. 261. DOI: 10.7567/JJAPS.2S1.261.
- [163] M. BastaniNejad et al. “Improving the performance of stainless-steel DC high voltage photoelectron gun cathode electrodes via gas conditioning with helium or krypton”. In: *Nuclear Instruments and Methods in Physics Research Section A: Accelerators, Spectrometers, Detectors and Associated Equipment* 762 (2014), pp. 135–141. DOI: 10.1016/j.nima.2014.05.114.
- [164] C. Hernandez-Garcia, M. Poelker, and J. Hansknecht. “High voltage studies of inverted-geometry ceramic insulators for a 350 kV DC polarized electron gun”. In: *IEEE Transactions on Dielectrics and Electrical Insulation* 23.1 (2016), pp. 418–427. DOI: 10.1109/TDEI.2015.005126.
- [165] M. A. A. Mamun et al. “TiN coated aluminum electrodes for DC high voltage electron guns”. In: *Journal of Vacuum Science & Technology A: Vacuum, Surfaces, and Films* 33.3 (2015), p. 031604. DOI: 10.1116/1.4916574.
- [166] M. Jacewicz et al. “Temperature-Dependent Field Emission and Breakdown Measurements Using a Pulsed High-Voltage Cryosystem”. In: *Physical Review Applied* 14.6 (2020), p. 061002. DOI: 10.1103/PhysRevApplied.14.061002.
- [167] M. Clemens and T. Weil. “Discrete Electromagnetism with the Finite Integration Technique”. In: *Progress In Electromagnetics Research* 32 (2001), pp. 65–87. DOI: 10.2528/PIER00080103.

-
-
- [168] CST. “Understanding Time Domain Meshing in CST MICROWAVE STUDIO®”. 2010. URL: https://www.researchgate.net/profile/Amjad-Ali-47/post/In_the_CST_MWS_software_in_the_local_mesh_properties_window_one_can_change_the_edge_volume_refinement_factors_What_do_they_mean/attachment/5eb20d4e4f9a520001e49fdc/AS%3A888000049324032%401588727118649/download/white_paper_meshing_in_td.pdf (visited on 12/16/2022).
- [169] S. Friederich. “Entwicklung einer hochbrillanten Photoemissionsquelle für spinpolarisierte Strahlen”. Doctoral Dissertation. Mainz: Johannes Gutenberg-Universität Mainz, 2019.
- [170] “NOAA Magnetic Field Calculators”. 2022. URL: <https://www.ngdc.noaa.gov/geomag/calculators/magcalc.shtml> (visited on 12/16/2022).
- [171] G. Behrens et al. “Guidelines for the design of cryogenic systems”. In: *NRAO Electronic Division Internal Report* 306 (1997).
- [172] J. R. Howell et al. “Thermal radiation heat transfer”. Seventh edition. Boca Raton: CRC Press / Taylor & Francis Group, 2021. 1 p.
- [173] C. D. Hodgman. “Handbook of Chemistry and Physics”. Cleveland, Ohio: Chemical Rubber Publishing Co., 1948.
- [174] VACOM. “Outgassing Rates of Aluminum compared to Stainless Steel”. 2016. URL: <https://docslib.org/doc/9765937/outgassing-rates-of-aluminum-compared-to-stainless-steel> (visited on 12/16/2022).
- [175] G. Weston. “A paper in our education series: The theory and practice of vacuum science and technology in schools and colleges”. In: *Vacuum* 25.11 (1975), pp. 469–484. DOI: 10.1016/0042-207X(75)91653-X.
- [176] SAES Private Communication. St 707 Brochure. E-mail. 2022.
- [177] M. D. Sturge. “Optical Absorption of Gallium Arsenide between 0.6 and 2.75 eV”. In: *Physical Review* 127.3 (1962), pp. 768–773. DOI: 10.1103/PhysRev.127.768.
- [178] Y. Fritzsche. “Aufbau und Inbetriebnahme einer Quelle polarisierter Elektronen am supraleitenden Darmstädter Elektronenlinearbeschleuniger S-DALINAC”. Doctoral Dissertation. Darmstadt: Technische Universität Darmstadt, 2011.
- [179] Y. El-Hayek. “Aufbau eines Faraday-Cups”. Miniforschung (unpublished). TU Darmstadt, 2007.

-
-
- [180] B. Steiner. “Strahldynamik-Simulation einer polarisierten Quelle für den S-DALINAC (SPIN)”. Doctoral Dissertation. Darmstadt: Technische Universität Darmstadt, 2008.
- [181] A. N. Lab. “Elegant beam simulation software”. 2022. URL: <https://www.aps.anl.gov/Accelerator-Operations-Physics/Software#elegant> (visited on 05/30/2022).
- [182] V. L. T. Winter. “Strahldynamik-Simulationen für Photo-CATCH”. Bachelor Thesis (unpublished). Darmstadt: Technische Universität Darmstadt, 2021.
- [183] C. Day. Private Communication. E-mail. 2020.
- [184] T. Eggert, J. Enders, and Y. Fritzsche. “Cryogenic GaAs cathode development for improved lifetime”. In: *Proceedings of The 18th International Workshop on Polarized Sources, Targets, and Polarimetry — PoS(PSTP2019)*. Knoxville, Tennessee: Sissa Medialab, 2020, p. 041. DOI: 10.22323/1.379.0041.
- [185] T. Eggert et al. “First setup for cooled GaAs cathodes with increased charge lifetime”. In: *Proceedings of XVII International Workshop on Polarized Sources, Targets & Polarimetry — PoS(PSTP2017)*. Kaist, South Korea: Sissa Medialab, 2018, p. 017. DOI: 10.22323/1.324.0017.
- [186] T. Eggert et al. “Setup for Cooled GaAs Cathodes With Increased Charge Lifetime”. In: *Proceedings of the 9th Int. Particle Accelerator Conf. IPAC 2018*. Vancouver, BC, Canada, 2018, pp. 4542–4544. DOI: 10.18429/JACOW-IPAC2018-THPMK100.
- [187] S. Weih et al. “Development of a Cryogenic GaAs DC Photo-Gun for High-Current Applications”. In: *Proceedings of the 8th Int. Particle Accelerator Conf. IPAC2017 (2017)*, pp. 1391–1392. DOI: 10.18429/JACOW-IPAC2017-TUPAB032.

Curriculum Vitae

Tobias Eggert

teggert@ikp.tu-darmstadt.de

Academic Education

Doctorate (Physics) at Technische Universität Darmstadt *02/2017 - 12/2022*

- Dissertation Title : "Development of a Cryogenic DC Photoelectron Gun for GaAs Cathodes with Increased Charge Lifetime" under supervision of Prof. Dr. Joachim Enders
- Member and Student Representative of the Research Training Group 2128 Accelence
- Member of the Helmholtz Graduate School for Hadron and Ion Research (HGS-HIRE)
- Participation in the CERN Accelerator School 2017 (CAS)

Master of Science (Physics), Technical University of Darmstadt *10/2013 - 12/2016*

- Thesis: "Investigation of ionic liquids using triplet state solvation dynamics" under supervision of Prof. Dr. Thomas Walther

Bachelor of Science (Physics), Technical University of Darmstadt *04/2008 - 10/2013*

- Thesis: "Seed source for a picosecond fiber amplifier" under supervision of Prof. Dr. Thomas Walther

School Education

Abitur at Alfred-Delp-Schule in Dieburg

Graduation in 07/2007

List of Publications

2020

- T. Eggert, J. Enders, and Y. Fritzsche. “Cryogenic GaAs cathode development for improved lifetime”. In: *Proceedings of The 18th International Workshop on Polarized Sources, Targets, and Polarimetry — PoS(PSTP2019)*. Knoxville, Tennessee: Sissa Medialab, 2020, p. 041. DOI: 10.22323/1.379.0041

2018

- T. Eggert et al. “First setup for cooled GaAs cathodes with increased charge lifetime”. In: *Proceedings of XVII International Workshop on Polarized Sources, Targets & Polarimetry — PoS(PSTP2017)*. Kaist, South Korea: Sissa Medialab, 2018, p. 017. DOI: 10.22323/1.324.0017
- T. Eggert et al. “Setup for Cooled GaAs Cathodes With Increased Charge Lifetime”. In: *Proceedings of the 9th Int. Particle Accelerator Conf. IPAC 2018*. Vancouver, BC, Canada, 2018, pp. 4542–4544. DOI: 10.18429/JACOW-IPAC2018-THPMK100

2017

- S. Weih et al. “Development of a Cryogenic GaAs DC Photo-Gun for High-Current Applications”. In: *Proceedings of the 8th Int. Particle Accelerator Conf. IPAC2017 (2017)*, pp. 1391–1392. DOI: 10.18429/JACOW-IPAC2017-TUPAB032

Acknowledgements

This thesis would not have been possible without the help of many people. At this point I want to express my gratitude to all of them.

First, I want to thank my supervising professor Joachim Enders for making this thesis possible. He always had an open ear for me and contributed with helpful advices and inputs. In addition to my daily work he made it possible to visit multiple international conferences, allowing me to make new and exciting experiences as well as meeting new people. This way i could not only develop professionally but my social skills, too. I would also like to thank my co-supervisor Prof. Norbert Pietralla for his input and support throughout my thesis.

The persons I worked the most with, are my colleges from the working group, Yuliya, 2 · Max, Marius, Vincent and Neeraj. They supported me in the laboratory, with new ideas and inputs, when i got stuck in the designing process and created a fantastic working environment. Especially I want to thank Yuliya who helped me a lot with her years of experience even after she left the institute. Thanks also to the whole group for the good times, discussions and laughs we had aside from work. Another big thanks goes to Neeraj, who introduced me to the Photo-CATCH test stand and taught me the basics of vacuum and photo-cathode physics, when I first started my thesis coming from another field.

For their contribution to this work as Bachelor students i supervised, I want to thank Dominik and Victor.

Furthermore, I want to thank the whole staff of the IKP, the accelerator group, the electronics workshop and the mechanical workshop. Especially the latter, who always did their best to fulfill my requests as fast and accurate as possible, even when I had a lot of urgent requests.

The simulations with CST would not been possible without the help and advice from Wolfgang Müller located the TEMF institute in Darmstadt and Simon Friederich from the Johannes-Gutenberg University of Mainz. Your help is much appreciated.

I also want to thank the graduate schools HGS-HIRE and AccelencE for giving me the opportunity to visit workshops, conferences, international research facilities as well as social skill courses and to meet many new interesting people.

And last but not least i want to thank my family and friends who have been there for me in good and bad times. I am very grateful for their helpful advice and emotional support throughout the whole time. Special thanks to Caro, Uwe and Michaela for their great input on the written part of this work.

This project was funded through the DFG Research-Training Group 2128 Accelence and BMBF projects 05H15RDRB1 and 05H18RDRB1.